ALMA MATER STUDIORUM
UNIVERSITÀ DI BOLOGNA

DOTTORATO DI RICERCA IN

ONCOLOGIA, EMATOLOGIA E PATOLOGIA

Ciclo 38

Settore Concorsuale: 06/A2 - PATOLOGIA GENERALE E PATOLOGIA CLINICA

Settore Scientifico Disciplinare: MED/04 - PATOLOGIA GENERALE

SHIGA TOXINS AND HEMOLYTIC UREMIC SYNDROME: PATHOGENESIS, DIAGNOSIS, AND THERAPY

Presentata da: Luciano Consagra

Coordinatore Dottorato

Manuela Ferracin

Supervisore

Maurizio Brigotti

Co-supervisore

Giuseppina Di Stefano

Esame finale anno 2026

Index

Abstract

Hemolytic Uremic Syndrome (HUS) is a severe thrombotic microangiopathy characterized by non-immune hemolytic anemia, thrombocytopenia, and acute renal failure. The most common form is caused by infections with Shiga toxin-producing Escherichia coli (STEC), which release potent Shiga toxins (Stx). This research addresses three objectives: elucidating mechanisms by which Stx subtypes contribute to HUS pathogenesis, developing a diagnostic platform for Stx detection, and evaluating novel therapeutic strategies. Patients infected with STEC co-producing Stx1 and Stx2 exhibit milder clinical manifestations than those infected with Stx2-producing strains. To investigate this, human blood was exposed to toxins, and extracellular vesicles (EV) were isolated and characterized. Co-exposure to both toxins produced a less toxic EV population, showing reduced number, size, and toxic cargo compared to EV generated by Stx2 alone, which are most strongly associated with HUS. Prompt STEC diagnosis is crucial for preventing HUS. A gold plasmonic biosensor was developed, coupling surface-enhanced Raman spectroscopy (SERS) with principal component analysis (PCA) for rapid Stx detection. The system recognizes Stx1a, Stx2a, and Stx2a-cleaved, enabling real-time analysis. Currently, no specific HUS therapy exists. NAB815, a polymyxin B derivative, emerged as a promising candidate. Previous studies showed sub-bactericidal NAB815 doses reduce Stx2a-containing EV formation in human blood. In vivo evaluation using CD1 mice demonstrated effective protection against kidney damage when NAB815 was co-administered with either free Stx2a or blood-derived Stx2a-containing EV. Since antibiotics can trigger bacterial SOS response and increase Stx production, NAB815's safety was evaluated in both engineered and wildtype STEC strains. Results confirmed NAB815 as a safe strategy for HUS prevention and management. These findings provide new insights into HUS pathogenesis while offering innovative approaches for early diagnosis and targeted intervention in STEC infections.

Introduction

Hemolytic uremic syndrome: definition and classification

Overview of hemolytic uremic syndrome (HUS)

Hemolytic uremic syndrome, HUS, is a rare but severe life-threatening condition characterized by non-immune hemolytic anemia (hematocrit <30%), thrombocytopenia (platelet count <150,000 per mm^3), and acute kidney failure due to the formation of microthrombi in renal blood vessels [1]. HUS primarily affects the pediatric population, establishing itself as the leading cause of acute kidney failure in young children worldwide; however adult cases, particularly among the elderly, are well-documented [1-4].

HUS can be classified into two distinct forms based on the underlying pathogenesis, with typical HUS triggered by Shiga toxin-producing *Escherichia coli* (STEC), and atypical HUS, which stems from genetic or acquired dysregulation of the complement system [2, 5]. Unlike typical HUS, which is often associated with diarrheal illness, atypical HUS tends to be more chronic and relapsing, requiring long-term management. Other contributing factors, including drugs, infective agents, pregnancy, organ transplantation, and systemic diseases, can also give rise to HUS-like syndromes that do not fall strictly within the classifications of typical or atypical HUS [3]. Despite the different underlying causes, the clinical manifestation of HUS is often indistinguishable [2].

The condition was first described by Gasser and colleagues in 1955, laying the foundation for understanding this critical disease [6]. Since then, extensive research has led to improved diagnostic tools and therapeutic strategies.

Despite these advancements, the complexity of HUS continues to challenge medical professionals, as it remains a significant cause of morbidity and mortality worldwide, with outcomes varying considerably between typical and atypical forms. Early recognition and prompt medical intervention, including supportive care and targeted therapies, are necessary in improving patient outcomes, thus mitigating the risk of severe complications such as permanent kidney damage and neurological impairment.

Shiga toxin-producing *Escherichia coli* (STEC) and HUS

STEC-related HUS

Typical HUS, also known as STEC-related HUS, is the most common form of HUS, primarily affecting children. It accounts for approximately 90% to 95% of all HUS cases, making it the dominant clinical subtype [5]. While various microbial pathogens can trigger the condition, STEC remains the predominant cause worldwide [2, 5]. Typical HUS may arise sporadically, in localized clusters, or as large-scale foodborne outbreaks, as evidenced by several notable international incidents in recent years [2, 3].

The term typical HUS reflects its well-distinct association with STEC infections and a predictable clinical course. This classification emerged as the first recognized form of the disease and remains the most extensively documented variant in pediatric medicine [1-3]. The significance of STEC as the unambiguous aetiologic agent of HUS was confirmed by Karmali and colleagues [7], shortly after the correlation of *E. coli* O157:H7 with several cases of bloody diarrhea in the United States in 1982, by the isolation of different STEC serotypes, including O157:H7, from stool samples of children affected by HUS [8]. These serotypes produce potent exotoxins able to damage and intoxicate Vero cells (renal fibroblast-like cells from African green monkey), leading to cellular injury and death [7]. These toxins, collectively referred to as Shiga toxins (Stx), are variably neutralized by antiserum against the Shiga toxin produced by *Shigella dysenteriae* serotype [9]. Alternative terms for these toxins include Verotoxins, Verocytotoxins, and Shiga-like toxins, reflecting their mechanism of action and historical discovery [3, 10].

Among the different STEC serogroups, the production of Stx plays a critical role in disease severity. There are two main types of Stx: Shiga toxin 1 (Stx1) and Shiga toxin 2 (Stx2), which result in a different clinical outcome [9, 10]. The pathogenic mechanisms and implications of Stx will be explored in detail in the dedicated chapter.

Typical HUS pathogenesis

Typical HUS is characterized by thrombotic microvascular lesions which primarily affect renal glomeruli, the intestinal tract, and cerebral tissues [2, 9, 10]. Endothelial injury within microvasculature constitutes the fundamental pathogenic mechanism in HUS development, with susceptible cells expressing globotriaosylceramide (Gb3Cer) receptors that bind Stx [9, 10].

Following exposure to STEC mainly via contaminated water or food sources, an asymptomatic period of approximately 72 hours precedes clinical manifestation [9, 10]. The initial presentation comprises non-hemorrhagic diarrhea accompanied by abdominal pain. These gastrointestinal symptoms result from specific bacterial adherence mechanisms rather than direct Stx effects.

STEC establish attachment to intestinal epithelium through a specialized Type III secretion apparatus, which facilitates translocation of bacterial effector molecules into epithelial cells [11]. This intimate interaction generates characteristic attaching and effacing lesions, characterized by microvilli destruction and formation of actin-derived pedestals at bacterial attachment sites [11]. The resultant architectural disruption compromises the normal absorptive function of the intestinal epithelium, thereby inducing watery diarrhea [10-12]. In many cases, within one to two days, the clinical picture progresses to bloody diarrhea, which is the most common prodromal symptom in patients who will develop HUS [9-11, 13]. Unlike the early nonspecific symptoms, bloody diarrhea is directly related to the toxic effects of Stx [9]. Stx produced by bacteria crosses the large bowel epithelium and enters the underlying *lamina propria*, even though human enterocytes lack specific receptors for the toxin [14]. After penetrating the intestinal *lamina propria*, Stx gain access to the circulatory system where they specifically target endothelial cells expressing Gb3Cer receptors [9]. This molecular interaction precipitates endothelial injury, resulting in the histological features of hemorrhagic colitis: edematous changes affecting mucosal and submucosal layers, localized hemorrhagic lesions, tissue necrosis, and microvascular thrombotic lesions [15, 16].

After approximately 5-7 days from the initial presentation of hemorrhagic diarrhea, a subset of patients (approximately 15%) progress to HUS, representing a critical transition from a local gastrointestinal pathology to a potentially fatal multi-organ disorder [9, 10]. HUS develops when blood Stx target endothelial cells in the kidneys and brain, resulting in endothelial damage and dysfunction that leads to thrombotic microangiopathic lesions in the affected organs [9, 10].

Comprehensive microscopic examination of human tissues in HUS-affected patients has been performed. The distinctive renal pathology explains the first component of the pathological triad defining HUS; i.e. acute morphological alterations predominantly within renal glomeruli [2]. These pathological features include modifications in capillary wall dimensions, separation of endothelial cellular elements from their underlying basement membranes, and accumulation of fibrinous material with platelet aggregates resulting in

congested glomerular structures [2, 15, 17]. Renal failure is directly associated with microthrombotic formations that impair microcirculatory perfusion through luminal constriction or complete occlusion [9, 15].

In affected individuals, thrombocytes exhibit activation patterns with substantial incorporation into microthrombotic complexes and subsequent sequestration within compromised organs, and/or clearance via the reticulo-endothelial system [12, 18]. This high platelet consumption underlies the marked thrombocytopenia observed clinically, representing the second element of the established triad [12, 18].

The pathological triad is completed by the development of hemolytic anemia, characterized by erythrocyte fragmentation producing distinctive morphological patterns [2]. These damaged erythrocytes undergo elimination through reticuloendothelial clearance mechanisms [12, 18]. The erythrocyte structural disruption occurs through mechanical forces, as these cellular elements pass through partially obstructed glomerular microvascular channels [9, 12, 18].

Consistent with the established significance of Stx in HUS pathogenesis, numerous scientific investigations have been conducted to elucidate the pathophysiological mechanisms of the syndrome, based on specific toxic effects observed in susceptible organs and cellular populations.

STEC serotypes and mode of transmission

E. coli are Gram-negative bacteria that typically inhabit the gastrointestinal tract of mammals and birds as part of the normal microbiota. However, specific strains have acquired virulence factors that enable them to cause disease in both humans and animals [19]. Based on their virulence factors, these strains are classified into distinct pathogroups [19]. In addition to pathogroup classification, *E. coli* strains are further differentiated by serotyping, which is based on variations in the O antigen, part of the lipopolysaccharide (LPS) on the bacterial outer membrane, in the H antigen, which corresponds to the flagellar protein, and in the K antigen which is related to the capsular polysaccharide antigen [19]. This serological classification aids in identifying and distinguishing strains with epidemiological and clinical relevance. The enterohemorrhagic *E. coli* (EHEC) strains are particularly significant, as they can cause severe conditions including hemorrhagic diarrhea and HUS. Many EHEC strains are classified within the STEC group due to their ability to produce potent cytotoxins that inhibit protein synthesis in eukaryotic cells [20]. Among the numerous STEC serogroups, a

few have been identified as the most clinically significant due to their high virulence and strong association with outbreaks. The global distribution of the most prevalent STEC serogroups, as well as serogroups most frequently associated with HUS, is summarized in Table 1 [10].

Location and Year	Most Common STEC Serogroups		Age Distribution		STEC Serogroups in HUS	
	Serogroup	Distribution	Age	Distribution	Serogroup	Distribution
		percent		*percent or incidence/total population*		*percent*
Europe†						
2021	O157	15.2	—	—	O26	34.0
	O26	14.8	—	—	O157	19.6
	Not reported	44.1	—	—	O80	11.0
	Nontypable	25.9	—	—	O145	7.6
	—	—	—	—	Not reported	27.8
2020	—	—	0–4 yr	27.8	—	—
	—	—	5–14 yr	12.8	—	—
	—	—	15–24 yr	8.9	—	—
	—	—	25–44 yr	14.1	—	—
	—	—	45–64 yr	15.4	—	—
	—	—	≥65 yr	21.2	—	—
United States‡§						
2016–2020	O157	15.8	0–4 yr	18.7/100,000	O157	83.9
	O26	7.9	5–9 yr	5.4/100,000	O111	5.7
	O103	7.9	10–19 yr	5.7/100,000	O145	3.8
	O111	5.1	20–64 yr	3.8/100,000	O26	2.8
	Other	12.9	≥65 yr	4.8/100,000	Undetermined	2.4
	Culture-independent diagnostic test	44.1	—	—	Other	1.4
	Non-O157, not serogrouped	6.3	—	—	—	—
Argentina¶						
2018–2019	O157	31.0	Mean, 36.1±30.1 mo		—	—
	O145	20.7	Median, 24.0 mo (IQR, 15–47)		—	—
	O26	13.8	—	—	—	—
	O121	3.4	—	—	—	—
	Other	17.3	—	—	—	—
	Nontypable	13.8	—	—	—	—
2005–2016‖	—	—	—	—	O157	73.6
	—	—	—	—	O145	16.8
	—	—	—	—	O121	5.4
	—	—	—	—	O26	0.7
	—	—	—	—	O103	0.7

Table 1

Distribution of the most common STEC serogroups, age distribution of cases, and STEC serogroups associated with HUS in Europe, the United States, and Argentina. Data are derived from national and regional surveillance systems. Percentages represent the proportion of reported STEC infections or HUS cases attributed to each serogroup, unless otherwise indicated. Age-specific data are shown as percentages or incidence per 100,000 population. Modified from [10].

Although STEC vary in prevalence across different regions, they share similar pathogenic mechanisms through the production of Stx [10]. Based on their virulence and potential for causing serious health complications, STEC are classified into low-risk and high-risk strains [3]. Low-risk STEC strains produce Stx1 but not Stx2 and are typically associated with milder illnesses, such as non-bloody diarrhea, and less frequent complications [21-25]. They rarely lead to HUS, except in immunocompromised adults [21, 26]. Given their propensity to precipitate HUS, the subset of STEC that produces Stx2 are referred to as high-risk strains [3].

Consistent with global surveillance data (Table 1), the O157 serogroup is the most recognized and globally prevalent high-risk STEC, responsible for the majority of severe infections and outbreaks [13, 27, 28]. It remains the dominant serotype detected in fecal samples from symptomatic individuals worldwide, accounting for 84% of documented HUS cases in the United States [10]. Due to its clinical relevance, the term *E. coli* O157 refers to any STEC possessing the antigen of this serogroup, while STEC with O antigens different from O157 are classified as non-O157 STEC. Although the O157 serogroup comprises multiple serotypes defined by their H antigens, O157:H7 remains the predominant and most virulent serotype associated with human disease [27, 28]. A notable phenotypic characteristic of *E. coli* O157:H7 is its inability to ferment sorbitol, which enables its differentiation on sorbitol–MacConkey agar, where it typically forms colorless colonies after 16 to 24 hours of incubation [29]. Beyond O157, many non-O157 STEC serogroups have been implicated in human infections. Other high-risk non-O157 serogroups, such as O26, O104, O111, and O145, have also been responsible for outbreaks [2, 3].

The incidence of STEC infections peaks during the summer and early fall, a period when transmission is more frequent and can occur with a very low infectious dose [3, 30]. STEC strains are zoonotic pathogens predominantly colonizing the gastrointestinal tract of ruminants, with cattle recognized as the principal reservoir [8]. Additionally, STEC were also isolated in many other animal species, including sheep, goat, buffalo, and deer [31]. Cattle are asymptomatic carriers of STEC due to the limited expression and distinct localization of Stx receptors [32]. After internalization into bovine epithelial cells, the toxin is trafficked to lysosomes rather than the endoplasmic reticulum, leading to its degradation and preventing cytotoxic effects [33]. As a result, cattle can harbor and shed STEC in their feces without exhibiting clinical symptoms. Infections primarily arise through foodborne transmission, waterborne transmission, zoonotic exposure, and human-to-human spread [3]. Among these, foodborne outbreaks represent the most prevalent route of infection, often

leading to large-scale public health concerns [19, 34]. Contamination can occur when individuals consume undercooked or raw meat, particularly ground beef [31]. Improper meat handling and insufficient cooking facilitate bacterial transmission. Additionally, unpasteurized dairy products pose a significant risk, as raw milk and its unpasteurized derivatives can become contaminated through exposure to fecal matter from infected animals [35]. Consumption of raw vegetables is another important source of STEC, especially when fruits and vegetables are irrigated with contaminated water or cross-contaminated during food processing [36, 37]. Waterborne transmission further contributes to infection risk, with drinking or recreational water serving as a medium for bacterial spread [38, 39]. Zoonotic transmission plays a crucial role in STEC dissemination. Direct contact with livestock in farm environments, or animal exhibits, such as petting zoos and slaughterhouses, significantly increases the risk of infection, particularly in children [32, 40, 41]. Wildlife and other farm animals can also function as secondary reservoirs, further facilitating environmental contamination and increasing the likelihood of human exposure [31]. In addition to foodborne and zoonotic transmission, STEC can spread directly between individuals, primarily via the fecal-oral route. This mode of transmission is particularly concerning in environments where hygiene practices are inadequate, such as households, daycare centers, and healthcare facilities [39, 42, 43]. Young children, who may not practice adequate hand hygiene, are at heightened risk of unknowingly transmitting the bacteria to others [44].

Major outbreaks and the global burden of STEC infections

Several significant STEC outbreaks have occurred throughout history, highlighting the impact of these microorganisms on public health. In 1982, one of the earliest and most pivotal *E. coli* O157:H7 outbreaks was traced to undercooked hamburgers served at a fast-food restaurant chain in the United States, resulting in 47 confirmed cases of hemorrhagic colitis [8]. Although no cases of HUS were reported, the incident marked the first identification of *E. coli* O157:H7 as a human pathogen and established its role as a significant foodborne agent of severe gastrointestinal illnesses [8]. In 1996, Japan reported 9,451 cases of *E. coli* O157:H7, including the large Sakai City outbreak linked to contaminated raw bean sprouts served in school lunches, which resulted in 12 deaths [45]. Between May and July 2011, Europe faced one of its most severe STEC outbreaks, primarily affecting adults in

Germany. The incident was caused by an atypical strain, *E. coli* O104:H4, and was related to contaminated fenugreek sprout consumption [46]. The outbreak resulted in 3,816 infections, with 845 (22%) progressing to HUS [47, 48]. Fifty-four patients died, and nearly half of those with HUS experienced neurological complications and required dialysis [9, 47]. Strikingly, 88% of cases occurred in adults, with a median age of 42 years, and 68% were female; an atypical epidemiological pattern for HUS, which is usually more common in young children [48]. Genomic analysis revealed that this strain had acquired the *stx2*-encoding prophage via horizontal gene transfer, transforming a previously enteroaggregative strain into a highly virulent STEC variant [47, 49]. This event highlighted two critical insights: the remarkable genetic adaptability of *E. coli* and the central pathogenic role of Stx in severe human disease [9]. This crisis demonstrated the high virulence of non-O157 STEC strains and emphasized the necessity for robust surveillance systems.

It has been estimated that STEC infections cause approximately 2.8 million cases of acute illness annually [27]. In addition, about 3,890 cases of HUS and 230 deaths occur worldwide each year due to STEC infections [27]. Latin America carries a comparatively high burden of STEC infections, with Argentina, Uruguay, and Chile identified as key endemic zones [50]. In Argentina, reported rates of HUS in children under five have reached 12.2 per 100,000, representing one of the highest documented national incidences worldwide [51].

Atypical HUS and complement dysregulation

Atypical hemolytic uremic syndrome (aHUS) is a rare, progressive, and potentially fatal thrombotic microangiopathy driven by uncontrolled activation of the complement system [2, 52]. In contrast to typical HUS, which is caused by STEC infections, aHUS results from dysregulation of the alternative complement pathway, causing persistent complement deposition on endothelial cells, resulting in hemolytic anemia, thrombocytopenia, and acute kidney injury [2]. The defective regulation of the complement system in aHUS is often attributable to mutations in genes encoding key complement regulatory proteins or complement factors, including complement factor H (CFH), complement factor I (CFI), membrane cofactor (MCP/CD46), complement component C3, and complement factor B (CFB) [52-54]. These mutations typically result in loss of function of inhibitory regulators (such as CFH, CFI, MCP/CD46) or gain of function in activators (C3, CFB), shifting the

balance toward pathological complement amplification on host tissues [2, 54]. In some cases, autoantibodies against CFH contribute to disease pathogenesis [2, 52]. Due to the lack of protective mechanisms that normally prevent complement activation on host cells, complement deposition on self-cells, followed by cascade activation, leads to the assembly of the membrane attack complex (MAC or C5b-9) that, by inserting into endothelial membranes, causes direct cell damage [2, 54]. Endothelial injury initiates a cascade of pro-thrombotic events, fostering platelet activation, adhesion, and aggregation. This pathological response promotes the development of microvascular thrombi, which in turn leads to platelet consumption, manifesting clinically as thrombocytopenia [2]. As red blood cells pass through these narrowed, thrombus-laden vessels, they are mechanically fragmented, resulting in the onset of microangiopathic hemolytic anemia. The kidneys are especially susceptible to this process due to their extensive microvascular network and high perfusion rate [52]. Thrombotic obstruction within glomerular capillaries and arterioles impair filtration and causes acute kidney failure, which may advance to end-stage renal disease without timely intervention [52]. While genetic or autoimmune dysregulation of the complement system underlies the pathogenesis of aHUS, environmental and physiological stressors such as infections, pregnancy, specific medications, or organ transplantation can trigger disease onset in genetically predisposed individuals [55]. The cornerstone of aHUS treatment is the inhibition of the complement system, aimed at interrupting the cascade of endothelial injury and thrombotic microangiopathy. In particular, eculizumab, a humanized monoclonal antibody that targets complement component C5, preventing its cleavage into C5a and C5b, and thereby blocking formation of the MAC [2], is indicated for the treatment of aHUS. Eculizumab administration has been shown to prevent hematological relapses and renal failure, to enhance kidney function in affected patients, and to reduce the risk of aHUS recurrence after transplantation [2]. This therapy has significantly improved patient outcomes by decreasing the need for dialysis, preventing progression to end-stage renal disease, and lowering mortality rates. Immunosuppressive therapy is used in aHUS patients whose disease is driven by the production of autoantibodies, particularly those targeting complement regulatory proteins such as CFH. Prior to the introduction of targeted complement inhibitors, the clinical management of patients with aHUS primarily relied on supportive care measures, including plasma exchange and the management of fluids and electrolytes [2].

Shiga toxins: from classification and structure to cellular mediated toxicity

The Shiga toxin family and its genetic diversity

The discovery and characterization of Stx spans more than a century of microbiological research, beginning in the late 19th century when Kiyoshi Shiga and colleagues first identified *S. dysenteriae* and its associated toxin, now known as Shiga toxin [56]. Nearly 80 years later, a toxin almost identical to Shiga toxin was discovered in certain *E. coli* isolates [57]. The only difference was a single amino acid substitution in the A subunit: Thr at position 45 in Shiga toxin was replaced by Ser, therefore indicating their shared evolutionary origin [58]. To establish taxonomic clarity, the toxin produced by *S. dysenteriae* retained its original designation, while that found in *E. coli* strains was designated as Shiga toxin 1 (Stx1). Subsequent studies identified other *E. coli* isolates that produced an immunologically distinct, yet functionally similar toxin, termed Shiga toxin 2 (Stx2) [59]. Although Stx2 shares the same cytotoxic mechanism as Stx1, it exhibits markedly different antigenic properties, with only approximately 50-60% amino acid sequence identity [60]. Together, these potent cytotoxins constitute the defining virulence determinant of STEC, enabling progression from localized enteric infection to potentially fatal systemic complications. Moreover, STEC strains can express either a single Stx subtype or a combination of multiple subtypes, which can influence their virulence and disease severity [21]. Indeed, despite belonging to a unified toxin family, Stx1 and Stx2 display remarkable genetic heterogeneity, with each type encompassing multiple subtypes that significantly influence pathogenicity, tissue tropism, and clinical outcomes in infected individuals [59, 61]. The prototype *E. coli* Stx from each main group, now designated Stx1a and Stx2a to distinguish them from other toxin subtypes, remains the most commonly identified toxins associated with human disease [61]. However, numerous subtypes exist within each toxin group, as detailed in classification systems [61].

In addition to the prototype Stx1a, the Stx1 group includes subtypes Stx1c and Stx1d, which differ immunologically from Stx1a [59]. Stx1c, found primarily in sheep STEC isolates, shares 97% amino acid identity with Stx1a and is mainly detected in animal and environmental reservoirs, typically causing diarrhea [62]. The most divergent Stx1d, with 94% identity to Stx1a, has unique antigenic properties that complicate detection [63]. It is predominantly isolated in bovine and environmental samples and is rarely isolated from

humans [59]. Overall, the Stx1 subfamily is highly conserved, leading to milder clinical outcomes compared to Stx2 subtypes [59].

In contrast, the Stx2 group displays considerably greater genetic diversity with subtypes Stx2a through Stx2i, exhibiting less than 60% sequence homology compared with the toxin from *S. dysenteriae* [64]. Among these, Stx2a, Stx2c, and Stx2d are significantly associated with elevated risks of developing HUS [59, 64]. Stx2c, the first identified subtype beside Stx2a, is characterized by reduced toxicity on both Vero cells and animal models, and reacts differently to some monoclonal antibodies compared to Stx2a [59]. Stx2d, also known as activatable Stx2d, is a subtype of the Stx2 family that stands out due to its unique ability to increase its cytotoxic activity when exposed to elastase, an enzyme found in intestinal mucus [65]. Although Stx2c and Stx2d share identical B subunits and differ only by two amino acids in the A_2 fragment, Stx2d is significantly more toxic, exhibits greater *in vivo* potency, and is more strongly associated with the development of HUS [59, 66, 67]. Additionally, Stx2e, Stx2f, and Stx2g are predominantly associated with animal-specific STEC strains and are rarely implicated in human disease [59]. Among these, Stx2e is associated with a fatal disease in swine known as edema disease, which causes neurological disorders and is frequently deadly [68]. Overall, the Stx2 family is complex, with variants that differ in cytotoxicity, host specificity, and disease outcomes, making it critical for understanding the pathogenic potential of STEC strains and their associated diseases [64].

The genetic variability among Stx manifests in critical functional differences, including receptor binding affinity, cellular trafficking efficiency, and susceptibility to neutralization [59, 64].

Notably, the genes responsible for producing Stx1 and Stx2, known as *stx1* and *stx2*, are carried by temperate bacteriophages that integrate into the bacterial chromosome [69]. Every STEC strain contains at least one temperate lambdoid prophage that carries the genes for Stx. These phages remain dormant for most of their life cycle, existing as prophages inserted at specific chromosomal sites, enabling horizontal gene transfer across bacterial populations and facilitating the emergence of novel strains through phage-mediated recombination events [69, 70]. Recent whole-genome sequencing approaches have further revealed complex mosaicism within prophage elements carrying *stx* genes, suggesting ongoing evolutionary dynamics that contribute to the pathogenic diversity of STEC strains and their variable clinical manifestations across different geographic regions [70, 71]. Both genetic mobility and variation make STEC infections unpredictable and complicate efforts to control

their spread, highlighting the importance of surveillance and research activity to mitigate their impact on public health.

Prophages can be induced to enter the lytic cycle either spontaneously or in response to environmental stresses such as chemical or physical agents [70, 72]. Activation of the bacterial SOS response by DNA-damaging compounds triggers prophage induction, leading to the self-cleavage of the CI repressor and subsequent excision and replication of the phage genome [70, 72]. During this process, early phage genes are expressed, followed by co-transcription of the *stx* genes with the phage late genes, which increases Stx production [69, 72]. The assembly of new phage particles within the host cytoplasm culminates in cell lysis, releasing both phages and toxins into the environment [69, 72]. While Stx2 synthesis is primarily dependent on phage induction, Stx1 is also influenced by iron levels through an internal promoter (p*stx1*) and a ferric uptake regulator (Fur) binding site, leading to increased expression under low-iron conditions [73].

The regulation of *stx* genes has important therapeutic consequences: the use of various classes of antibiotics is not recommended, as they can trigger the SOS response, leading to prophage activation and Stx production, which may worsen symptoms in STEC-infected patients [10, 72, 74, 75].

Molecular structure of Shiga toxins

Despite sequence variations between Shiga toxin from *S. dysenteriae*, Stx1 and Stx2, Stx share a consistent structural framework. They are specifically ribosome-inactivating proteins (RIPs), potent exotoxins produced by phylogenetically distinct organisms, such as plants, bacteria, and fungi [9, 76]. Among the three different structural groups, Stx belong to the class 2 RIPs, since they are composed of two different subunits and present the typical AB5 structure [9, 76]. Thus, the holotoxin consists of a pentameric B chain complex responsible for cell receptor binding that is non-covalently bound to a catalytic A chain [9, 76]. This structural organization enables receptor binding, internalization, and protein synthesis inhibition in target cells. The three-dimensional organization of the representative Stx1, including the pentameric B subunit and the A domains, is illustrated in the ribbon diagram (Figure 1).

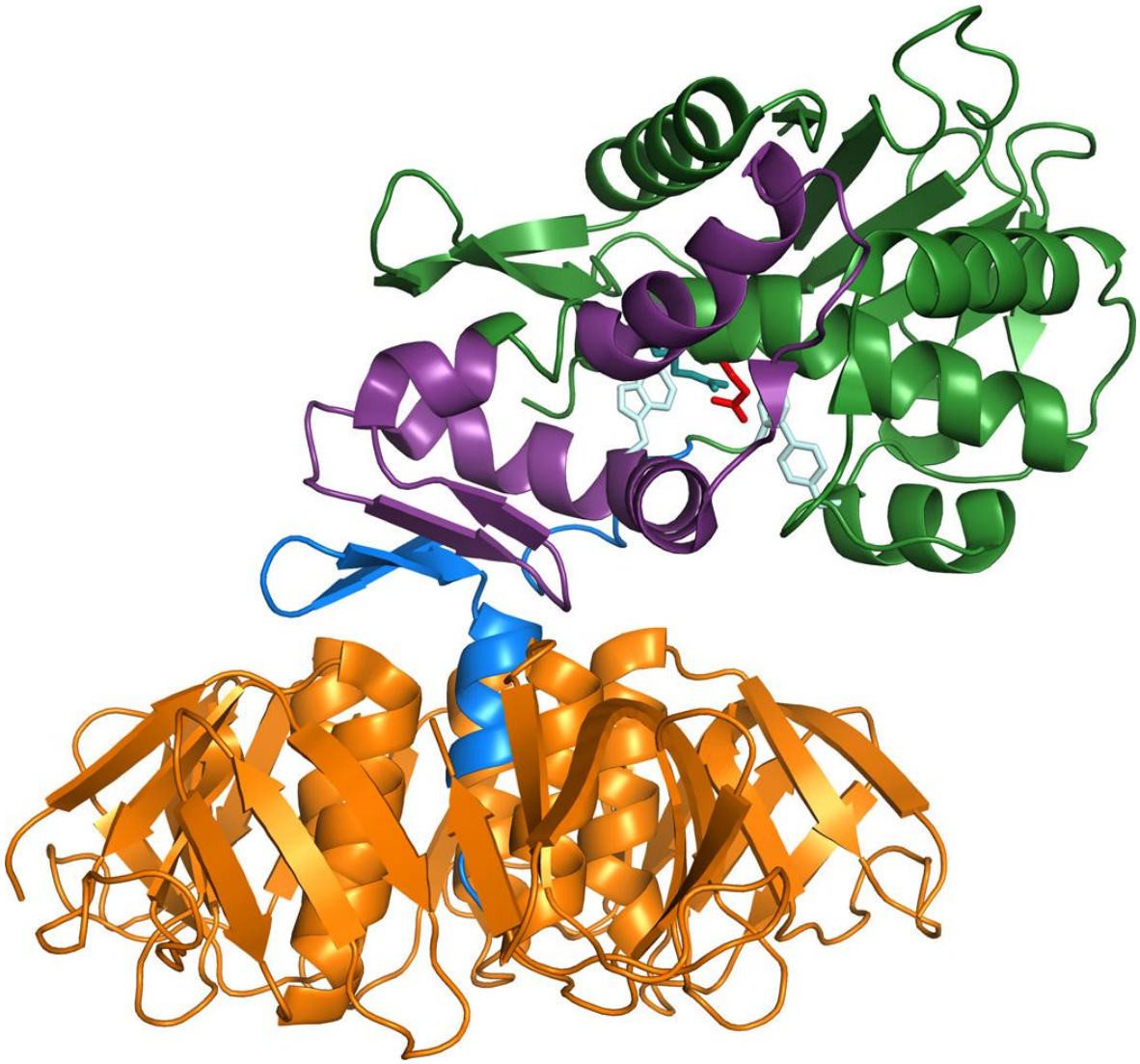

Figure 1.

Ribbon diagram of Stx1. The pentameric B subunit is shown in orange, while the A2 chain is depicted in blue. Most of the A1 domain is colored green, except for the ribosome-interacting region, highlighted in purple. The catalytic residue Glu167 is shown in red, and other active-site side chains are in light blue. Picture from [59].

The B subunit of both Stx1a and *S. dysenteriae* Shiga toxin is composed of five identical monomers, each of 69 amino acids (~7.7 kDa), assembled non-covalently into a pentameric ring. In contrast, Stx2's B pentamer comprises five monomers of 71 amino acids each, arranged similarly into a pentameric ring [59]. Each monomer relies in two three-stranded antiparallel β-sheet, constituting a six-stranded β-sheet which is further stabilized by hydrogen bonds [77]. These interactions create a pocket with up to three receptor binding sites: site 1 (involving Asp16, Asn32, and Arg33) exhibits the highest affinity (Kd = 10^{-9} M); site 2 (involving Thr54, Val55, and Gly63) shows intermediate affinity; while site 3

(involving Trp29, Asn30, and Trp33) displays the lowest affinity but contributes significantly to membrane insertion [77-79]. Moreover, an α-helix from each monomer points inward, forming an ~11 Å central pore [77, 78]. The A chains belonging to both mature Stx1a and Shiga toxin from *S. dysenteriae* contain 293 amino acids, while the Stx2a A chain is four residues longer at the C terminus [59]. The A subunit of both Stx1a and Stx2a is initially synthesized as a single polypeptide of ~32 kDa and exerts its enzymatic activity via a crucial glutamic acid residue at position 167 [59]. A disulfide bond stabilizes the A subunit conformation and is essential for its proper function, occurring between Cys242 and Cys261 in Stx1a and between Cys241 and Cys260 in Stx2a [59, 77].

Furthermore, the A subunit of Stx contains a highly conserved arginine-rich sequence (Arg248-Arg251 in Stx1) recognized by furin protease [80, 81]. Cleavage at this site produces the cleaved form of the toxins (Stx-cl), constituted by the A1 fragment (~27 kDa) and the A2 peptide (~5 kDa), which remain linked by a disulfide bond [59, 77]. The A1 domain of Stx contains the catalytic site with N-glycosidase activity, removing a conserved adenine from 28S rRNA in the 60S ribosomal subunit, thereby preventing ribosomal interaction with elongation factors, blocking protein synthesis, and inducing apoptosis [59, 77]. All Stx share a similar enzymatic mechanism, but the A1 fragment of Stx2 interacts with mammalian ribosomes more rapidly and with greater affinity compared to that of Stx1 [82]. The A1 fragment of Stx contains the key residues Arg170, Tyr77 and 114, and Glu167 which coordinate the binding to the adenine target [77]. The A2 fragment serves a structural role, anchoring the A1-containing catalytic site with B subunit [77]. In Stx1a, residues 279-287 form an extended α-helix that lies antiparallel to the five α-helices of the B subunits and penetrates 11 Å into the B pentamer's 20 Å-deep central pore [77]. Finally, in Stx2a, the C-terminal region of the A2 fragment also extends toward the central pore of the B pentamer [83].

Shiga toxin-mediated cellular toxicity

Glycosphingolipid receptors as targets of Shiga toxins

Stx initiate their cytotoxic activity by specifically interacting with glycosphingolipid receptors present on the surface of host cells. This initial interaction is mediated by the mature B subunit pentamer of the toxin, which recognizes and binds to a distinct carbohydrate motif (Galα1-4Galβ1-4Glc) found within Gb3Cer, the primary human receptor

for Stx [77, 84, 85]. Gb3Cer, also known as CD77, consists of a ceramide backbone, made of sphingosine and a fatty acid linked by an amide bond, coupled with the oligosaccharide head group [77, 86, 87]. Variations in the length, saturation, and hydroxylation of the fatty acid chain result in multiple isoforms, influencing the toxin's binding affinity and specificity [85]. Although Gb3Cer is the principal human receptor, Stx2e displays preferential binding to globotetraosylceramide (Gb4Cer), a structurally related glycosphingolipid also embedded in the outer leaflet of the cell membrane [77]. Figure 2 provides the molecular structures of Gb3Cer and Gb4Cer, respectively.

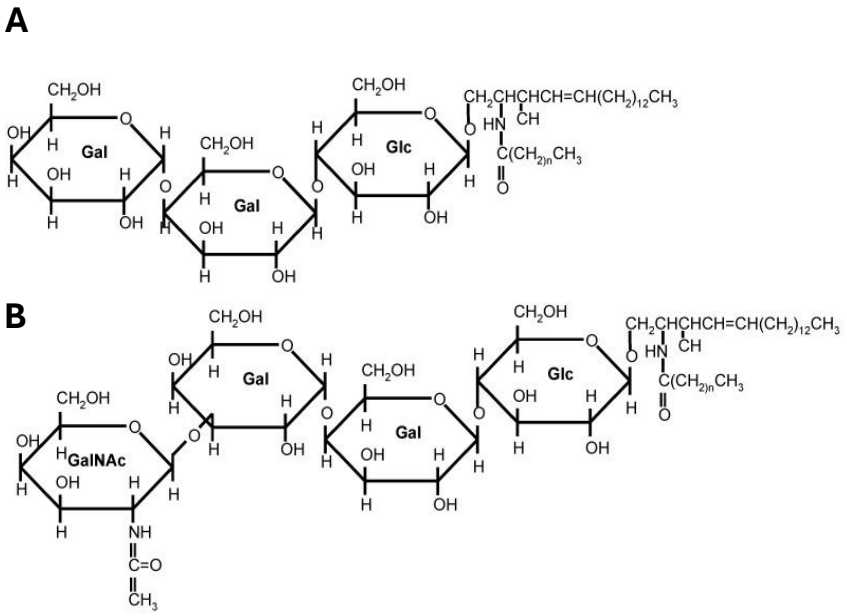

Figure 2.

Molecular structure of globotriaosylceramide (Gb3Cer) (**A**) and globotetraosylceramide (Gb4Cer) (**B**). Modified from [77].

Gb3Cer is found on the membranes of various mammalian tissue cells, with its expression and distribution differing between species [85]. This variability requires caution when applying findings from animal models to humans. In the human kidney, Gb3Cer is found in several cell types including glomerular endothelial cells, podocytes, mesangial cells, and tubular epithelial cells [77, 85]. Conversely, in mice, its expression is mainly limited to the proximal tubular epithelium [85]. Despite differences in renal Gb3Cer distribution between humans and mice, mice remain suitable models for studying STEC- or Stx-induced kidney lesions similar to those observed in human HUS patients [85]. Regarding the peripheral nervous system, Gb3Cer is present in both neurons of the dorsal root ganglia

and endothelial cells in humans and rabbits [85]. In contrast, in mice and rats, the receptor is detected only in neurons, with endothelial cells lacking Gb3Cer expression [85]. The human intestinal tract shows variable Gb3Cer expression, with highest levels in Paneth cells [88]. Thus, the distribution of these receptors in human tissues determines Stx tropism, explaining the pathophysiology of Stx-mediated diseases and why the kidney is a primary target in HUS. Gb3Cer is also expressed by several circulating blood cell components, including platelets, monocytes, and erythrocytes, but not by neutrophils [89-92].

Gb3Cer has roles extending well beyond its function as a receptor for Stx. The Stx principal receptor is physiologically localized within lipid rafts, specialized microdomains of the plasma membrane which facilitate signal transduction and membrane organization [84]. In neural development, Gb3Cer influences the balance of glycosphingolipid composition, regulating the transition necessary for neural differentiation through pathways involving key epigenetic factors [85]. Within the immune system, Gb3Cer is expressed on specific B cell subsets and may participate in modulating receptor signaling and apoptotic pathways, although its exact contribution to these processes remains incompletely understood [85]. Gb3Cer also supports antiviral defenses by facilitating type I interferon receptor signaling, highlighting its role in immune response regulation [93]. Furthermore, Gb3Cer is present in professional antigen-presenting cells, where it could influence major histocompatibility complex class II function, though *in vivo* relevance is still unclear [94]. Importantly, Gb3Cer contributes to membrane stability in kidney proximal tubule cells, playing a critical role in protein reabsorption and renal function [95]. Beyond its physiological role, it has been demonstrated that the deletion in mice of the gene encoding Gb3Cer synthase, the enzyme responsible for producing Gb3Cer from lactosylceramide, provides key insights into the role of Gb3Cer as the major receptor for Stx [96]. In these genetically modified mice, the absence of Gb3Cer resulted in complete resistance to Stx, demonstrating that Gb3Cer is essential for toxin binding and subsequent toxicity [96, 97].

However, the cytotoxic potency of Stx is not solely determined by their binding interactions with Gb3Cer receptors. Although Stx1 demonstrates a higher binding affinity to Gb3Cer compared to Stx2, experimental evidence consistently shows that Stx2 exhibits significantly greater *in vivo* toxicity [98, 99]. Research in animal models revealed that the LD_{50} value of Stx2 is 400-fold lower than that of Stx1 in mice, indicating higher potency [99]. In baboon studies, four sequential doses of Stx2 (25 ng/kg) induced HUS, whereas equivalent doses of Stx1 produced no pathological effects [100]. This differential toxicity is further supported by epidemiological data showing that most HUS fatalities are associated

with infections caused by Stx2-producing *E. coli* strains [21, 23, 24]. Although young children display a higher incidence of HUS, studies indicate that basal renal Gb3Cer expression does not decrease with age, suggesting that factors other than Gb3Cer abundance contribute to pediatric susceptibility [101].

These findings collectively indicate that while Gb3Cer receptor plays a key role in Stx-induced effects, other more complex mechanisms that determine the overall toxicity of these bacterial toxins are involved. The effectiveness of cellular intoxication involves a sophisticated multi-step process, including cell surface entry, strategic intracellular navigation through the Golgi network and endoplasmic reticulum, cleavage of the A chain, and precise cytosolic release of the A1 fragment by reduction of the connecting disulfide bond. These intricate transport mechanisms significantly influence the toxin's destructive potential, demonstrating that cytotoxicity is not solely determined by receptor interaction or strain variability, but also by the remarkable ability of the toxin to successfully navigate and compromise cellular structures. Finally, it is important to note that in the blood of HUS patients have been found two Stx2 forms, native and cleaved (with A1 and A2 fragment linked by a disulfide bridge). Although both native Stx2 and its cleaved form (Stx2-cl) exert comparable toxic effects on sensitive cells via Gb3Cer, they differ in their binding properties to circulating cells, serum components, and complement factors, thereby contributing in distinct ways to the pathogenesis of HUS [102].

From receptor-mediated uptake to ribotoxic effects of Shiga toxins

Upon binding Gb3Cer on the plasma membrane, Stx undergo internalization mainly via clathrin-dependent endocytosis, although clathrin-independent pathways have also been described [12, 59, 103, 104]. This receptor-mediated uptake is critical, as the holotoxin exhibits enhanced internalization compared to the B subunit pentamer alone, underscoring the functional importance of the intact toxin in cellular entry [105]. Following endocytosis, the Stx-Gb3Cer complex is trafficked via a retrograde pathway through early endosomes and Golgi apparatus to the endoplasmic reticulum [12, 59]. The retrograde transport is essential for Stx toxicity, and it is dependent on the presence of Gb3Cer; toxin uptake in the absence of this receptor results in trafficking blockade and reduced toxicity [104]. Withing the Golgi apparatus, the A subunit of Stx is proteolytically cleaved by the membrane-anchored protease furin, generating the A1 fragment that remains linked through a disulfide bond to

the A2 chain, hence maintaining the holotoxin structure until reduction of this bond occurs in the ER [106]. The protease-sensitive region of the Stx A subunit can also undergo cleavage within the intestinal mucus, where host-derived proteases may initiate the nicking process prior to cellular uptake [107]. Subsequently, the A1 fragment is translocated from the ER lumen into the cytosol [108]. In cytoplasm, the enzymatically active A1 fragment exerts its rRNA N-glycosidase activity by specifically removing a conserved adenine residue within the sarcin loop of the 28S rRNA of the 60S subunit [109]. This depurination irreversibly impairs ribosome function by preventing the elongation factor binding and blocking protein synthesis, triggering a ribotoxic stress response [109].

Beyond translation inhibition, in endothelial cells Stx induce changes in gene expression, including chemokines and cytokines encoding genes [110]. Microarray profiling revealed significant upregulation of 25 pro-inflammatory genes following Stx1 and Stx2 exposure, including chemokines such as IL-8 and MCP-1, which mediate leukocyte recruitment, adhesion molecules as E-selectin and VCAM-1, which facilitate platelet and leukocyte binding, and mediators involved in apoptosis [110]. These changes are largely driven by activation of NF-κB and AP-1 transcription factors, promoting cytokine release and amplifying vascular inflammation [110, 111]. Such gene expression patterns can explain the pro-thrombotic and pro-inflammatory phenotype observed in injured endothelial cells during HUS. The ribosomal damage induced by Stx activates multiple cellular signalling cascades, including the MAP kinases pathways, which contribute to proinflammatory and proapoptotic outcomes [12, 110-112]. In human endothelial cells, the A1 fragment of Stx has been shown to target DNA beside ribosomal RNA, by removing multiple adenines from the nucleic acid strand to induce DNA fragmentation [113, 114]. The depurination doesn't directly cleave the DNA but weakens the integrity of the sugar-phosphate backbone, potentially causing spontaneous strand break [114]. Furthermore, the ribosome inactivating toxicity is accompanied by activation of key apoptotic mediators such as caspase -3, -6, -8, and -9, and induction of DNA damage-inducible gene products like GADD153/CHOP, linking ribosomal damage to programmed cell death [115]. Following bacterial ingestion and toxin release into circulation, the molecular basis of Stx cytotoxicity is tightly linked to its receptor-mediated endocytosis, retrograde trafficking, ribosomal depurination, and induction of both inflammatory and apoptotic pathways, which together underline their potent pathogenicity. Figure 3 summarizes the entire process from STEC ingestion to end-organ damage.

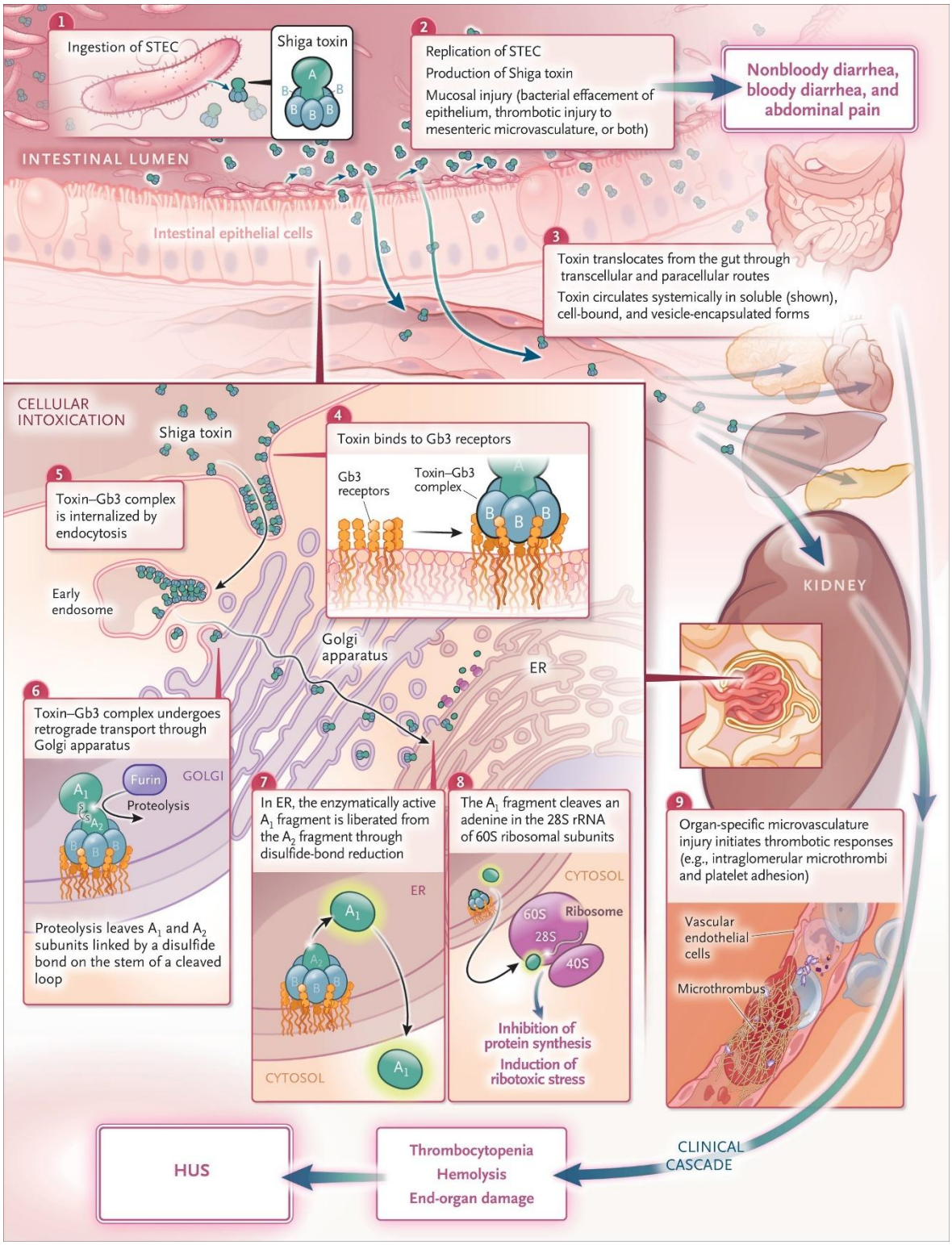

Figure 3.

Mechanisms of microvascular damage in STEC infections. Pathogenic STEC enters the body through contaminated sources (1). Bacteria multiply within the gastrointestinal tract, producing Stx subtypes 1 and/or 2, with subtype 2 causing more severe human disease (2). Released toxins enter the bloodstream (3). Stx attach to Gb3Cer receptors on cell surfaces via its B subunit (4). Receptor-bound Stx complexes are internalized into early endosomes (5), which transport them to the Golgi

complex (6), where furin protease cleaves them, separating A1 and A2 fragments that remain connected by a disulfide bridge. Processed toxins transfer to the endoplasmic reticulum (ER), where the disulfide connection between A1 and A2 fragments breaks (7). The released, catalytically active A1 fragment then cleaves an adenine residue from 28S rRNA within the 60S ribosomal subunit, blocking protein synthesis (8). Blood vessel damage resulting from disrupted protein synthesis and/or inflammatory activation creates microscopic clots (9). Platelet consumption and red blood cell destruction cause thrombocytopenia and anemia, while microthrombi lead to organ dysfunction. Reproduced from [10].

Shiga toxins interact with multiple blood components leading to overt HUS

Binding of Shiga toxins to soluble blood factors: Toll-like receptor 4 (TLR4) and human serum amyloid P component (HuSAP)

Beyond Gb3Cer-expressing circulating blood cells, human neutrophils can also bind Stx despite lacking the specific glycosphingolipid receptor [116, 117]. Their involvement in HUS is supported by evidence from patients, in whom neutrophils appear activated, degranulated, and less responsive to additional stimuli [118]. Moreover, neutrophils bearing Stx on their membrane have also been detected in STEC-infected individuals [119]. This interaction is mediated by Toll-like receptor (TLR) 4, which binds the A subunit of the toxin without promoting internalization, in contrast to the Gb3Cer-dependent binding of the B subunit, which facilitates endocytosis [120]. In the context of HUS, neutrophils are not the only cells expressing TLR4; this receptor is also located on the surface of monocytes and platelets [116, 120]. Neutrophils are a subtype of polymorphonuclear leukocytes and constitute a fundamental component of the innate immune system. As the most abundant white blood cells in circulation, they serve as a primary line of defense against invading pathogens through rapid recognition and response mechanisms [90]. Like many immune and non-immune cells, neutrophils express pattern recognition receptors (PRRs) on their surface, such as TLRs, which allow the specific detection of pathogen-associated patterns (PAMPs), conserved molecular motifs present on a broad variety of microorganisms, including bacteria, viruses, fungi, and parasites [90, 121]. Stimulation by PAMPs leads to the activation of membrane-bound TLRs [121]. The activation of TLRs not only leads to the release of mediators such as cytokines and chemokines, which regulate the immune response and promote inflammation, but can also induce the upregulation of certain TLRs, such as TLR4, on the cell surface, as well as the production and release of soluble forms of these receptors (sTLRs) into the extracellular environment [121-123]. sTLRs can bind PAMPs with high affinity, effectively competing with their membrane-bound counterparts. By acting as decoy receptors, sTLRs help modulate the inflammatory response by preventing excessive activation of immune signaling pathways, thus contributing to the maintenance of immune homeostasis [121-123]. Among TLRs, TLR4 is best known for recognizing LPS, but it has also been found capable of binding Stx [120-122]. In colonic carcinoma cell lines and primary human umbilical vein endothelial cells, TLR4 has been shown to enhance Stx

binding to Gb3Cer, suggesting its role as co-receptor in increasing the rate of Stx uptake in renal endothelial cells, which also express TLR4 [124]. Together with the well-known effects induced by LPS, the recognition of Stx by TLR4 expressed by neutrophils was shown to increase the levels of CXCL8, CCL4, TNF-α and G-CSF, supporting the pro-inflammatory effects in the context of STEC-infections and HUS [120]. Furthermore, sTLR4 was demonstrated to inhibit the binding of Stx to neutrophils [122].

Among the soluble components of human blood, the pentraxin human serum amyloid P component (HuSAP) has been identified as a negative regulator of Stx2a, but not Stx1a, due to its ability to bind this toxin subtype and reduce its cytotoxic activity [125, 126]. Simultaneously, HuSAP resulted in enhance binding of Stx2 to TLR4 expressed on human neutrophils [127]. HuSAP circulates in the bloodstream at stable concentrations, and is composed of two pentagonally-arranged subunits [125]. Even at low concentrations, HuSAP has been shown to inhibit the cytotoxic activity of Stx2a *in vitro* and to confer protection in animal models against its lethal effects [125, 128]. Interestingly, the binding between HuSAP and Stx2a involves both the A subunit and the B pentamer of the toxin, indicating a broad recognition interface [126]. sTLR4 has been shown to be capable of interfering with the binding of Stx2a by HuSAP, thereby allowing the toxin to retain its ability to interact with Gb3Cer-expressing target cells [122]. However, once the Stx2a-HuSAP complex is established, the sTLR4 is no longer able to displace HuSAP from the toxin [122]. Soluble TLR4 may form complexes with Stx2a either during the intestinal phase of STEC infection, following local release by activated macrophages, or through detachment from membrane-bound TLR4 on circulating immune cells via proteolytic cleavage or extracellular vesicles (EV) release (discussed in the next section) [122]. These mechanisms could allow Stx2a to evade HuSAP-mediated neutralization and retain its ability to bind target cells [122].

Shiga toxins interact with circulating blood cells leading to aggregate formation and extracellular vesicles (EV) production

Although Stx are the key mediators of vascular endothelial damage, they are rarely detectable in the serum of STEC-infected patients during the acute phase of HUS [129, 130]. Only 50% of the individuals with HUS during the acute phase showed to have free Stx (ng/mL) in the bloodstream, as demonstrated by ELISA (enzyme-linked immunosorbent assays) and by functional assays measuring protein synthesis inhibition in human cells [131].

Stx not only circulate in free form during early infection but are also associated with different blood circulating cells, including neutrophils, platelets, monocytes and erythrocytes [132]. During early toxemia, Stx reach the bloodstream and bind to erythrocytes, leukocytes, and platelets via Gb3Cer or TLR4, leading to cellular activation [89-92]. Monocytes and platelets express both receptors, allowing direct interaction with the toxin, whereas neutrophils, though lacking Gb3Cer, are activated through TLR4-mediated pathways [120]. This interaction promotes two major pathogenic mechanisms: the formation of cellular aggregates and the release of Stx-containing EV, both of which facilitate toxin dissemination and contribute to disease progression [132].

One of the striking features of typical HUS patients is the appearance of circulating aggregates composed of leukocytes and platelets [133]. The binding of Stx to blood circulating cells results in their activation, promoting the upregulation of adhesion molecules, such as P-selectin and integrins, which enhance cell–cell interactions [133]. On the other hand, the activation of these cells promotes the formation of microthrombi and thrombocytopenia, two hallmarks of HUS [92, 133]. Additionally, the formation of platelet–monocyte and platelet–neutrophil aggregates is not observed under normal physiological conditions [92, 134]. These aggregates have been consistently observed in children during the acute phase of HUS and are notably absent following recovery [133]. *In vitro* studies corroborate these clinical findings, showing that exposure of whole blood to Stx2 and/or STEC-derived LPS synergistically promotes aggregate formation [133]. Importantly, these aggregates have been shown to carry Stx, and this further supports the concept that monocytes, neutrophils, and platelets individually bind the toxin [133]. The interplay between activated platelets and leukocytes is central to the initiation of thrombosis and of inflammatory responses, a defining feature of HUS pathophysiology. As discussed in the next paragraph, beside Stx, blood cell aggregates can also contain additional cell-damaging factors which can exacerbate the toxic effects of Stx at cellular level.

A second key effect of the activation of circulating blood cells by Stx is the production of EV, a clinical signature in the onset of HUS [132]. EV are a heterogeneous group of small or large, membrane-surrounded particles released by many cell types and have been found in many biological fluids, such as blood, urine, seminal fluid, breast milk, saliva, and amniotic fluid [135-137]. They are broadly classified into exosomes, microvesicles, and apoptotic bodies, based on their size, origin, and biogenesis. Exosomes (30-100 nm) arise from the fusion of intracellular multivesicular bodies with the plasma membrane, while microvesicles (100-1000 nm) are shed directly from the plasma membrane

after budding, often in response to cellular activation, stress, or injury [135-137]. In contrast, apoptotic bodies (>1000 nm) are generated during programmed cell death and contain cellular components [135-137]. However, these distinctions are increasingly viewed as imprecise due to overlapping physical characteristics and the limitations of current isolation methods. Recognizing this, MISEV2023 recommends describing EV populations based on the centrifugation parameters (expressed in relative centrifugal force, g) used during their isolation, rather than attempting to assign vesicles to a specific subtype based on size or on specific markers [138]. This approach improves reproducibility and facilitates more accurate comparisons between studies, especially when biogenetic origin cannot be experimentally confirmed [138]. The composition of EV reflects their cell of origin, often containing specific proteins, surface receptors, lipids, and nucleic acids such as mRNA and microRNA [135, 138]. Through this molecular cargo, EV facilitate intercellular communication both locally and systemically [135, 137, 138]. Additionally, vesicle release may serve as a cellular defense mechanism, allowing cells to eliminate toxic or unwanted substances [135, 138]. A large body of evidence implicates EV as active mediators in numerous pathological conditions, including cancer, cardiovascular and renal diseases, and systemic inflammatory disorders [135, 137, 138].

In the context of STEC infection and HUS, large-sized EV have emerged as important contributors and, by carrying Stx to target organs they are now recognized as the main factors responsible for the transition from bloody diarrhea to HUS in STEC-infected patients [131, 133, 139]. Thus, Stx can trigger the release of large-size Stx-containing EV, thereby promoting the intoxication of distant target organs, such as the kidney [131-133, 139]. Notably, the large-sized EV released into circulation can transfer their toxic cargo to vascular targets via receptor-mediated endocytosis, exerting the Stx typical cytotoxicity in a manner equivalent to free toxin [132]. These structures, which can carry Stx either on their surface or in their lumen, contribute not only to toxin dissemination but also to immune activation and endothelial injury, reinforcing their critical role in the pathophysiology of HUS [131, 132, 139]. Indeed, the binding of Stx to monocytes via Gb3Cer and TLR4 receptors leads to the overproduction of potent pro-inflammatory cytokines, such as IL-1 and TNF-α [91, 120, 140, 141]. These mediators subsequently upregulate Gb3Cer receptor expression on endothelial cells, thereby increasing their vulnerability to toxin-mediated injury [140-142]. Accordingly, elevated levels of circulating large-sized vesicles have been identified in patients with overt HUS, primarily originating from platelets, and to a lesser extent from leukocytes and erythrocytes [139]. Supporting this mechanism, large-sized

vesicle carrying Stx2 have been identified within both glomerular and peritubular endothelial cells, helping to explain the severe damage observed in glomeruli and renal tubules during HUS [139]. *In vitro*, it has been demonstrated that large-sized EV derived from activated platelets and leukocytes are taken up by human glomerular endothelial cells leading to inhibition of protein synthesis and cell death [131, 139]. Morphologically, these vesicles are rounded and approximately 1 μm in diameter, as shown by transmission electron microscopy, a technique that enables detailed structural visualization [139]. However, since the latter analysis shows limited ability in assessing population-wide prevalence, supplementary approaches such as nanoparticle tracking analysis are necessary for comprehensive characterization. Nevertheless, based on their size, these vesicles most closely resemble microvesicles [139].

A quantitative assessment of EV in HUS revealed distinct contributions from circulating blood cells based on their size, lifespan, and shedding efficiency [132]. In pediatric patients, the ratio between the volume of vesicles of 1 μm in diameter (0.52 fl) and that of the different circulating cells have been considered. For leukocytes and erythrocytes, this ratio ranges from 1 to 150 up to 1 to 700, while for platelets it is around 1 to 15, suggesting physical limits on the number of EV each cell can release [132]. When adjusted for pediatric blood cell counts, analysis of EV release in typical HUS patients revealed that monocytes and neutrophils could generate more vesicles per cell than platelets or erythrocytes [132]. Although platelet-derived vesicles are the most abundant in circulation, platelets demonstrate a lower efficiency of vesicle shedding compared to monocytes and neutrophils [132]. *In vitro* studies performed by treating healthy donor blood with Stx2 showed similar patterns of EV release, confirming these observations [139]. By their intercellular communication properties EV could also promote the pathogenic cascade observed in HUS [143]. It has been proposed that Stx2, through interaction with its receptors Gb3Cer and TLR4, enhances the basal release of vesicles from circulating blood cells [132]. Taken together, these findings position large host-derived EV as efficient vectors for Stx dissemination, and active participants in endothelial injury, thrombosis, inflammation, and renal damage during the pathogenesis of HUS.

To characterize the *in vivo* dynamics of Stx during natural infection, 20 pediatric patients infected with STEC were monitored from the prodromal intestinal phase characterized by hemorrhagic diarrhea to the development of HUS [131]. Although Stx2 was detectable in the serum of all patients, its presence in blood was not sufficient to trigger the onset of the syndrome [131, 144]. Kinetic analyses showed that the amount of Stx2 bound

to leukocytes decreased as serum levels of functionally active Stx2 and soluble TLR4 increased [131]. In patients who progressed to HUS, EV-associated Stx2 appeared one day prior to the onset of the syndrome, paralleling the reduction in leukocyte-associated toxin [131]. This shift may reflect the direct transfer of Stx2 from circulating cells to Gb3Cer-expressing cells, as demonstrated *in vitro* during neutrophil transmigration through endothelial cell monolayers or, more likely, the incorporation of the toxin into EV [88, 131]. However, considering the relatively low rate of large-vesicle production, the latter process alone is unlikely to account for the rapid decline in circulating cell-bound toxin immediately before HUS onset [131, 132, 139]. It is worth noting that, in serum, toxicity correlates more strongly with EV abundance than with total Stx2 levels, suggesting that the vesicle-associated form represents the most pathogenic circulating toxin species during the transition from diarrhea to overt HUS [131].

The presence of Stx2 on large-sized EV has been confirmed through the use of monoclonal antibodies targeting the toxin [131]. EV interact with target cells via multiple mechanisms, including direct contact, receptor-mediated interactions, and endocytosis [136, 137]. Stx2 recognizes target endothelial cells through Gb3Cer which binds the B subunit. The mode of attachment of the toxin to the vesicle can determine which part of the toxin is externally exposed [131, 132]. Thus, EV derived from monocytes and platelets, which express both TLR4 and Gb3Cer, can carry Stx2 anchored through A subunit (via TLR4) or B subunit (via Gb3Cer) and thus alternatively exposing the uncommitted subunit. In contrast, vesicles released from neutrophils, which express only TLR4, are bound via A subunit and expose the B subunit on their surface [131, 132]. In patients, the vesicles most frequently detected prior to HUS onset displayed the B subunit externally [131]. Given the higher concentration of HuSAP compared to free Stx2 found in patients' blood, the serum toxicity observed in patients appears to be primarily due to Stx2 bound to TLR4 within Stx2-containing EV [132]. Finally, the incorporation of Stx2 into patient-derived EV, followed by the interaction between Stx2 and TLR4 may also allow the toxin to evade HuSAP inhibition, thereby facilitating its targeting of renal endothelial cells that express Gb3Cer [132]. A schematic overview of Stx interactions with circulating blood cells, including neutrophils, monocytes, and platelets, their respective receptors (Gb3Cer and TLR4), and the subsequent budding of Stx-containing EV, is shown in Figure 4.

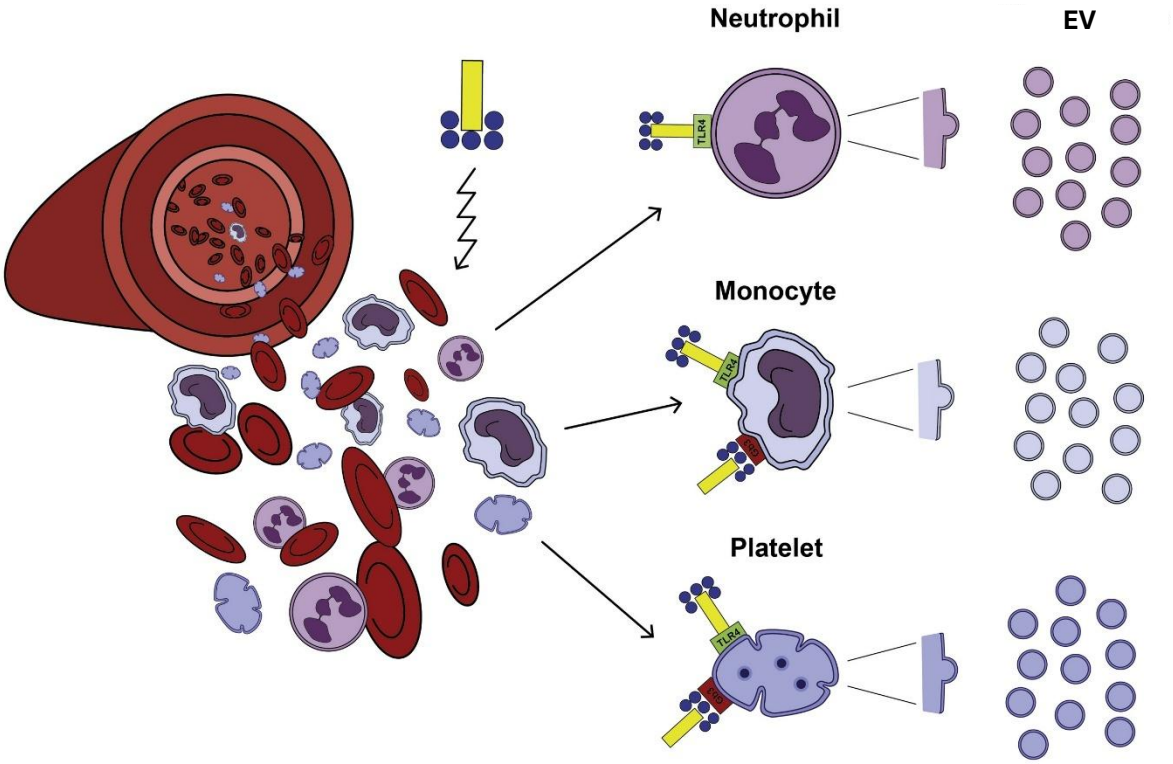

Figure 4.

Overview of Stx interactions with blood cells in STEC-infected patients. Stx bind circulating blood cells and platelets through Gb3Cer (red), expressed on monocytes and platelets, and TLR4, expressed on monocytes, platelets, and neutrophils. The B subunit of Stx interacts with Gb3Cer, while the A subunit binds TLR4. These interactions trigger the release of EV from activated cells, promoting toxin spread and disease progression. Modified from [132].

Blood cell-derived EV bear other pathogenic factors beyond Shiga toxins

In addition to Stx, platelet–leukocyte aggregates and the large-sized EV involved in HUS also carry additional pathogenic factors that exacerbate Stx-mediated endothelial cytotoxicity [132]. The activation of circulating blood cells, followed by toxin binding, promotes the expression of tissue factor (TF), a transmembrane glycoprotein considered the primary initiator of the coagulation cascade, and thereby facilitating thrombin generation [133, 145, 146]. Although endothelial cells, blood monocytes, and other circulating cells do not typically express TF or store it intracellularly, TF expression can be induced in response to stimulation with various pro-inflammatory or pro-thrombotic agonists, including inflammatory cytokines, P-selectin, LPS, and Stx [133]. Thrombin not only converts fibrinogen into fibrin but also acts as a potent platelet activator [133]. Elevated thrombin

levels are commonly observed in prothrombotic conditions, including HUS, further emphasizing the link between inflammatory activation and widespread microvascular thrombosis. During the acute phase of HUS, circulating platelet–monocyte, platelet–neutrophil aggregates, together with large-sized EV expressing surface-bound TF have been identified in the blood of affected children, but not after recovery [133]. These patients also exhibited significantly elevated plasma levels of functional TF compared to healthy pediatric controls [133].

In the 80s of the last century, several studies showed elevated breakdown products of the complement factor C3 in patients with typical HUS, and the activation of the alternative complement pathway [147, 148]. Subsequently, low levels of C3 in sera and C3 deposition in renal tissues were found in patients with HUS, further supporting complement involvement and its systemic activation during the syndrome [149-151]. Clinical observations on 12 HUS patients during the acute phase showed that EV derived from platelets, leukocytes, and erythrocytes carried surface-bound C3 and C9, thereby suggesting that blood cell activation contributes to the amplification of the complement response [139]. Notably, C3 is primarily associated with platelet–leukocyte complexes [152]. Thus, activated complement components bound to the surface of EV may be transferred to endothelial target cells, contributing to cellular injury and intensifying the pathogenetic cascade typical of HUS [132, 139]. These findings were corroborated by *in vitro* experiments in which human blood stimulated with Stx1, Stx2, and STEC-derived LPS generated platelet–leukocyte aggregates and EV containing C3 and C9 [133]. Moreover, even the non-catalytic B subunit of Stx1 can induce complement deposition on blood cells and promote the release of complement-coated EV [133]. This suggests that toxin–receptor interactions are sufficient to initiate complement activation. Additionally, Stx2 has been shown to bind complement factor H at the membrane recognition region on host cells, impairing its negative regulatory function [153]. Experimental evidence indicates that exposure to Stx promotes endothelial synthesis of P-selectin, a mediator involved in platelet deposition and specific binding of complement component C3 [154]. As previously mentioned, Stx2 triggers the activation of the alternative complement pathway, resulting in the enzymatic cleavage of C3 into C3a and C3b fragments. Among these products, C3a is a potent pro-inflammatory factor, thereby amplifying the inflammatory condition associated with HUS [154]. A separate study demonstrated that Stx2 treatment of endothelial cells leads to a reduction in the expression of CD59, a critical inhibitor of MAC formation [155]. Therefore, Stx2 activates the complement cascade and interferes with its regulation by downregulating factor H and CD59, enhancing complement-

mediated endothelial injury in HUS [151]. The pathogenic effects of EV are further facilitated by the expression of Gb3Cer and TLR4 on renal endothelial cells, which allow EV-bound Stx to dock and deliver their toxic cargo, including TF, C3, C9, and Stx. A schematic overview of the EV, their contents, and interactions with renal endothelial cells is shown in Figure 5.

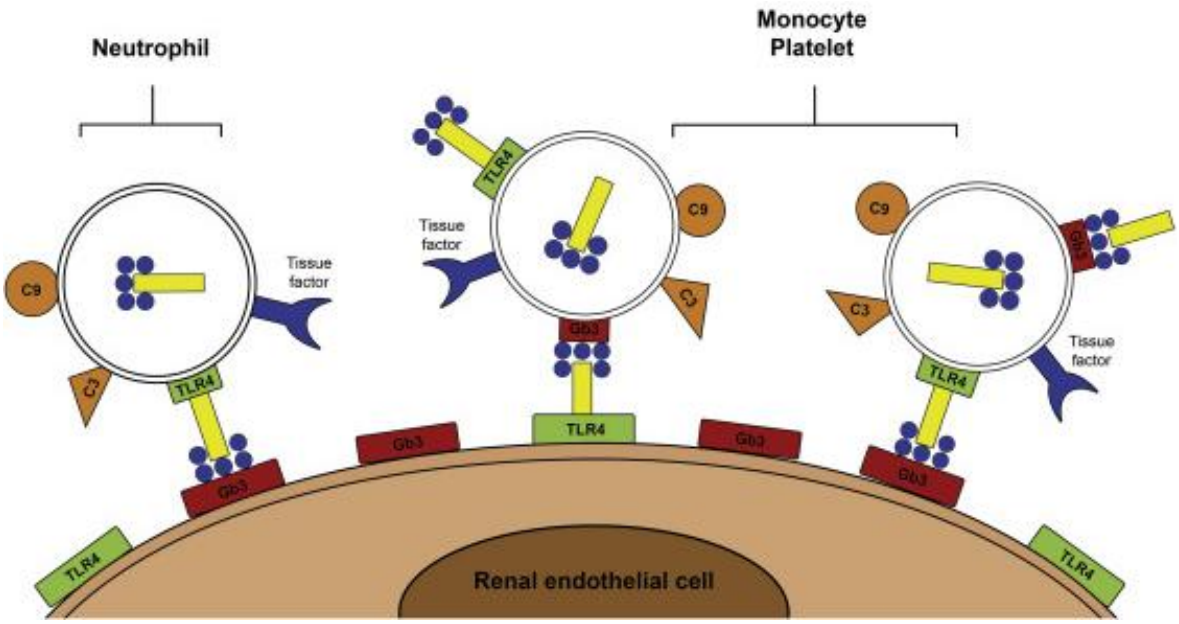

Figure 5.

EV released by platelets, monocytes, and neutrophils after Stx challenge and their interactions with renal endothelial cells. EV carry pathogenic factors, including C3 (orange triangle), C9 (orange circles), TF (blue cup), and Stx on their surface and inside. The Stx A chain (yellow) binds TLR4 (green), while the B chains (blue) interact with Gb3Cer (red). These receptors are present on EV and endothelial cells. Monocyte/platelet-derived EV can bind endothelial Gb3Cer via B chains of TLR4-anchored Stx and endothelial TLR4 via A chain of Gb3Cer-anchored Stx, whereas neutrophil-derived EV (lacking Gb3Cer) use only the former mechanism. Binding of EV enables delivery of toxic cargo to target cells and contributes to HUS pathogenesis. Modified from [132].

Different Shiga toxins, and their combination, account for different HUS risks and outcomes

Stx2 is well established as a key virulence factor associated with the development of HUS in humans [59, 77, 156]. However, STEC strains carrying different Stx2 subtypes exhibit distinct pathogenic profiles. Among the different known Stx2 subtypes, Stx2a is most

strongly linked to HUS, whereas Stx2c is only occasionally associated [156]. In contrast, Stx2d and Stx2e are commonly isolated from adults and primarily associated with mild or asymptomatic infections, sustained by STEC that typically lack the intimin-encoding *eae* gene [156]. The presence of Stx2d or Stx2e in the absence of the *eae* sequence may help predict a low risk of HUS, highlighting the diagnostic value of Stx2 subtyping [156]. Notably, the presence of Stx2 in both O157 and the major non-O157 serogroups (O26, O103, O111, O145) is significantly correlated with increased risk to develop HUS and bloody diarrhea in STEC-infected patients, underscoring the central role of Stx2 in STEC virulence [157]. Moreover, beyond subtype diversity, each Stx exists in two structural forms, native and cleaved, that differ in their biological behaviour. While both native and cleaved Stx2a demonstrate similar toxigenic effects on Gb3Cer-expressing cells (Vero and Raji), they differ markedly in their binding properties, resulting in distinct interactions with circulating cells and soluble serum components [97]. These structural differences also influence their capacity to promote platelet-leukocyte aggregate formation and incorporation into toxin-containing EV [97]. Stx2-cl does not interact with TLR4, preventing the toxin from communicating with circulating blood cells through this receptor, whereas it shows the capacity to bind CFH. In contrast, uncleaved native toxins exhibit opposite properties and promote the formation of leukocyte-platelet aggregates and Stx-containing EV pathogenesis [97]. Moreover, the cleaved form fails to bind human neutrophils indicating that the neutrophil-recognition site is likely located very close to the A subunit cleavage site, distinct from the toxin catalytic domain [97]. The uncleaved toxin capacity to induce leukocyte-platelet aggregates underscores TLR4 essential role, given its expression across all involved blood cell populations. In addition, both cleaved and native Stx2 interact identically with HuSAP, which simultaneously prevents Gb3Cer recognition [97, 125, 126, 128]. However, despite the strong rationale, current evidence remains insufficient to predict HUS onset based solely on the Stx2/cleaved Stx2 ratio [102].

Differently from Stx2, Stx1 is rarely associated with microangiopathic complications and is generally linked to milder clinical presentations [21, 23-25]. Thus, the risk of HUS in STEC infections depends more on the specific Stx type encoded by the prophages than on the bacterial strain itself. Epidemiological data consistently show a strong association between STEC harboring the Stx2 gene and severe disease outcomes, including progression to HUS [21, 23, 25]. Between 2010 and 2019, a STEC screening program for children (<20 years) with bloody diarrhea was conducted across 63 pediatric units in Northern Italy, covering a referral population of 2.3 million individuals [24]. The program focused on early

Stx detection prior to HUS diagnosis and Stx-positive patients were closely monitored until diarrhea resolution [24]. Molecular diagnostics performed on stool samples included reverse dot blot analysis and real-time PCR assays, targeting multiple STEC virulence factors, including *stx1* and *stx2* genes [24]. A total of 214 children presenting with bloody diarrhea tested positive for Stx. Among these, 29% were positive for Stx1, 45.3% for Stx2, and 25.7% for both Stx1 and Stx2 [24]. HUS developed in 15.9% of cases but strikingly none of the children carrying Stx1 alone progressed to HUS, whereas 23.7% of those with Stx2 and 12.7% of those with both Stx1 and Stx2 developed the syndrome (p = 0.001) [24]. The presence of Stx2 was significantly associated with the development of HUS, particularly when detected in association with STEC O26, which accounted for 34.5% of all HUS cases [24]. These findings suggest that the milder clinical outcomes observed in patients infected with STEC strains producing both Stx1 and Stx2 may result from an antagonistic effect of Stx1, which could mitigate the pathogenicity of Stx2 and ultimately reduce the risk of HUS development. To test this hypothesis, Petro C. et al. used the *E. coli* O26:H11 strain TW08571, which produces both Stx1a and Stx2a, to investigate the influence of Stx1a on Stx2a toxicity *in vitro* and *in vivo* [158]. Neutralization of Stx2a protected infected mice from lethality, confirming its dominant role in virulence [158]. In contrast, neutralization of Stx1a increased disease severity and morbidity, indicating that Stx1a exerts a protective effect [158]. Moreover, treatment with 2 × LD_{50} of Stx2a resulted in reduced lethality only in animals pretreated with the Stx1a B subunit, suggesting that Stx1a may compete with Stx2a for binding to target organs and thereby attenuate toxicity [158]. Consistently, administration of different doses of Stx2a toxoid and Stx1a B subunit protected Vero cells from Stx2a in a dose-dependent manner, further supporting the *in vivo* findings [158]. In a different experimental setting, the oral co-administration of fluorescently labeled Stx1a and Stx2a showed similar distribution in BALB/c mice tissues, suggesting that biodistribution is not sufficient to explain the observed differences in toxicity [159]. Additionally, mice treated with Stx2a alone displayed elevated blood urea nitrogen and serum creatinine levels, indicating significantly impaired kidney function compared to animals treated with both toxins [159].

Taken together, these results suggest that competition for toxin receptors or interference with toxin internalization may underline the protective effect of Stx1. Laboratory findings have confirmed the protective role of Stx1 in mitigating the deleterious effects associated with Stx2; however, the precise mechanisms remain unclear, as well as the role of Stx1 in Stx2-containing EV.

From diagnosis to therapeutic treatments

Laboratory and clinical diagnosis of STEC infections and associated HUS

Early recognition of STEC infections is essential for early management and to minimize the risk of HUS [160]. Diagnosis currently relies on the integration of clinical presentation with laboratory and microbiological testing [160].

Initial evaluation should include baseline tests such as hemoglobin, hematocrit, platelet count, serum urea, serum creatinine, electrolytes, and a peripheral blood smear to assist in diagnosis and establish reference values for monitoring disease progression [10, 160]. These parameters should be reassessed after 24 to 48 hours, as early microangiopathic changes may present as a decline in hemoglobin and platelet levels or an increase in serum creatinine, even when initial results are within normal limits [160]. The diagnostic hallmarks are non-immune hemolytic anemia with a hematocrit below 30%, fragmented erythrocytes on the peripheral smear with a negative Coombs test, thrombocytopenia with a platelet count below 150,000 mm^3, and evidence of acute kidney injury indicated by serum creatinine above the age-adjusted reference range, which may occasionally be accompanied by hypocomplementemia [10, 160]. Confirmation of STEC infection requires further stool and serological testing.

Laboratory diagnosis typically involves culture-based isolation of the organism, combined with nucleic acid amplification assays targeting *stx* genes [161]. Because detection sensitivity declines quickly after diarrhea onset, stool samples should be collected as soon as possible [160]. A detailed patient history can identify exposures to STEC-related high-risk factors, such as the consumption of unpasteurized dairy products, undercooked beef, raw vegetables, contact with symptomatic individuals, livestock, or contaminated water. Stool testing is recommended for patients presenting bloody diarrhea and for children with nonbloody diarrhea accompanied by tenesmus or severe abdominal pain [162]. Notably, the absence of fever does not exclude STEC infection [163]. If stool specimens are unavailable, rectal swabs may be used initially, but confirmatory stool testing should follow promptly [160, 164]. Enrichment of samples in broth generally enhances detection sensitivity compared to direct testing on collected samples [165]. The non-sorbitol-fermenting O157:H7 serotype, which is most strongly associated with the development of typical HUS, is identified on selective agar plates within 24 hours and subsequently confirmed using O157-specific agglutination [29]. Non-O157 serotypes (such as O26, O45, O103, O111, O121, O145) can be detected using O-specific antisera [166]. Enzyme immunoassays

differentiate between Stx1 and Stx2, while real-time PCR is widely used for *stx* gene detection due to its sensitivity and subtyping capacity [21, 165]. Multiplex PCR assays may also detect *eae* (intimin) and *hly* (listeriolysin O) genes, and *ipaH* (invasion plasmid antigen H) gene may help in excluding *S. dysenteriae* and enteroinvasive *E. coli* [21, 165]. Hemoglobinuria, detected by urine dipsticks, can serve as an early marker of renal involvement [21]. Although fecal diagnostics offer a noninvasive screening method, they may underestimate STEC infections since HUS typically develops 5–13 days after diarrhea onset, while bacterial counts and toxin amounts decline rapidly within the first week [160, 165]. Consequently, a negative stool test does not exclude STEC infection in patients with suspected HUS. Serological testing improves stool analysis by detecting immunoglobulin M and immunoglobulin A against LPS antigens from prevalent STEC serogroups [165]. Combining serology with stool culture increases diagnostic yield, with advanced glyco-linked ELISA assays increasing detection rates for O157 infections to nearly 90% [167]. Serology is particularly useful for identifying non-O157 infections, such as O26, O145, and O111, that are often missed by culture alone [167]. Mass spectrometry techniques like MALDI-TOF have recently enhanced diagnostic capabilities by rapidly distinguishing O157:H7 from other STEC serotypes with minimal sample preparation [168]. Although MALDI-TOF cannot differentiate individual Stx variants and is not yet widely adopted, its high processivity makes it well suited for routine screening [168]. Complementary methods including sandwich ELISA and immuno-PCR provide sensitive Stx subtyping, with immuno-PCR demonstrating significantly higher sensitivity than ELISA [169]. Each diagnostic approach presents advantages and limitations: culture offers definitive identification but is time-consuming; ELISA can exhibit cross-reactivity; PCR is highly sensitive but susceptible to inhibitors; and MALDI-TOF provides rapid results but lacks detailed subtype resolution [160]. Given the limitations of the mentioned techniques, rapid and point-of-care diagnostic tools that provide accurate and immediate results are urgently needed to enable timely treatment and prevent HUS progression.

Advances in plasmonic biosensors for rapid Shiga toxin detection

In the field of biosensors, plasmonic surfaces composed of gold or silver have become valuable tools for detecting extremely small quantities of analytes [170]. When light strikes these noble metals, it excites the free electrons in the metal, causing them to oscillate collectively. This collective electron is known as a plasmon [171]. When the frequency of the incident light matches the natural frequency of this oscillation, a strong resonance called localized surface plasmon resonance (LSPR) occurs [171]. At resonance, the nanoparticle absorbs and scatters light very strongly, creating an intense electric field near its surface. LSPRs are sustained by a hybrid wave made of electrons and light traveling along the interface between the metal and the surrounding material [171]. This confinement allows plasmons to be concentrated into regions smaller than the wavelength of light, surpassing conventional diffraction limits and generating extremely strong electromagnetic fields near the nanoparticle [171]. These intense near-fields form the basis for many sensing applications: when a molecule binds or approaches the nanoparticle, the resonance shifts slightly, altering optical properties and enabling both qualitative and quantitative detection [171]. A key application of plasmonic surfaces is surface-enhanced Raman spectroscopy (SERS), which combines Raman spectroscopy's molecular specificity with the strong signal amplification from plasmonic nanostructures [170-172]. This allows the detection of molecules even at very tiny amounts without the need for labels or dyes. Recent advances in nanofabrication allow precise control of plasmonic nanostructure size, shape, and composition, greatly enhancing their sensing performance [170, 173]. Their high sensitivity, selectivity, and miniaturization potential make plasmonic surfaces ideal candidates for biosensing. SERS signal enhancement arises mainly from two effects: electromagnetic enhancement, due to intense local fields from LSPRs, and chemical enhancement, caused by charge transfer between the adsorbed molecule and the metal [174, 175]. Designing new 3D nanostructures can further confine these fields, increasing sensitivity and enabling compact diagnostic devices [170, 173].

Related to STEC infections, rapid, on-site diagnosis is essential for timely treatment and preventing disease progression, making point-of-care tools that deliver fast and accurate results highly desirable. Very few studies have reported using LSPR properties to detect Stx or *stx* genes, and even fewer have combined this approach to SERS strategies [176]. Recently it was developed a novel plasmonic SERS substrate capable of detecting Stx2a with a limit of detection (LoD) of 1.4 nM. Designing new plasmonic nanostructures may further lower the LoD of Stx2 but also expand the detection to Stx1 and Stx2-cl [170]. Given the

limitations of the conventional Stx diagnostic systems, which are time-consuming and require laboratory infrastructures, SERS-based plasmonic sensors could provide rapid, sensitive, and label-free detection directly at the patient's bedside, offering a promising strategy for timely clinical decision-making.

Clinical management of STEC-related HUS patients

Conventional strategies for patients presenting typical HUS

Currently, there is no targeted therapy that directly addresses the underlying pathophysiology of STEC infections. As a result, management of patients remains primarily supportive, aiming to stabilize the patient and mitigate complications [166, 177]. The main adopted therapeutic strategies in the clinical treatment of typical HUS patients include early volume expansion and renal replacement therapy [160]. Recent clinical treatments also include plasma exchange, eculizumab and antibiotics [160].

Initiating isotonic fluid expansion within the first four days following the onset of diarrhea, and continuing during the early progression of HUS, it has been shown to reduce the incidence of oligoanuric kidney failure and the need for dialysis in susceptible individuals, thereby improving short-term recovery and increasing favorable long-term outcomes [178]. Thus, identifying patients early in the course of the illness is essential to begin fluid expansion at the optimal time. However, once HUS is established, fluid administration must be carefully controlled, as fluid overload has been associated with increased mortality rates [179]. Dialysis of patients affected by typical HUS is performed to manage complications of acute kidney injury [160, 180]. Between 40% and 60% of patients with typical HUS require renal replacement therapy, which may involve peritoneal dialysis, hemodialysis, or continuous renal replacement modalities [181]. Clinical practice typically favors peritoneal dialysis in pediatric patients, whereas hemodialysis was more frequently employed in adults, as seen during the O104:H4 outbreak [182]. Continuous renal replacement therapy is considered the preferred modality for patients who are critical, particularly those presenting with multiorgan dysfunction and hemodynamic instability [183]. Eculizumab has been used in severe cases of STEC-HUS, particularly in patients with neurological involvement or multiorgan failure [184]. Reports describe rapid neurological improvement in some treated individuals, but larger retrospective studies have not demonstrated significant benefits in renal or hematologic outcomes [184]. Plasma exchange has been investigated as a potential

therapy of critical STEC-HUS cases, primarily for its capacity to remove circulating pathogenic factors such free circulating Stx, Stx-containing EV, proinflammatory mediators, and prothrombotic elements [185]. Despite its widespread use during the *E. coli* O104:H4 outbreak, particularly in adults, clinical evidence supporting plasma exchange in Stx mediated HUS is limited [186]. Further analyses suggested that improved outcomes were likely attributable to high quality supportive care rather than the intervention itself [186]. Nowadays, the use of antibiotics in STEC infections remains controversial, as they may worsen patient outcomes [10, 13, 74, 160]. Given the potential consequences, the following dedicated paragraph will discuss antibiotic use in STEC patients.

Recent studies have explored novel therapies for STEC-HUS, including anti-Stx antibodies, Gb3Cer receptor inhibitors, and Retro-2. By neutralizing Stx, antibodies offer a powerful therapeutic approach. The production of antibodies (Ab) mainly relies on three different approaches, including polyclonal (p) Ab, monoclonal (m) Ab, and recombinant Ab. pAb have advantages such as recognizing multiple epitopes and toxin variants; however, they may trigger immune reactions due to animal origins [160]. Chimeric mAb like Shigamabs® and urtoxazumab have demonstrated promising neutralizing effects in preclinical and early clinical trials, highlighting their potential for treating Stx-mediated diseases [187, 188]. Gb3Cer inhibitors represent a promising therapeutic approach against Stx toxicity by blocking glucosylceramide synthase, the enzyme responsible for Gb3Cer synthesis [189]. Drugs like eliglustat and miglustat reduce Gb3Cer expression in human renal and colon cells, protecting them from Stx2-induced damage [190]. The glucosylceramide synthase inhibitor C-9 reduces mortality and organ damage in animal models but showed limitations due to its side effects [191]. Small molecules Retro-1 and Retro-2 selectively inhibit retrograde transport of Stx from early endosomes to endoplasmic reticulum, protecting and improving survival from toxin effects in both cellular and mice models [192]. To overcome the poor Retro-2 solubility, Retro-2-containing nanospheres were developed, enhancing solubility and enabling effective toxin inhibition in the gut [193].

Although various approaches have been investigated for HUS treatment, none specifically target the key pathophysiological process underlying the transition from bloody diarrhea to overt HUS: the production of Stx-containing, host-derived EV. Targeting this process could offer a more precise and potentially effective direction for future therapeutic development.

Therapeutic dilemma: antibiotics in STEC-associated HUS

Since STEC are microorganisms, it may seem intuitive to administer antibiotics to quickly eradicate the infection and prevent Stx–mediated complications such as HUS. However, antibiotic use remains widely debated and is generally not recommended because certain antibiotics, such as quinolones, can trigger the bacterial SOS response by damaging DNA [10, 72, 74, 75]. As discussed in the section "The Shiga toxin family and its genetic diversity," activation of the SOS response induces temperate lambdoid prophages integrated into the STEC genome, which are normally quiescent and carry the *stx* genes responsible for toxin production. This activation leads to the phage lytic cycle, increasing *stx* gene expression and consequent release of toxins, thereby elevating the risk of HUS. Moreover, antibiotics can alter the host microbiota in ways that promote STEC adhesion to the intestinal mucosa, further exacerbating disease progression [160].

Observational and meta-analytic studies failed to specifically address the relationship between antibiotic administration and increased HUS risk in STEC-infected patients. Many of these studies are limited by small sample sizes, heterogeneous antibiotic regimens, and inconsistent diagnostic criteria for HUS [160]. In addition, confounding factors such as disease severity complicate interpretation, as patients with more severe illness are both more likely to receive antibiotics and more prone to developing HUS [160]. The absence of adequately powered randomized controlled trials with standardized methodologies further restricts the ability to draw definitive conclusions [160].

In addition, the impact of antibiotic class and dosage is another critical factor. Ciprofloxacin, a widely used fluoroquinolone, induces the bacterial SOS response *in vitro*, leading to prophage activation and increased Stx release; however, clinical findings remain inconsistent, with some studies indicating no elevated HUS risk or even potential therapeutic benefit [72, 194]. Notably, observational data following the 1996 E. coli O157 outbreak in Japan suggested that early fosfomycin treatment within the first 5 days of illness might reduce HUS risk [195]. Unlike fluoroquinolones, fosfomycin acts on bacterial cell wall synthesis. Currently, the use of fosfomycin in STEC patients remains controversial due to the lack of randomized controlled trials and the apparent discrepancy between in vitro and clinical observations, with fosfomycin's effects on toxin liberation varying across STEC strains and potentially influenced by host factors such as gut microbiota and mucosal immunity [195].

Given these differences, the employment of each antibiotic should be assessed individually, following the most standardized protocol. As a result, the relationship between

antibiotic therapy and HUS risk remains unresolved, highlighting the need for rigorously designed prospective studies to address this question.

The polymyxin B derivative NAB815: a potential novel tool in preventing HUS development

Polymyxin B is a potent antimicrobial agent with selective activity against Gram-negative bacterial [196]. It plays a significant role in modulating host–pathogen interactions by impairing the recognition of LPS by the TLR4 signaling complex [197]. Structurally, polymyxin B is a pentacationic cyclic lipodecapeptide bearing five cationic residues (Figure 6): three within the cyclic ring (residues R4 to R10) and two within the linear N-terminal segment (residues R1 to R3) [196]. Recently, polymyxin B has also been recognized for its capacity to inhibit the interaction between Stx2 and TLR4 [198]. However, its clinical application remains limited due to dose-dependent nephrotoxicity and neurotoxicity [199]. Moreover, effective inhibition of Stx2 binding to leukocytes occurs only at micromolar concentrations of the antibiotic, which also exhibit strong bactericidal activity, thereby complicating its therapeutic use in toxin-neutralizing strategies.

To reduce nephrotoxicity, a polymyxin B derivative named NAB815 was developed with a reduced number of positive charges [200]. In comparison to polymyxin B, which carries five cationic groups, NAB815 contains only three. This modification was obtained by replacing DThr with Dab^{+} at position R3 in the linear segment and substituting Abu for Dab^{+} at position R8 in the cyclic segment (Figure 6) [200, 201]. This modification significantly lowers toxicity to human kidney tubular cells, with an IC_{50} of 334 µg/mL, approximately 20 times lower than that of polymyxin B (18 µg/mL) [201]. In a 7-day study involving cynomolgus monkeys, the administration of NAB815 at 36 mg/kg/day (divided into three doses) was well tolerated, showing no notable changes in serum creatinine, blood urea nitrogen, or urinary biomarkers [202]. In contrast, animals treated with the parental drug, polymyxin B, at 18 mg/kg/day developed severe nephrotoxicity requiring euthanasia [202]. While still in the preclinical stage, NAB815 exhibits promise as a treatment for complicated urinary tract infections. In a mouse model of *E. coli*-induced pyelonephritis, NAB815 was found to be ten times more effective than polymyxin B, a difference attributed primarily to its significantly improved urinary elimination approximately tenfold higher than that of polymyxin B [203, 204]. Notably, polymyxin B shows a minimum inhibitory

concentration (MIC) values above 1 µg/mL against *E. coli* isolates [205], while NAB815 shows an MIC of 2 µg/mL against *E. coli* ATCC 25922 [206].

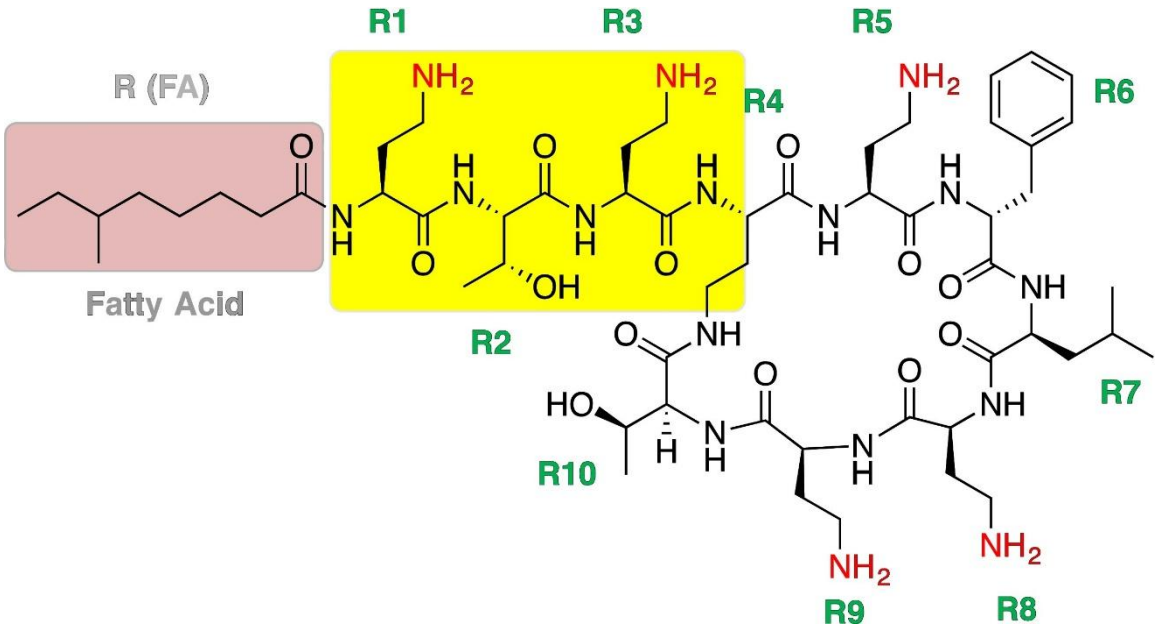

	L	R1	R2	R3	R4	R5	R6	R7	R8	R9	R10
Polymyxin B	MOA/MHA	-Dab$^+$	-Thr	-Dab$^+$	-cy[Dab	-Dab$^+$	-DPhe	-Leu	-Dab$^+$	-Dab$^+$	-Thr]
NAB815	OA	-Dab$^+$	-Thr	-DThr	-cy[Dab	-Dab$^+$	-DPhe	-Leu	-Abu	-Dab$^+$	-Thr]

Figure 6.

Structural representation of polymyxin B, separated into its lipidic tail, linear chain (R1–R3), and cyclic moiety (R4–R10) [207]. Underlined residues indicate positive charges, while red marks identify amino acidic substitutions. Abbreviations: MOA = methyloctanoic acid; MHA = methylheptanoic acid; OA = octanoic acid; Dab = 2,4-diaminobutyric acid; Thr = L-threonine; DThr = D-threonine; DPhe = D-phenylalanine; Leu = leucine; Abu = 2-aminobutyric acid. The symbol cy[…] indicates a cycle connecting the first and last residues in brackets (modified from [177]).

Regarding Stx-specific activity, NAB815 strongly inhibited the binding of Stx2a to neutrophils in a clear dose-dependent manner, even at sub-bactericidal concentrations [177]. The amount required to reduce toxin binding by 50% was approximately 60 times lower than that of polymyxin B [177]. Unlike the parent compound, NAB815 was able to prevent the formation of neutrophil–platelet and monocyte–platelet aggregates in human blood exposed to Stx2a, even at very low concentrations (as low as 0.01 µg/mL) [177]. At the same sub-

bactericidal dose, NAB815 had no damaging effect on red blood cells [177]. However, it led to a mild reduction in white blood cell viability, primarily linked to increased apoptosis, with minimal necrosis observed [177]. Nanoparticle tracking analysis of EV isolated from human blood exposed to 2 nM Stx2a, in the presence or absence of NAB815 (0.01 μg/mL dose), showed that NAB815 markedly reduced both the number and size of EV compared to treatment with Stx2a alone [177]. Quantitative capillary Western blot (WES) analysis of the isolated EV showed that samples from NAB815 and Stx2a-treated blood had lower levels of the EV marker Alix, as well as reduced amounts of toxic cargo proteins, including C3, C9, and Stx2a, compared to EV from blood treated with Stx2a alone [177]. The same analysis also revealed that NAB815 decreased the formation of EV derived from platelets and leukocytes [177]. Finally, EV isolated from Stx2a-treated samples were applied to Vero cells in viability assays, showing that the presence of NAB815 during blood treatment enhanced cell survival [177].

In conclusion, the *in vitro* studies highlighted the potential of NAB815 as a promising therapeutic candidate by targeting the formation of Stx2a-associated EV and reducing their toxic protein cargo, an event that represents a critical stage in HUS pathogenesis. Given that NAB815 is an antibiotic derivative, further investigation is necessary to clarify if its employment in STEC-infected patients could activate SOS response and increase Stx production. *In vivo* studies are crucial to assess the efficacy and safety of NAB815 in physiological conditions. These studies will be essential to assess both the therapeutic potential and the safety profile of NAB815 in the context of STEC infections.

Aim of the project

HUS is a severe complication of STEC infection, characterized by hemolytic anemia, thrombocytopenia, and acute kidney injury, and represents the leading cause of acute renal failure in the pediatric population. This project focuses on Stx, STEC, and HUS at three distinct but interconnected levels: pathophysiology of the disease, diagnostic improvement, and therapeutic intervention. At the pathophysiological level, it aims to explore the distinct contributions of Stx1a and Stx2a to the onset and severity of HUS. In parallel, the study seeks to develop sensitive diagnostic tools for early detection of circulating Stx and to assess the efficacy of a novel therapeutic approach in a CD-1 mouse model, with the goal of preventing the progression of the disease and reducing systemic complications.

Despite its clinical relevance, several mechanisms underlying HUS pathogenesis remain unclear. Epidemiological evidence indicates that the risk of HUS progression does not solely depend on the STEC serotype, but also on the type of Stx produced by the strain along with its associated virulence factors. Indeed, the risk of developing this multi-organ condition is highest in patients infected with Stx2-producing strains, negligible in those infected with those producing Stx1, and intermediate in patients infected with strains capable of producing both toxins suggesting a possible protective role of Stx1 against Stx2-mediated cytotoxicity. Moreover, it is well recognized that the transition from bloody diarrhea to HUS is marked by the appearance of large Stx2-containing EV in the bloodstream approximately one day before syndrome onset. To date, no studies have isolated and characterized human-derived EV in the presence of both Stx1 and Stx2. This thesis investigates whether co-exposure of human blood to Stx1a and Stx2a reduces leukocyte-platelet aggregate formation and the release of pathogenic EV compared to single-toxin exposure. Protein characterization of these EV may clarify epidemiological findings and confirm the apparent protective role of Stx1 in mitigating Stx2-induced effects.

Early identification of STEC infection and characterization of the specific Stx subtype are crucial to prevent severe complications such as HUS. Conventional diagnostic methods, however, are often labor-intensive, time-consuming, and require specialized facilities. In recent years, plasmonic biosensors based on SERS substrates have emerged as powerful tools for biosensing, due to their high sensitivity and ability to detect low levels of analytes. Moreover, a previous plasmonic substrate for SERS enabled the selective detection of Stx2a, achieving a detection limit of 1.4 nM. To further improve diagnostic performance, this project introduces a newly designed planar plasmonic metasurface for SERS analysis,

allowing the acquisition of molecular fingerprint spectra and precise differentiation of Stx1a, Stx2a, and cleaved Stx2a. Prompt recognition of the specific Stx subtype produced by STEC strains could therefore guide clinical focus toward patients at increased risk of HUS progression, enabling both targeted monitoring of disease progression and earlier intervention in those most likely to develop severe disease.

However, even with the rapid and specific identification of Stx achievable through SERS approaches, it remains essential to develop targeted therapeutic strategies for STEC-infected patients to prevent worse outcomes. Indeed, the clinical management of STEC-infected patients relies on non-specific therapies, with supportive care remaining the most widely adopted approach. Recent evidence demonstrated that polymyxin B can inhibit Stx2a binding to TLR4, a critical step for toxin internalization and the subsequent release of host-derived Stx-containing EV, the most pathogenic form of the toxin, responsible for HUS development. However, the clinical use of polymyxin B is severely limited by its high nephrotoxicity and neurotoxicity, which may even exacerbate patient outcomes. To overcome this limitation, a novel derivative, NAB815, was designed, showing significantly reduced toxicity compared to the parental compound. At a very low concentration of 0.01 μg/mL, NAB815 strongly inhibits Stx2a binding to neutrophils and prevents the formation of leukocyte–platelet and monocyte–platelet aggregates. It also significatively reduces the release of pathogenic Stx-containing EV. At this dose, red blood cell integrity is preserved, while white blood cell viability is only mildly affected. These combined effects highlight the potential of NAB815, demonstrating its therapeutic potential in preventing HUS progression. However, it is still unclear whether the protective effects of NAB815 observed in cell models are maintained *in vivo*. In this study, NAB815 was tested in CD-1 mice using two complementary experimental strategies: by assessing its ability to prevent the effects of particulate Stx, through injection of human blood-derived Stx2a-containing EV isolated in presence or absence with NAB815, and by evaluating its impact on free soluble Stx2a. Moreover, the evaluation included survival analysis, histopathological examination, and measurement of blood urea and creatinine levels to assess kidney involvement.

The administration of antibiotics in STEC-HUS patients is generally avoided due to the risk of inducing the SOS response, which can increase Stx production and worsen patient outcomes. A critical consideration in evaluating NAB815 arises from the fact that it is a derivative of the parental antibiotic polymyxin B. To assess its potential clinical applicability,

this study further investigates the effects of NAB815 on both engineered and clinically relevant wild-type *E. coli* strains producing Stx1a or Stx2a.

Overall, these investigations integrate the study of HUS pathophysiology, the development of sensitive diagnostic tools, and the evaluation of targeted therapeutic strategies, highlighting a comprehensive approach aimed at preventing disease progression and improving outcomes in STEC-infected patients.

Materials and methods

Purification of the toxins

Stx1a and Stx2a were obtained from *E. coli* strains C600-H19J and C600-933W, respectively (provided by Dr. Alison O'Brien, Department of Microbiology and Immunology, Uniformed Services University of the Health Sciences, Bethesda, MD, USA). Purification was performed using receptor analogue affinity chromatography: Stx1a was isolated on globotriose Fractogel (IsoSep, AB), while Stx2a was purified on cyanogen bromide–activated Sepharose coupled to bovine serum albumin (BSA) conjugated with terminal galabiose (Galα1-4Galβ-O-spacer—BSA, Glycorex, Lund, Sweden) [208, 209]. Both toxins were additionally processed through an ActiClean Etox column (Sterogene Bioseparations, Carlsbad, CA, USA) to reduce LPS contamination. Protein concentrations were determined by the Lowry assay, and residual LPS was quantified using the Limulus Pyrogen Plus amebocyte lysate test (Cambrex, Walkersville, MD, USA). The endotoxin level assessment showed low levels of LPS contamination, measured at 8.1 ng/mg for Stx1a and 4.9-6.5 ng/mg for Stx2a. Aliquots of purified toxins were stored at –80 °C in phosphate-buffered saline (PBS). Toxin dilution was performed with PBS supplemented with 1% BSA to prevent nonspecific binding to plastic tubes. Finally, cleaved Stx2a was obtained by incubating native Stx2a (120 µg) with trypsin (1 µg in 100 µL PBS, pH 7.5) for 1 h at 37 °C, followed the addition of the protease inhibitor phenylmethylsulfonyl fluoride (0.7 µg/mL, 10 min at 37 °C) [97].

Collection of blood samples from adult human donors

Blood samples anticoagulated with *CDP* (citrate-phosphate-dextrose solution) were collected from 18 healthy male adult volunteers at the Emilia-Romagna Regional Blood Centre, Maggiore Hospital (AUSL Bologna, Italy), after obtaining informed consent. The donors were allocated to three experimental groups based on the study objectives, and samples were used for the isolation of blood cell-derived EV containing Stx. Donors 1–6 (median age 57.5 years, range 40–66 years; ABO/Rh groups: 3 A+, 2 O–, 1 O+) were employed for pathogenesis studies investigating the modulatory effects of Stx1a on Stx2a-induced cellular responses. Blood from donors 7–10 (median age 51 years, range 24–60 years; ABO/Rh groups: 1 A+, 1 B+, 1 AB+, 1 O–) was used to isolate Stx2a-containing EV

for cell viability assays with NAB815, and for preliminary dose-response studies to determine appropriate EV concentrations for subsequent animal experiments. Blood from donors 11–18 (median age 47 years, range 19–56 years; ABO/Rh groups: 5 A+, 3 B+) was used to isolate Stx-containing EV for animal experiments.

Isolation of 10,400-20,800 × g EV from whole human blood exposed to Shiga toxins

To reproduce the formation of pathogenic EV observed in HUS patients, whole blood from healthy donors was diluted with an equal volume of Dulbecco's Modified Eagle Medium (DMEM; high glucose, without L-glutamine, with sodium pyruvate; Capricorn Scientific) supplemented with 10 µM Gly-Pro-Arg-Pro (GPRP; Merck), a fibrin polymerization inhibitor that prevents clotting without affecting cellular responses. For pathogenesis studies (donors 1–6), 40 mLof blood per experimental condition was incubated for 4 hours at 37 °C in the presence of either 1 nM Stx1a, 2 nM Stx2a, a combination of 2 nM Stx2a with 1 nM Stx1a, or vehicle as control. Following incubation, EV were isolated through sequential centrifugation: 2,600 × g for 35 minutes to remove platelets and blood cells, 10,400 × g for 25 minutes to clear cell debris and apoptotic bodies, and 20,800 × g for 1 hour to pellet large EV (10,400–20,800 × g fraction). The resulting pellet was resuspended in 500 µL PBS and divided into two 250 µL-aliquots which were further centrifuged at 20,800 × g for 40 minutes. One pellet was stored at –80 °C for protein analysis, while the other was resuspended in 34 µL PBS for nanoparticle tracking analysis (NTA). For NAB815 studies (donors 7–10) and animal experiments (donors 11–18), 80 mL of blood per condition was processed following the same dilution and incubation protocol. Samples were treated with either 2 nM Stx2a, NAB815 0.01 µg/mL, Stx2a + NAB815 combination, or vehicle as control. EV were isolated using the sequential centrifugation protocol described above. The 10,400–20,800 × g pellet was resuspended in 1 mL PBS, centrifuged at 20,800 × g for 40 minutes, and the final pellet was resuspended in 100 µL PBS and stored at –80 °C for subsequent experiments. Notably, at the experimental concentrations used (1 nM Stx1a and 2 nM Stx2a, corresponding to ~70 ng/mL and ~140 ng/mL, respectively), the estimated LPS contamination in the preparations translates into approximately 0.57 pg/mL for Stx1a and 0.7–0.9 pg/mL for Stx2a. These concentrations are orders of magnitude below those required to induce measurable TLR4-dependent activation in vitro, indicating that LPS contamination is unlikely to contribute to the observed effects [210].

Characterization of EV using nanoparticle tracking analysis (NTA)

EV obtained from the Stx1+Stx2 combination studies were characterized by NTA using a NanoSight RS300 system (Malvern Panalytical, Malvern, UK). Samples were diluted 1:1000 in PBS and filtered through a 0.1 μm membrane. For each sample, three 60-second videos were recorded, and data were analyzed with NTA software version 3.2 to determine particle size and concentration (particles/mL).

Preparation of EV lysates for protein analysis

Each EV pellet obtained from the Stx1+Stx2 studies marked for protein analysis was lysed by adding 25 μL of RIPA buffer (20 mM Tris-HCl, pH 7.5, 150 mM NaCl, 1 mM EGTA, 1% sodium deoxycholate, 1% NP-40) supplemented with cOmplete protease inhibitor cocktail (Roche, Sigma-Aldrich, USA). Samples were incubated for 10 minutes with gentle mixing every two minutes. Following incubation, cell debris was removed by centrifugation at 14,000 × g for 10 minutes at 4 °C. The resulting supernatant was collected and stored at –80 °C. Protein concentration of the EV lysates was determined using the Bradford assay, with BSA as the standard.

Quantitative assessment of EV proteins by capillary Western blot (WES)

Proteins from EV lysates derived from Stx1+Stx2 combination studies were analyzed using WES system (Biotechne). Protein solutions were first diluted in a master mix containing dithiothreitol and incubated for 5 minutes at 95 °C. Following the manufacturer's protocol, each well was loaded with the protein marker, sample, primary and secondary antibodies, antibody diluent for blocking, streptavidin-HRP, and Luminol-Peroxide mix. The Abs used for protein detection included rabbit polyclonal anti-Alix (1:50, Novusbio) as EV marker, and rabbit polyclonal anti-Stx2a (1:50, Dr. Stefano Morabito, ISS Rome) to detect Stx2a.

Fabrication and structural analysis of gold metasurfaces

The gold metasurface patterns, measuring 450 µm × 430 µm, were constructed as ordered hexagonal arrays of nanoelements exhibiting trigonal symmetry. These nanostructures, referred to as octupolars, were originally designed for second harmonic generation, a nonlinear optical phenomenon with relevant applications in surface characterization, and later adapted as a platform for biosensing [211]. Fabrication was obtained using the Raith 150 electron beam lithography (EBL) system. Each nanoelement consisted of three partially overlapping equilateral triangular nanoclusters with a side length of 200 nm (Figure 7A). A 150 nm layer of positive resist (styrene methyl acrylate, ZEP 520A) was applied to a 15 nm indium tin oxide (ITO)-coated glass substrate by spin coating, baked at 170 °C for 5 minutes, and then patterned with a 10.2 pA electron beam with an area dose of 30 µC/cm². The patterned resist was developed in n-amyl acetate, followed by a 90 second rinse in a 1:3 methyl isobutyl ketone:isopropyl alcohol solution and a 30 second wash with isopropanol. Gold deposition was carried out by electron beam evaporation (SISTEC CL-400C), applying a 2 nm chromium adhesion layer followed by a 50 nm gold layer. The resulting multilayer structure is illustrated in Figure 7B, and the main fabrication steps are summarized in Figure 7C. The minimum interparticle distance along the x-axis was 100 nm. Morphological characterization of the fabricated nanostructures was performed using scanning electron microscopy (SEM; Raith 150). The structure captured by SEM is shown in Figure 7D.

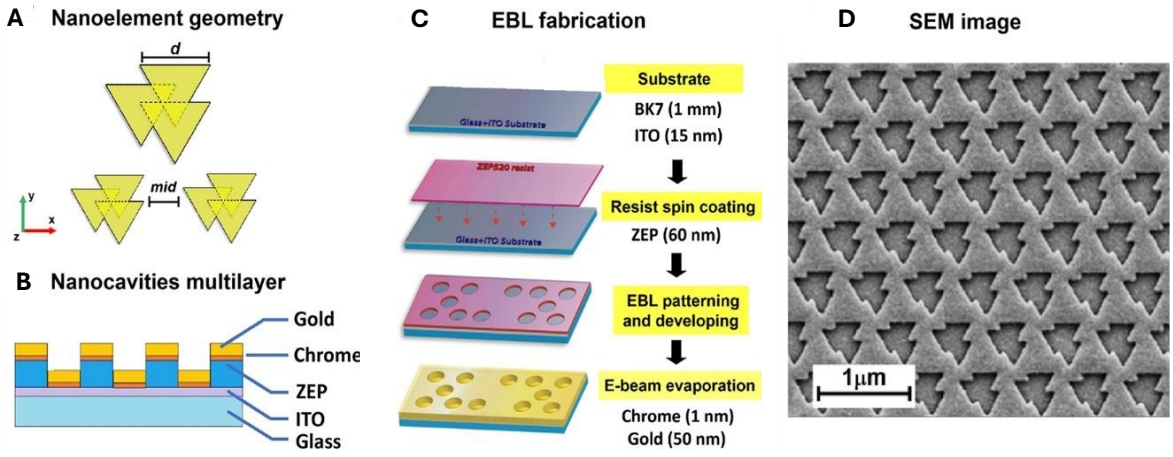

Figure 7.

(A-D) Plasmonic metasurface fabrication. **(A)** Illustration of the designed nanoelement geometry. **(B)** Multilayered nanocavities obtained after fabrication. **(C)** Key steps of the EBL fabrication process employed to create the metasurface. **(D)** SEM picture showing the final plasmonic metasurface structure. Modified from [170].

Functionalization of gold metasurfaces and acquisition of SERS spectra

The biosensor was modified by noncovalent functionalization of the nanopatterned gold surface via physisorption of mAbs specific for each Stx: Ab anti-Stx1a for Stx1a (Stx1–13C4; Toxin Technology, Sarasota, FL, USA), and Ab anti-Stx2a for Stx2a and cleaved Stx2a (Stx2–BB12; Toxin Technology, Sarasota, FL, USA). To achieve this, 50 µL of mAb (10 µg/mL in PBS) was deposited dropwise on the nanostructured chip surface and incubated overnight at 4 °C in a humid chamber to allow physical adsorption of the antibodies onto the gold surface. Excess of unbound antibodies was removed by washing the chip 5 times with 1 mL of bi-distilled water. To reduce nonspecific binding, the surface was subsequently blocked with 1% w/w BSA for 1 h at 25 °C in a humid chamber, followed by another wash step with bi-distilled water. Biosensor functionality was tested by exposing the modified surface to a toxin solution at a final concentration of 45 nM, incubated overnight at 4 °C in a humid chamber. After exposure, the chip was washed five times with 1 mL of bi-distilled water and dried under a nitrogen stream before the collection of SERS spectra.

Raman measurements were performed with a QE Pro-Raman spectrometer (Ocean Optics) integrated into an Olympus BX51 upright microscope operated in backscattering mode. Excitation was provided at 785 nm using a 1,200 lines/mm grating and a 50 µm entrance slit. The laser was focused on the sample with a 50× objective (N.A. 0.75), delivering 12 mW on the sample plane. For Stx detection, 40 SERS spectra were recorded from distinct positions across each sample, covering the 350–1,400 cm^{-1} spectral window, with an integration time of 10 s per acquisition. Raw spectra were subsequently corrected for baseline and averaged using a custom MATLAB (R2019b, MathWorks) routine. The applied laser intensity (≈1.7 × 10^3 W/cm^2) was verified not to induce detectable heating effects.

Vero cell cultivation and assessment of viability following Stx2-containing EV exposure

Simian (Cercopithecus aethiops) Gb3Cer-expressing Vero cells were provided by Dr. Stefano Morabito (European Reference Laboratory for *Escherichia coli*, Istituto Superiore di Sanità, Rome, Italy). Cells were cultured in DMEM (high glucose, without L-glutamine, with sodium pyruvate; Capricorn Scientific), supplemented with 10% fetal bovine serum (FBS), 2 mM L-glutamine, and 1% penicillin-streptomycin. Cultures were maintained at 37 °C in a 5% CO_2 atmosphere. Vero cells were seeded in 24-well plates at 50,000 cells per well

in a 500 µL final volume of medium. After 24 h, monolayers were treated with the previously isolated human-derived EV (donors 7-10; blood exposed to 2 nM Stx2a, NAB815 0.01 µg/mL, Stx2a + NAB815 0.01 µg/mL, or PBS) and incubated for 72 h to evaluate cell viability. Viability was assessed using the luminescent CellTiter-Glo® assay (Promega, Milan, Italy), which quantifies ATP as a marker of metabolically active cells. After incubation, the medium was replaced with 150 µL of fresh medium, followed by an equal volume of CellTiter-Glo reagent. Plates were shaken for 2 minutes to lyse cells, then 200 µL of the lysate were transferred to 96-well plates. After 10 minutes at room temperature, luminescence was measured to determine intracellular ATP levels.

Mice model and renal injury assessment

The workflow procedure is summarized in Figure 8. All animal procedures were reviewed and authorized by the Institutional Animal Care and Use Committee of the University of Bologna (Comitato per il benessere degli animali, CoBA) and received the approval by the Italian Ministry of Health (Ethics Approval Code n. 583/2022-PR, 3 October 2022). Experiments were performed following the standards of European Directive 2010/63/UE and Italian Law 26/2014. Female CD-1 mice (Mus musculus), 6–7 weeks old and weighing 21–26 g, were obtained from Charles River Laboratories and kept in the Department of Veterinary Medical Sciences' facilities at the University of Bologna. Mice were maintained in individually ventilated cages (1500 cm^2, 1500U Blu Line, Tecniplast S.p.A., Italy) with HEPA-filtered air providing 50 changes per hour. The housing environment was controlled for temperature (20-24 °C), relative humidity (45–65%), and a 12 h light/dark cycle. Mice had continuous access to food and water, were grouped 5–10 per cage, and enrichment items were provided to encourage normal behaviours.

Two different experimental models were conducted using CD-1 mice. In the first setting, animals were treated with intravenous injections of Stx2a (10 or 15 pg/g) diluted in PBS containing 1% BSA, either alone or combined with NAB815 (0.01 µg/mL). Control animals received equal volumes of PBS-BSA 1% or NAB815 alone. Each injection was administered via the tail vein in a volume of 100 µL. In the second experimental model, CD-1 mice received 300 µL of EV via tail vein injection. EV were isolated from human blood exposed to 2 nM Stx2a, Stx2a combined with NAB815 (0.01 µg/mL), NAB815 alone (0.01 µg/mL), or vehicle as control. The Stx2a dose delivered through EV from toxin-treated blood

corresponded to 5 ID_{50} (as measured by Vero cell viability assay), equivalent to 15 pg/g. EV isolated under the other experimental conditions were administered at equal volumes for comparison. All solutions (free toxin) and suspensions (EV-associated toxin), corresponding to the first and second models, were kept on ice for up to 1 hour and allowed to reach room temperature immediately before administration. Serum was obtained from blood collected in Eppendorf tubes via retromandibular bleeding. After allowing the blood to clot at room temperature for 30 minutes, samples were centrifuged at 4000 × g for 10 minutes to obtain serum. The serum was then aliquoted and stored at −20 °C. Serum samples were analyzed for urea and creatinine concentrations using commercial assay kits (Urea Assay Kit ab83362; Creatinine Assay Kit ab65340, Abcam) according to the manufacturer's instructions. Mice were weighed daily and monitored for health status, morbidity, and survival for 10 days after injection.

Histopathology

Histopathological analyses were conducted on mice that either died (first experimental model) or were sacrificed at the end of the experiments. Animals were euthanized using an isoflurane overdose (Iso–Vet, Piramal Critical Care, Voorschoten, The Netherlands) and immediately subjected to cervical dislocation. Kidneys were fixed in 10% neutral formaldehyde for 48 h to preserve them, and tissue sections were stained with hematoxylin and eosin, and periodic acid–Schiff (PAS) to highlight proximal tubules, recognizable for their thick brush border. A veterinary pathologist (Dipl. ECVP), blinded to group allocation, performed all slide evaluations. Acute tubular injury (ATI) was defined as tubular epithelial attenuation with loss of brush border, apical cytoplasmic blebbing with increased eosinophilic staining, nuclear alterations such as chromatin condensation, increased basophilia, or indistinct nuclear borders, lumens containing sloughed necrotic cells, fibrin deposits or hyaline casts, and hydropic degeneration. Kidney sections stained with PAS were examined under a light microscope at 4× magnification to assess ATIs, which were scored based on the proportion of affected parenchyma: 0 (minimal, <10%), 1 (mild, 11–25%), 2 (moderate, 26–50%), 3 (marked, 51–75%), and 4 (severe, >75%). Regions with extensive damage were further evaluated by counting detached cells within a 1 cm^2 area using a 10 × 10 mm grid at 400× magnification (total area 1 mm^2). The evaluation was repeated in smaller sections (0.1875 mm^2) to count all ATI-associated cells.

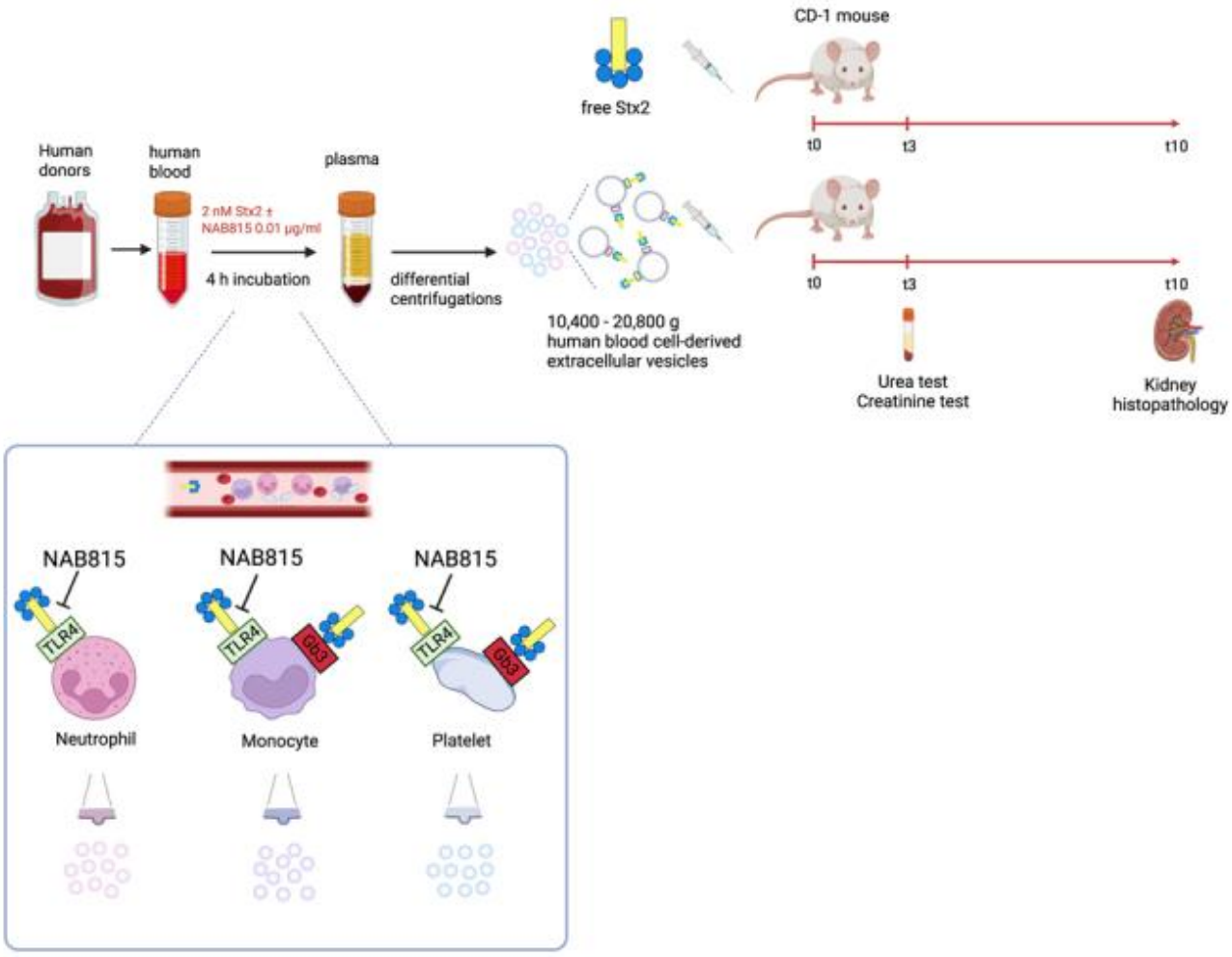

Figure 8.

Schematic representation of the workflow adopted to evaluate the impact of NAB815 treatment in mice challenged with either soluble Stx2a or blood cell-derived EV carrying Stx2a.

Construction of engineered STEC strains

During my visiting PhD studies at the Hygiene Institute of Münster University (Uniklinikum Münster, Germany), we investigated the effects of NAB815 and polymyxin B on SOS response activation and consequent Stx production using engineered and clinical STEC isolates. To evaluate whether these antibiotics could trigger phage induction, two non-virulent *E. coli* strains producing either Stx1 or Stx2 were used. The first strain, *STEC* O157:H7 EDL933 *Δstx2 stx1::yfp* pMBM25, kindly provided by Dr. Michael Berger, was constructed as previously described [72]. In this strain, the *stx1* gene was precisely replaced with a yellow fluorescent protein (yfp) reporter in a derivative lacking *stx2*, allowing

accurate measurement of Stx1 production. To enable simultaneous monitoring of SOS response induction, a low-copy-number plasmid carrying a *recA promoter–cyan fluorescent protein* (*recAP*::*cfp*) transcriptional fusion was introduced. This plasmid also conferred resistance to kanamycin, permitting selection of successfully transformed cells while allowing simultaneous tracking of SOS activation. In contrast, the second strain, *STEC* O104:H4 *stx2::yfp* pKB1 *recAP::cfp*, was engineered *de novo* for this study. The parental *STEC* O104:H4 *stx2::yfp* strain was transformed with plasmid pKB1, which carries a *recAP::cfp* fusion gene along with a hygromycin resistance cassette for selection. Plasmid pKB1 was constructed by cloning the *recA promoter–cfp fusion* (*recAP::cfp*) into a low-copy-number vector containing the pSC101 replication operon, which maintains a stable copy number under UV irradiation and therefore does not interfere with the SOS response. This engineered strain enabled simultaneous monitoring of SOS response induction (via cfp) and Stx2 production (via yfp) in a time-resolved manner through quantitative reporter gene expression.

Growth conditions and reporter gene expression measurements

The engineered strains *STEC O157:H7 EDL933 Δstx2 stx1::yfp pMBM25* and *STEC O104:H4 stx2::yfp pKB1 recAP::cfp* were initially cultured on LB agar supplemented with either kanamycin or hygromycin (both at 12.5 µg/mL) and incubated overnight at 37 °C. Single colonies were then inoculated into 2 mL of minimal growth M9 medium containing 0.4% glucose, 0.4% casamino acids, and the appropriate selective antibiotic, and grown overnight at 37 °C with shaking at 180 rpm. Overnight cultures were diluted 1:10 into standard M9 medium (150 µL per well) without the test antibiotics in black 96-well plates with transparent bottoms and lids. Plates were incubated at 37 °C in a Tecan Infinite 200Pro microplate reader. Each measurement cycle consisted of linear shaking at 1 mm amplitude for 5 seconds, followed by automatic recording of optical density (OD) at 595 nm, CFP fluorescence (excitation 442 nm / gain 85), and YFP fluorescence (excitation 514 nm / emission 550 nm / gain 100), followed by linear shaking at 2 mm amplitude for 450 seconds. After 60 minutes, the test antibiotic (1.5 µL of differently concentrated solutions of NAB815 or polymyxin B in PBS) was added to reach the final concentrations reported in the Results section. Ciprofloxacin and PBS were included as positive and negative controls, respectively. Samples were monitored for a total of 20 hours (1200 minutes) and protein

production was quantified as the increase in fluorescence (F [A.U.]) according to the method described by Berger et al [72]. At the end of the 20-hour experiment, 5 µL of each sample was analyzed using a Leica M205 FCA fluorescence microscope to visually assess the effects of antibiotic exposure.

Collection and concentration of supernatants from clinical *E. coli* isolates exposed to NAB815 and polymyxin B

To assess whether NAB815 or polymyxin B exposure increases the production of functional Stx in clinical *E. coli* isolates producing Stx1 (strain 2074/97) or Stx2 (strain 03-06016) additional studies were performed at the Uniklinikum Münster. The strains were treated with NAB815 or polymyxin B at concentrations of 0.01 and 0.1 µg/mL, while ciprofloxacin (0.1 µg/mL) and PBS served as positive and negative controls, respectively.

A four consecutive days workflow allowed the collection of antibiotic-exposed concentrated supernatants. Frozen strains (–70 °C) were streaked onto blood agar and incubated overnight at 37 °C to obtain isolated colonies. Single colonies were then used to establish five overnight cultures in 3 mL LB medium within 15 mL Falcon tubes with vented caps, incubated at 37 °C with shaking at 180 rpm. On the third day, 3 replicate subcultures per experimental condition were prepared by inoculating 10 µL of the overnight cultures into 10 mL of LB medium in 50 mL Falcon tubes. Following a 3-hour pre-incubation at 37 °C with shaking at 180 rpm, the different compounds were added at their predetermined final concentrations and incubated for 20 hours under the same conditions. During the last experimental day, bacterial growth was assessed by measuring the optical density of cultures diluted 1:10 in LB medium and cultures were then centrifuged at 2200 × g for 5 minutes to collect supernatants for Stx detection. Supernatants were transferred to 10 mL syringes and sterilized by filtration through 0.2 µm filters. Sterility was confirmed by plating filtered samples onto blood agar and incubating for 48 hours, while remaining supernatants were temporarily stored at 4 °C. Finally, the supernatants were concentrated using Sartorius Vivaspin™ Turbo 15 devices (MWCO 5,000 Da, GE Healthcare) by centrifugation at 3000 × g until a final volume of 300 µL was reached. The concentrated supernatants were used to assess the levels of functional Stx produced in response to drug exposure, using both Western blotting and cytotoxicity assays.

Western blot analysis of concentrated supernatants from clinical isolates treated with NAB815 and polymyxin B

Concentrated samples (12 µL) were mixed with 3 µL of 1× Laemmli buffer containing 5% β-mercaptoethanol (Bio-Rad) and boiled at 99 °C for 10 minutes. Proteins were separated by SDS-PAGE using pre-cast Mini-PROTEAN TGX AnyKD gels (4–20%, 15 wells; Bio-Rad) and run at 200 V for 30 minutes. For transfer, polyvinylidene fluoride (PVDF) membranes were activated in 100% ethanol for 2–3 minutes and equilibrated in transfer buffer containing 20% methanol (v/v). Whatman paper sheets were soaked in the same buffer and used to assemble the transfer sandwich. Protein transfer was performed using the Trans-Blot® Turbo™ RTA Mini PVDF Transfer Kit (Bio-Rad) at 1.3 A and 19 V for 7 minutes. Blots were blocked in 5% skim milk in Tris-buffered saline-Tween-20 (TBS-T; 0.05%) for 1 hour at room temperature or overnight at 4 °C, followed by three washes (5 minutes each) with TBS-T. Primary antibody incubation using Ab anti-Stx1 or anti-Stx2, (1:68; Davids Biotechnologie, Regensburg, Germany) was carried out in TBS-T containing 0.01% sodium azide for 90 minutes at room temperature with shaking. Blots were then washed for 5, 10, and 15 minutes with TBS-T. Secondary antibody incubation (1:3000) was performed in TBS-T for 1–2 hours at room temperature with shaking, followed by additional washes as described above. Blots were equilibrated in 1× NBT/BCIP buffer (Roche) for 2–3 minutes and developed in NBT/BCIP solution (Roche) (1:500) for approximately 15 minutes in the dark. Finally, membranes were rinsed with double-distilled water and left to dry overnight. Images were acquired using a ChemiDoc MP system (Bio-Rad) and analyzed with the Lane and Bands Analysis Tool in Image Lab software version 4.0.1 (Bio-Rad).

Cytotoxicity studies on Vero cells using supernatants from clinical isolates treated with NAB815 and polymyxin B

This protocol was performed at Münster University and is a crystal violet-based cell viability assay, which differed from the viability assay described above. Vero cells, (passage 20) were seeded from a T75 flask at 95% confluence into two 96-well plates at a density of 4.0×10^4 in Eagle's Minimum Essential Medium (EMEM) supplemented with 10% fetal bovine serum. Plates were incubated overnight at 37 °C in a 5% CO_2 atmosphere to allow cell attachment. The following day, dilutions of the previously concentrated supernatants

were added to plated cells to achieve a final concentration of 0.02× (1:50 dilution). Plates were incubated for 72 hours at 37 °C with 5% CO_2. Following incubation, cells were fixed with 2% formaldehyde solution for 2 minutes at room temperature, then stained with 0.0652% crystal violet solution for 1 hour. Unbound dye was removed by washing three times with deionized water, and plates were air-dried overnight at 37 °C. For quantification of cell viability, crystal violet was solubilized by adding 100 µL of 50% ethanol to each well, followed by gentle shaking for 1 hour at room temperature. Optical density was measured at 570 nm using a microplate reader. Absorbance values were normalized to untreated control wells, and cytotoxicity was expressed as percentage of cell viability.

Statistical analysis

Statistical evaluation of the data was carried out using GraphPad Prism 8 software. Details on the number of replicates or subjects (n), statistical tests and significance levels are provided in figure captions or legends. Differences between continuous variables (mean ± SD) were assessed using a t-test after confirming normality of the data, and correlations between variables were evaluated using Pearson's correlation coefficient. For two-group comparisons, significance was determined with either a two-tailed unpaired t-test or a two-tailed unpaired Mann-Whitney test, depending on data distribution. For comparisons involving more than two groups, one-way ANOVA followed by Tukey's, Dunnett's or Holm's multiple comparison test was applied. The log-rank (Mantel-Cox) test was used to evaluate differences in survival curves obtained in animal experiments. A p value < 0.05 was considered statistically significant.

Principal component analysis (PCA) was applied to analyze and distinguish patterns obtained in the SERS spectra to evaluate the discriminatory performance of the designed biosensor. PCA is a statistical method used to simplify complex datasets by reducing their dimensionality while keeping the main sources of variance. Specifically, PCA helped to discriminate among Stx1a, Stx2a, and cleaved Stx2a, whose SERS spectra displayed high similarity. Data analysis was conducted in R (version 2024.04.2+764) using the *ChemoSpec* package. Following PCA, a one-way analysis of variance (ANOVA) was applied separately to the first two principal components (PC1 and PC2) using the stats package in R.

Results

Stx1 blunts the pathogenic effects of Stx2 in blood

To investigate the pathogenic mechanisms underlying the well-known protective effects of Stx1 on the HUS-triggering effects of Stx2 in animal models, and to explain why patients infected with STEC strains co-producing Stx1 and Stx2 are at moderate risk of developing HUS, human blood from healthy donors was exposed to purified toxins. Blood samples were treated with 2 nM Stx2a, 1 nM Stx1a, or their combination to generate human blood cell-derived Stx-containing EV. An equivalent volume of PBS served as negative control. The selected toxin concentrations reflect conditions observed in STEC-infected patients, where similar serum Stx2 levels were observed during infections by STEC producing Stx2 alone or in combination with Stx1, while Stx1a, when present, is typically found at lower concentrations [24, 131].

Stx1a and Stx2a are similarly associated with large blood cell-derived EV

Whole blood from a representative donor was challenged with Stx1a or Stx2a or vehicle as described above, then large EV (10,400–20,800 × g) were purified by following the sequential centrifugation protocol described in the Method section. Subsequently, control-, Stx1a- and Stx2a-blood-derived EV were analyzed by size exclusion chromatography using qEV 70 nm columns (Izon Science, Cambridge, MA, USA). Aliquots of the obtained fractions were applied to Vero cells for cytotoxicity assessment through viability assay.

Unlike control EV fractions, which exhibited minimal cytotoxic effects characterized by a flat response profile (Figure 9), EV derived from Stx1a- or Stx2a-treated blood exhibited maximum toxicity in fraction 6 (Figure 9; green squares and red triangles, respectively). In accordance with the technical specifications provided by the manufacturer, qEV 70 nm columns typically separate unpurified plasma-derived EV into fractions 7–10 (blue rectangle, Figure 9). The earlier elution of toxin-associated EV in fraction 6 confirms that both Stx1a and Stx2a stimulated circulating cells to release large EV. This finding is consistent with previous reports showing that exposure to 2 nM Stx2a produces a large EV profile, as determined by similar chromatographic methods [177]. Cytotoxicity assays, while useful for detecting EV-associated toxin activity, cannot distinguish between the effects of Stx1a and Stx2a when both toxins are simultaneously present. Since both toxins induce

indistinguishable cytotoxic responses in Vero cells, alternative analytical approaches are required to assess their individual contributions in co-treatment conditions.

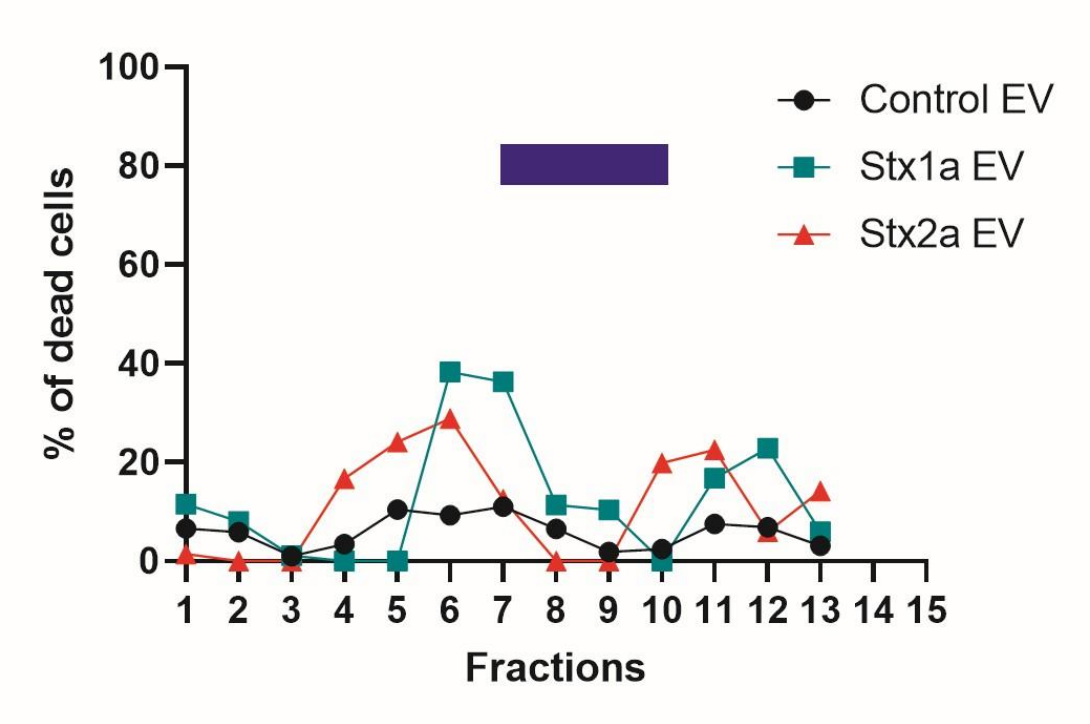

Figure 9.

Analytical gel-filtration of EV produced after treatment of human blood with Stx1a or Stx2a. Human blood samples (40 mL) from a representative donor were incubated for 4 h at 37 °C with Stx2a (2 nM) or Stx1a (1 nM) or PBS. Large EV were sedimented between 10,400 g and 20,800 g and 100 µl-aliquots of each preparation, brought to 500 µl with PBS, were applied to qEV original 70 nm columns and analysed by size exclusion chromatography as described in Materials and methods section. Aliquots of each 500 µl-fraction were added to cultured Vero cells which are sensitive to Stx action. Viability of cells was assessed by a luminometric assay as described in Material and methods section. Aliquots of each 500 µl-fraction were added to cultured Vero cells which are sensitive to Stx action. Viability of cells was assessed by a luminometric assay as described in Methods section. Data are expressed as percent of dead cells with respect to controls run with PBS; 1 nM Stx1a EV (green line), 2 nM Stx2a EV (red line), and control EV (black line). According to the column performance described by the manufacturer, the blue rectangle indicates the elution position of total non-purified EV present in human plasma samples (500 µl) loaded on the same column and analysed under the same conditions.

Characterization of EV released upon exposure to Stx1a, Stx2a, and their combination via NTA and WES

To characterize the EV populations obtained after Stx treatment, NTA was performed on vesicles purified from the blood of a representative donor. Treatment with Stx2a induced substantially higher vesicle production (8.5×10^{10} particles/mL; Figure 10A, red line) compared with Stx1a (3.3×10^{10} particles/mL; Figure 10A, green line) or control samples (3.7×10^{10} particles/mL; Figure 10A, black line). Size distribution analysis revealed that control samples contained predominantly small vesicles (50–350 nm), with negligible populations around 480 nm and 575 nm (Figures 10A and 10B, black line). Exposure to Stx1a produced a similar small-vesicle profile but also generated a distinct population centered at approximately 400 nm (Figure 10B, green line). Stx2a treatment resulted in a comparable generation of a large-vesicle peak around 425 nm (Figure 10B, red line) and markedly increased the abundance of smaller vesicle fractions (Figure 10A, red line). Notably, simultaneous exposure to both toxins clearly reduced the total EV population (2.1×10^{10} particles/mL; Figure 10A, blue line), with decreases across all size ranges, particularly in vesicles larger than 300 nm. Strikingly, the characteristic 400 nm peak observed in single-toxin treatments was completely absent following co-exposure (Figure 10B, blue line).

A clear-cut picture of the observed differences emerged when we calculated the total volume of the different vesicle populations according to their diameter (Figure 11A-D). In samples exposed to individual toxins, the 400 nm vesicle population accounted for approximately 20% (Stx1a) or 11% (Stx2a) of the total EV volume. Combined toxin exposure markedly reduced the overall EV population (Figure 11D), with the large-vesicle fraction decreasing to 4%. Although substantial donor-to-donor variability was observed in the response to individual toxins, particularly among vesicles smaller than 300 nm, the suppressive effect of combined toxin treatment on vesicle formation was remarkably consistent across all donors examined (Figure 11E).

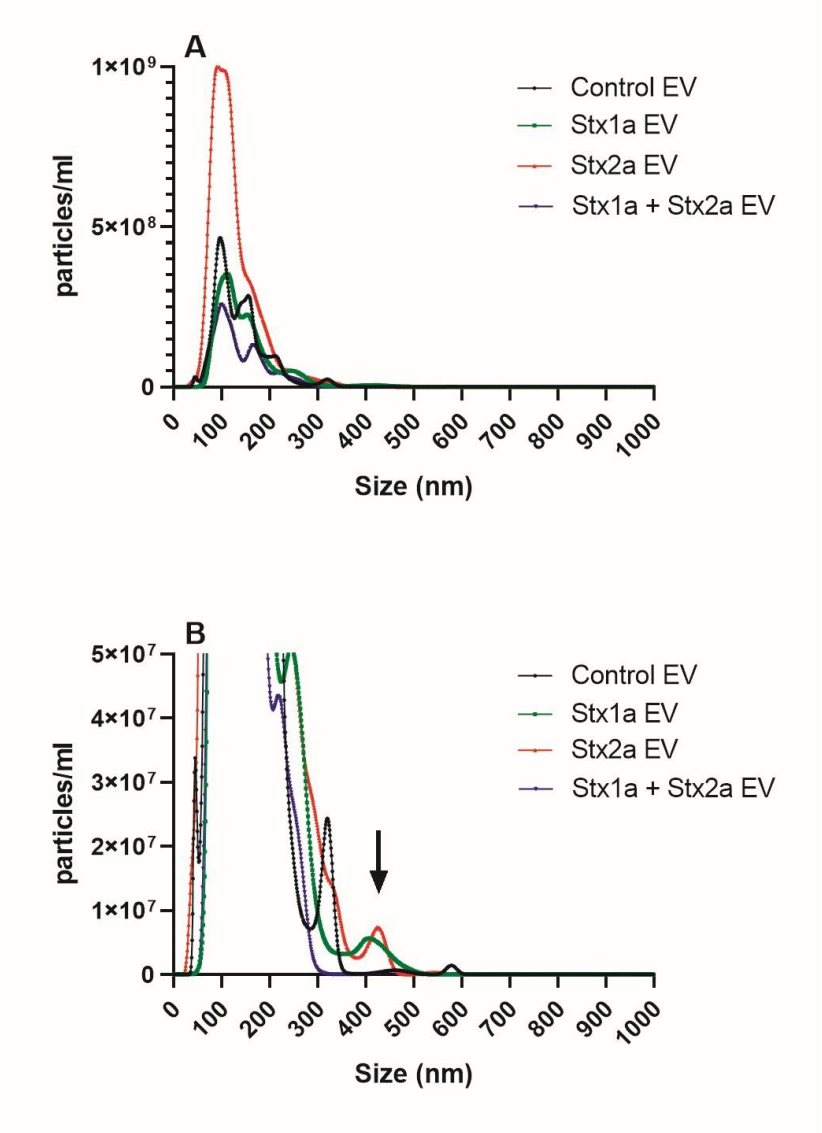

Figure 10.

(A-B) Number of blood cell-derived EV produced after treatment with Stx1a, Stx2a alone or in association. Human blood samples (40 mL) from a representative donor were incubated for 4 h at 37 °C with Stx2a (2 nM) or Stx1a (1 nM) or with both toxins (2 nM Stx2a+1 nM Stx1a). Large EV were sedimented between 10,400 g and 20,800 g as described in Materials and methods section and characterized by Nanoparticle tracking analysis. **(A)** Data are expressed as the number of particles/mL of the different EV populations resolved by the technique and differing each other in diameter by 0.5 nm; 1 nM Stx1a (green line), 2 nM Stx2a (red line), 1 nM Stx1a+2 nM Stx2a (blue line) and vehicle (black line). **(B)** The same data depicted in panel A are reported in this panel which differs only in the scale of the y-axis. The black arrow indicates the toxin-induced peaks featuring the larger EV components (~400 nm diameter).

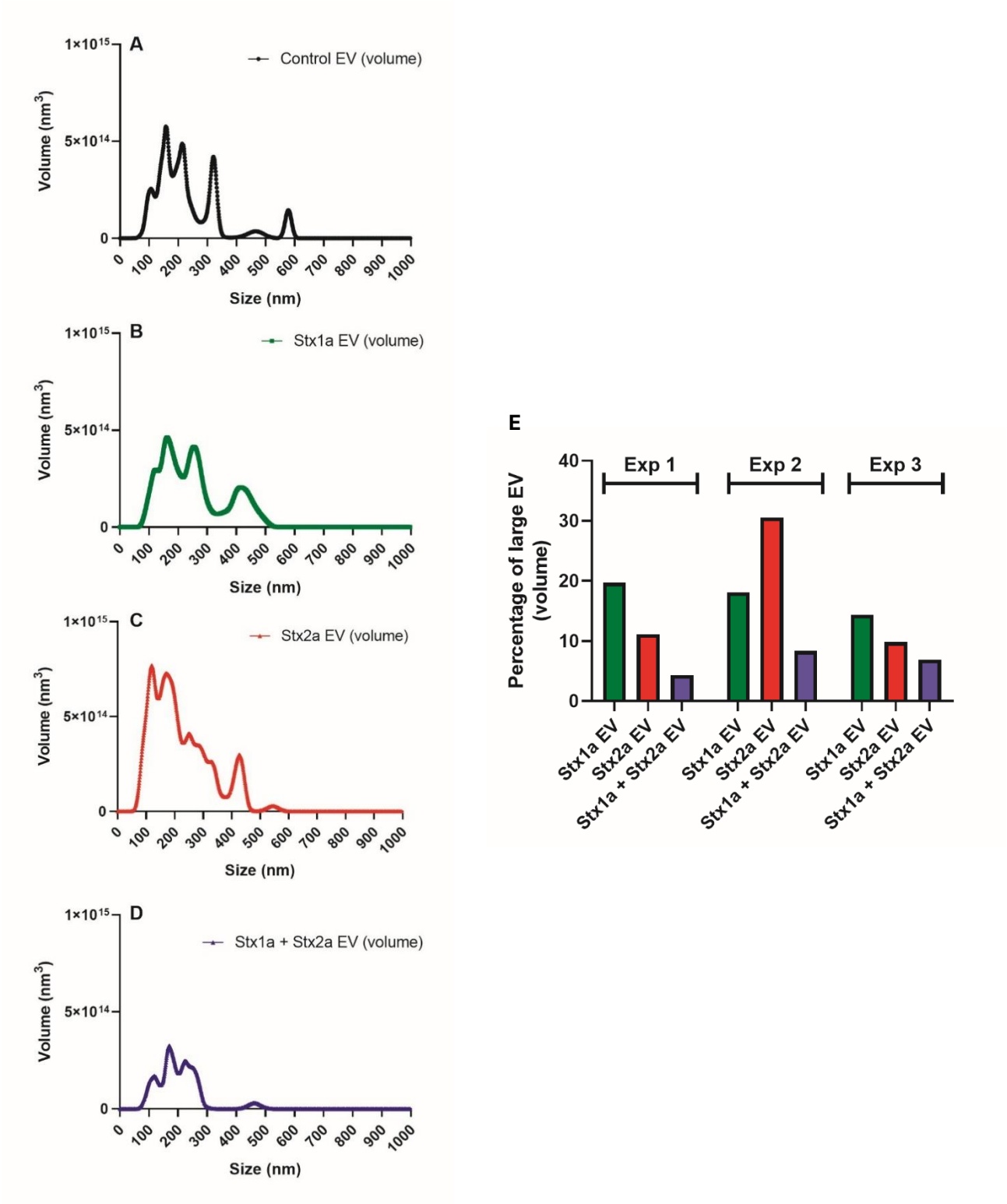

Figure 11.

(A–D) The same data reported in Figure 10 on the large EV released by human circulating cells from a representative donor after treatment with 1 nM Stx1a (green line), 2 nM Stx2a (red line), 1 nM Stx1a+2 nM Stx2a (blue line) and vehicle (black line) were expressed as total volume (nm^3) of each population of EV and was calculated according to their diameter assuming a spherical shape. **(E)** Percentage of large (>300 nm) blood cell-derived EV (volume) produced after treatment with Stx1a,

Stx2a alone or in association. Human blood samples (40 mL) from three donors were incubated for 4 h at 37 °C with Stx2a (2 nM) or Stx1a (1 nM) or with both toxins (2 nM Stx2a +1 nM Stx1a). Large EV were sedimented between 10,400 g and 20,800 g, as described in Materials and methods section, and characterized by Nanoparticle tracking analysis. Data are expressed as percentage of the volume of large (>300 nm) EV relative to total EV volume calculated with three different donors, 1 nM Stx1a (green bars), 2 nM Stx2a (red bars), 1 nM Stx1a+2 nM Stx2a (blue bars). Stx levels are shown as absolute EV volumes, without normalization, to preserve the effects of individual and combined toxin exposures

WES analysis of the proteins extracted from the EV from three independent donors revealed considerable inter-donor variability in toxin-induced responses, as indicated by the expression of the vesicular marker Alix (see SDs in Figure 12C). Despite donor-dependent variability, exposure to either Stx1a or Stx2a enhanced Alix expression, whereas co-exposure to both toxins elicited a weaker response than single treatments (Figures 12A and 12C). The slight non-significant reduction in total Alix expression recorded in the latter condition (Figure 12C) reflects the constant inhibition of the larger EV peaks which constitute 10–30% of the total EV population (Figure 11E). No additive effects were observed, as Alix levels in co-treated samples were lower than the expected sum of the individual toxin responses (Figure 12C, dashed bar). Overall, the findings about the vesicular marker Alix support the data obtained from the NTA analysis (Figure 11A-D).

Consistent with previous observations [177], EV obtained after toxin exposure were positive for the leukocyte marker CD45 and for the platelet antigen CD42a (Figure 13). The expression patterns of CD42a followed those of Alix, displaying a modest, non-significant reduction after combined treatment and no additive effects. CD45 expression remained comparable across treatments, with a significant increase observed only after Stx2a exposure relative to controls. It is worth noting that Stx2a levels in EV were significantly lower following combined Stx1a + Stx2a treatment compared with Stx2a alone (Figures 12B and 7D). The specificity of the anti-Stx2 antibody in recognizing Stx2a by WES, even in the presence of Stx1a, was assessed experimentally. Stx1a (1.5 and 3 ng), Stx2a (1.5 and 3 ng) and a combination of the two toxins (3 ng Stx2a+1.5 ng Stx1a) were added to proteins extracted from a HeLa cell lysate and WES analysis was performed (Figure 12B). WES analysis confirmed that the anti-Stx2 antibody specifically recognized Stx2a and that the presence of Stx1a did not affect its quantitative detection (Figure 12B). In conclusion, Stx1a reduces the production, size, and Stx2a content of EV induced by Stx2a after treatment of

human circulating cells. Since Stx2a is more dangerous than Stx1a for STEC-infected patients, the observations herein described might explain the lower incidence of HUS in patients in patients infected with STEC strains expressing both toxins.

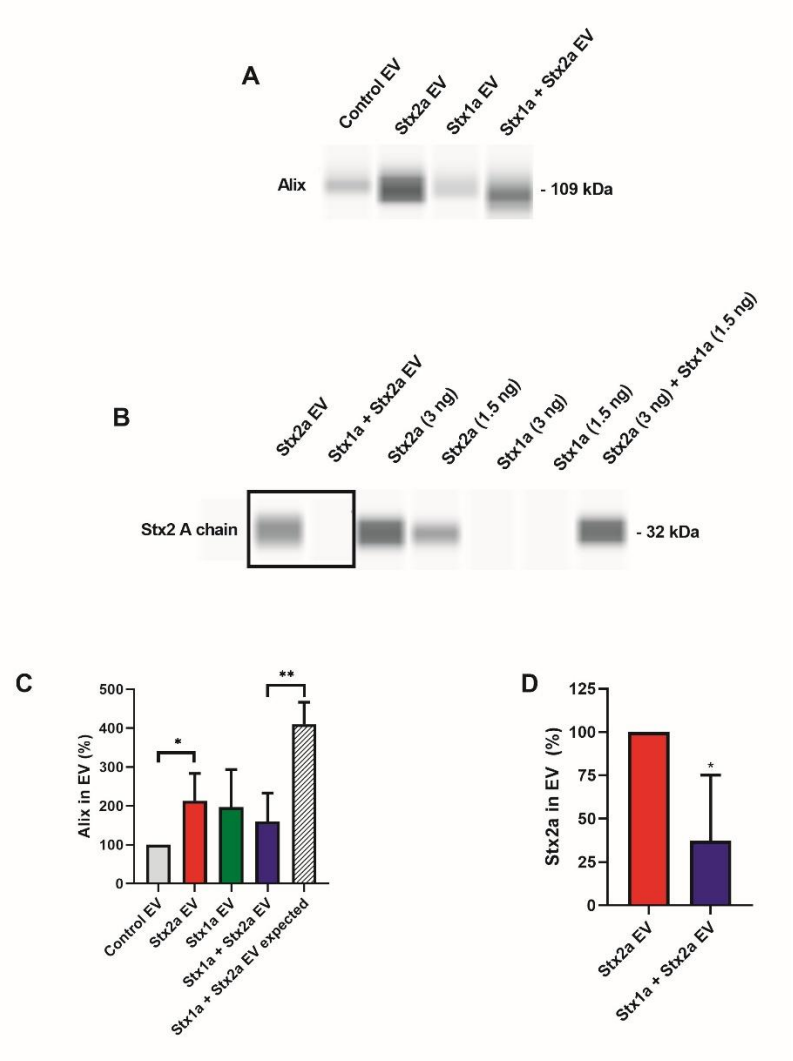

Figure 12.

(A-D) Stx1a reduced the release of blood cell-derived EV containing Stx2. **(A)** WES analysis of the EV marker Alix derived from human EV isolated from a representative donor. **(B)** Quantitative WES analysis of the Stx2a associated to human EV, and ability of the rabbit anti-Stx2 antibody to recognize Stx2a even in the presence of Stx1a. Box: A contrast modification was applied to the lanes with EV-extracted proteins since the amount of Stx2a in these samples was lower (<1.5 ng) than those of the lanes with added Stx. **(C)** Data are expressed as mean ± SD (n = 3) of the percentage of Alix determinations with respect to control obtained by analysing the EV isolated from 3 different donors. The expression of Alix in Stx1a+Stx2ainduced EV was also compared to the sum of the values obtained in Stx1a-induced EV and Stx2a-induced EV. **(D)** Data are expressed as mean ± SD (n = 3) of the percentage of Stx2a determinations in Stx1a+Stx2ainduced EV relative to Stx2a amounts found in Stx2a-induced EV from three different donors. * $p < 0.05$: ** $p < 0.01$

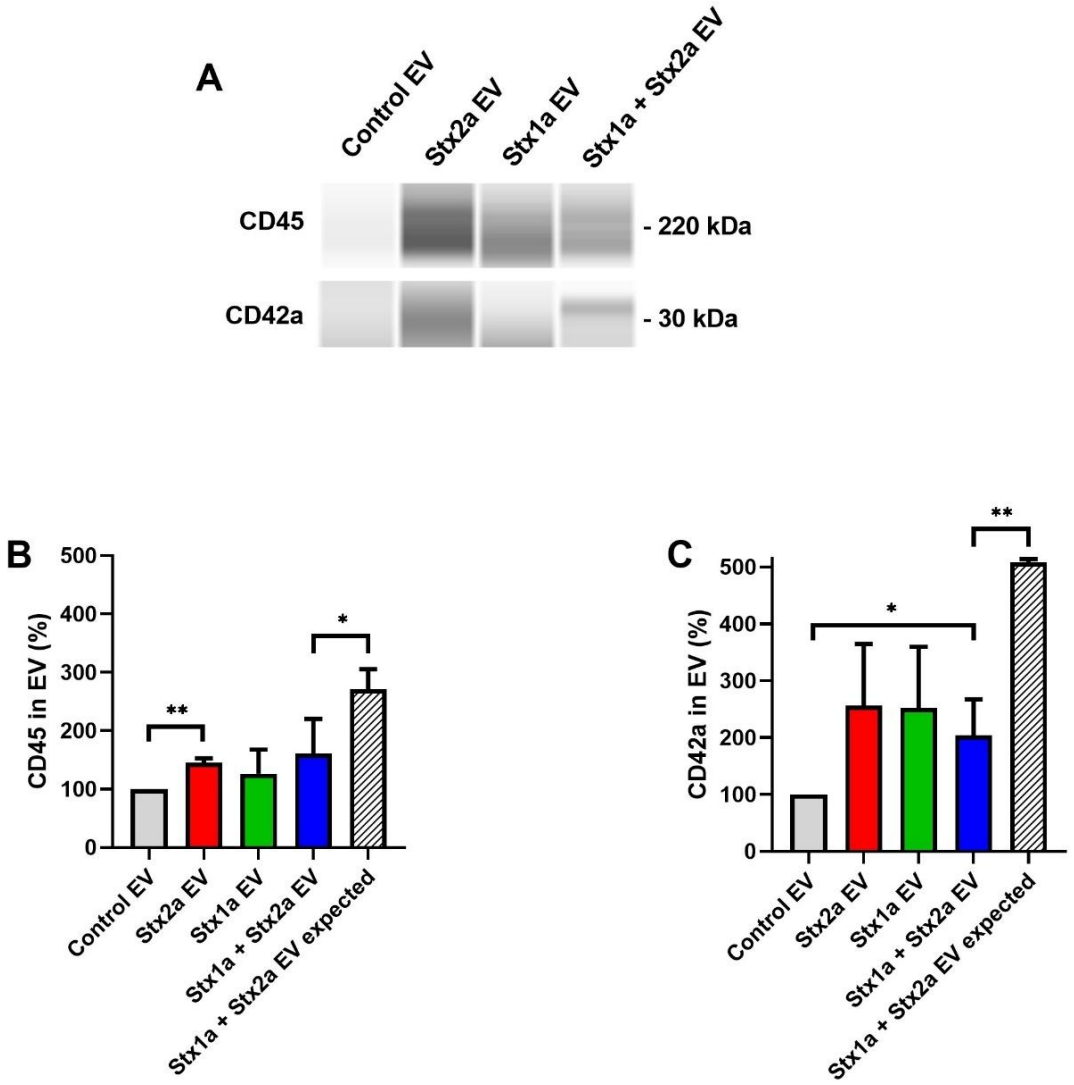

Figure 13.

(A-C) Cellular origin of the EV produced by human blood cells challenged with Stx. (A) WES analysis of the leukocyte marker CD45 or of the platelet marker CD42a derived from human EV isolated from a representative donor. **(B)** Data are expressed as mean ± SD (n = 3) of the percentage of CD45 determinations with respect to control obtained by analysing the EV isolated from 3 different donors. The expression of CD45 in Stx1a+Stx2a-induced EV was also compared to the sum of the values obtained in Stx1a-induced EV and Stx2a-induced EV. **(C)** Data are expressed as mean ± SD (n = 3) of the percentage of CD42a determinations with respect to control obtained by analysing the EV isolated from 3 different donors. The expression of CD42a in Stx1a+Stx2a-induced EV was also compared to the sum of the values obtained in Stx1a-induced EV and Stx2a-induced EV. * $p <$ 0.05: ** $p < 0.01$

Design of plasmonic surfaces for the specific recognition of Stx2a, cleaved Stx2a, and Stx1a

The diagnosis of STEC infections is based on clinical presentation associated with laboratory and microbiological assays tests. The latter methods are often time-consuming and may lack the sensitivity required for early detection. Point-of-care diagnostic tools can provide immediate results allowing timely administration of appropriate therapies. As previously demonstrated [176], sensors based on plasmonic effects may be suitable for rapid and sensitive detection of Stx, the main pathogenic factors responsible for HUS development.

To establish spectral signatures for different toxin types and forms, Stx1a, Stx2a, and Stx2a-cl were applied at 45 nM concentration onto nanofabricated SERS substrates via direct adsorption. Figure 14A presents the normalized average spectra for Stx1a (blue line), Stx2a (red line), and Stx2a-cl (green line), with principal vibrational assignments summarized in Table 2. The Raman analysis showed unique peaks for the different toxins highlighting their chemical fingerprints. Careful analysis of the spectra revealed notable differences in peak shifts and intensities among the different toxins. The spectral profiles showed characteristic peaks, including those related to disulfide bond stretching, aromatic amino acid residues, and backbone stretching, reflecting the molecular structure of each of the assayed Stx. Proteolytic cleavage of Stx2a A chain originating Stx2a-cl resulted in a distinctive spectral pattern. The cleaved form exhibited unique Raman peaks at 671, 731, 891, and 1,552 cm^{-1}, along with enhanced thiol group exposures at 2,510 and 2,524 cm^{-1}, indicating substantial structural reorganization. Within the C–S stretching region, the Stx2a-cl spectrum showed a dominating peak at 671 cm^{-1} (C-S bond vibration) absent in Stx1a and intact Stx2a spectra which exhibited a better resolved methionine peak at 720 cm^{-1}. Cleavage also resolved new tryptophan-related peaks (731, 891, 1,552 cm^{-1}), suggesting increased exposure of these aromatic residues compared with intact Stx2a. Several peaks present in native Stx2a were absent in Stx2a-cl, providing additional evidence of structural modification induced by cleavage. The two yellow boxes in Figure 14A highlight additional spectral differences between cleaved and the wild type toxins. In the bands between 550–750 cm^{-1} and 1,125–1,370 cm^{-1}, peaks appeared sharper or more resolved. Notably, the vibration of the Amide III region at 1,279 cm^{-1} characteristic of α-helical conformation exhibited marked intensification in Stx2a-cl. This is consistent with results obtained with intact Stx2a showing a significant α-helix structure by circular dichroism [97]. Quantitative assessment revealed

systematic intensity variations across the spectral profiles. Disulfide bond vibrations at 514 and 544 cm^{-1} exhibited 1.3- and 1.1-fold increase in the area under the curve in Stx2a-cl relative to the native form. Moreover, the -SH bands demonstrated a spectral shift, appearing at 2,510 cm^{-1} in the cleaved variant versus 2,524 and 2,535 cm^{-1} in the intact toxin, with corresponding 1.5-fold area increase. These quantitative alterations provide additional evidence of cleavage-induced structural changes. When comparing Stx1a and Stx2a, a substantial spectral divergence was evident, consistent with their independent genetic origins and different primary structures. The differences in the spectra of the native toxins (Stx1a and Stx2a) are more quantitative than qualitative, as toxins shared most of the peaks that, however, showed different intensities.

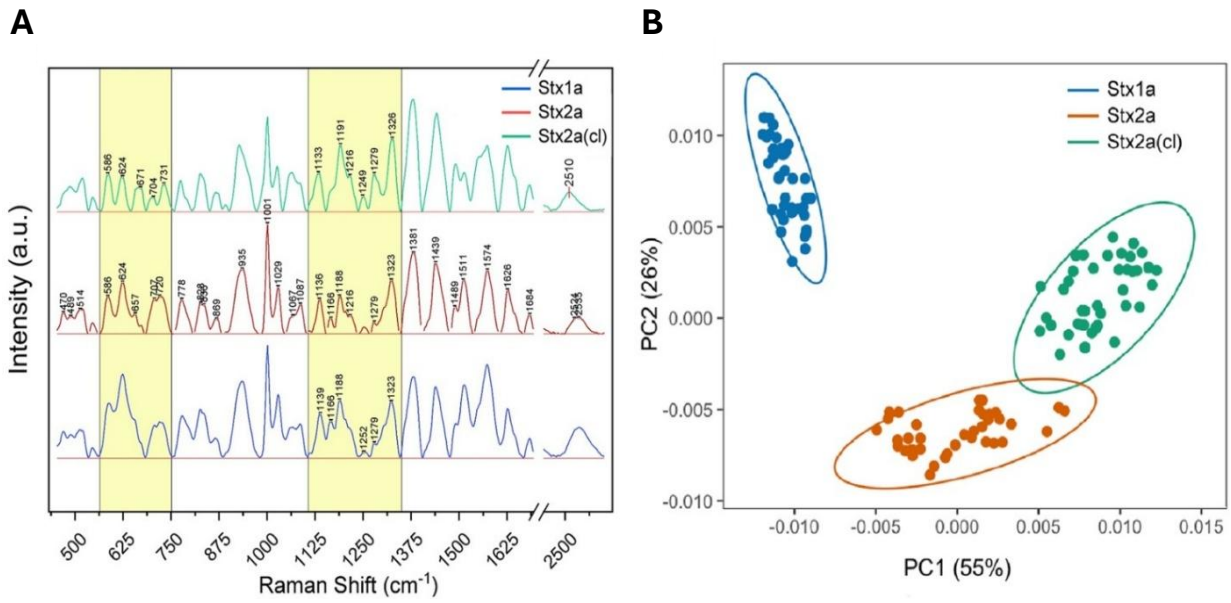

Figure 14.

(A-B) SERS coupled with PCA analysis of Stx variants. **(A)** SERS fingerprints of Stx1a (blue), Stx2a (red), and Stx2a-cl (green). **(B)** PCA of SERS measurements for Stx1a (blue points), Stx2a (red points), and Stx2a-cl (green points).

To extract key discriminating spectral information from the small differences observed in the complex spectral SERS datasets, the statistical method PCA was used. Figure 14B shows the projected spots in the 2D space constructed by the first two principal components (PC1 and PC2), revealing three spatially distinct populations corresponding to Stx1a (blue points), Stx2a (red points), and Stx2a-cl (green points). The points associated with the toxins form three clearly separated clusters, confirming successful

spectral discrimination. The relative distances between the clusters mirrored the real differences in chemical composition that are marked between Stx1a and Stx2a and very subtle between Stx2a and Stx2a-cl. One-way ANOVA confirmed statistically robust differentiation among the three toxins for both principal components ($p < 2\times10^{-16}$), indicating strong discrimination power. Collectively, these data establish SERS spectroscopy integrated with PCA as an effective label-free methodology for Stx identification in water. The combined contribution of PC1 and PC2 (55% and 26% variance, respectively; 81% cumulative) exceeded the 80% threshold for robust classification, enabling antibody-independent toxin discrimination (Figure 14B).

Wavenumber (cm^{-1})	Assignation	Stx1a	Stx2a	Stx2a(cl)
514–544	S–S stretching	+	+	+
624	n(C–S)G Phe	+	+	+
657	C–H in-plane bending, stretch of H39 on C16, strong swagging of H42 on C24 and H28 on N2, H37 on O12, out of plane breathing of benzene ring	-	+	-
671	Isoleucine/C–S stretching	-	-	+
720	Ile [78] met C–S stretching n(C–S)T Tryptophan	+	+	-
836	Backbone stretching/out of plane ring breathing in tyrosine	-	+	-
935	Tryptophan/ C–C stretching δ(C–C–N)symm, α-helical skeletal			
1,001	Symmetric ring breathing mode of phenylalanine Symmetric CC ring stretching	+	+	+
1,029	C–H stretching mode of phenylalanine	+	+	+
1,252	Amide III band -N–H in-plane bend, C–N stretch	+	+	+
1,279	Amide III band CH2 wag or Ring stretching	+	+	+
1,323	Trp/C–H deformation/backbone/C–N twisting C–H stretching of adenine	+	+	+
1,381	COO- stretching	+	+	+
1,552	COO^- stretching /His/ Trp /Phe	-	-	+
1,574	Amide II band - Ade/Gua			
1,626	Tyr/Trp/Phe	+	+	+
1,684	Amide I band	+	+	+
1,723–1,836	C=O stretch and C–C stretch	+	-	-
2,510–2,535	S–H stretching, thiol group exposure	-	-	+

Table 2.

Comparison and proposed assignment of the key SERS spectral peaks for the three Stx analyzed.

A second approach using functionalized SERS substrates was explored to develop a sensor capable of detecting and discriminating Stx1a, Stx2a, and Stx2a-cl in complex samples. Three copies of the nanostructured substrate were functionalized with specific antibodies for Stx1a (AbStx1a), Stx2a, or Stx2a-cl (AbStx2a) at 10 µg/mL in PBS. Each substrate was then incubated with the corresponding toxin. Figure 15A provides a schematic overview of the functionalization process. Repeated measurements were performed on each substrate before and after toxin deposition. Average SERS spectra are shown in Figure 15B for AbStx1a (black) and AbStx1a/Stx1a (blue), and in Figure 15C for AbStx2a (black),

AbStx2a/Stx2a (red), and AbStx2a/Stx2a-cl (green). Comparison of the spectra obtained with the antibody and with the Ab–toxin complex reveals notable differences, indicating structural changes in toxin spectrum upon antibody binding. For example, a new peak was observed at 500–550 cm^{-1} (Figure 15B) corresponding to disulfide (S–S) bonds characteristic of the toxin. The 1,574 cm^{-1} band, also evident in the fingerprint region, corresponds to amide II vibrations and reflects conformational changes in protein secondary structure upon binding. Similar distinctive spectral features were observed in complexes involving Stx2a and Stx2a-cl and AbStx2a. Specific peaks in the 1,500–1,700 cm^{-1} range (e.g., 1,574 cm^{-1} for the toxin, 1,500 cm^{-1} for the complex) further highlight structural differences induced by binding.

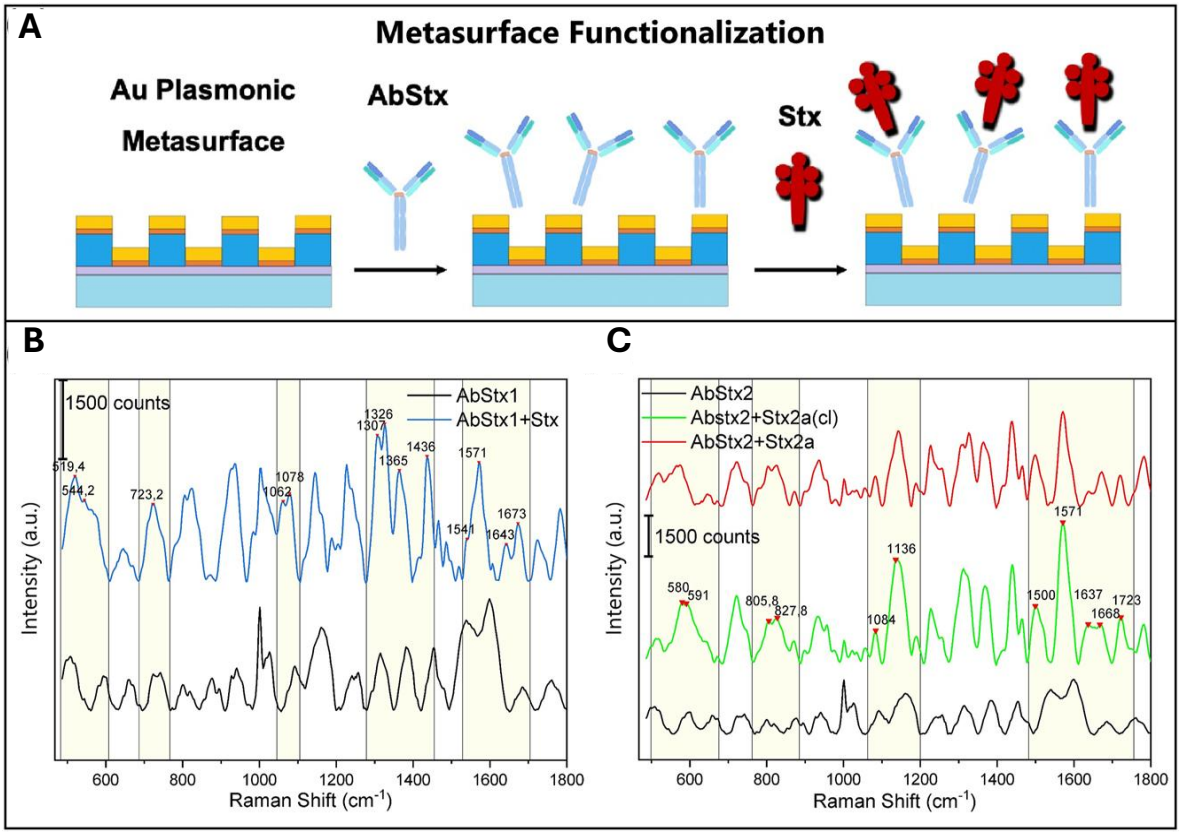

Figure 15.

(A-C) Analysis of functionalized SERS metasurface. **(A)** Scheme of the main steps of functionalization process. **(B)** Comparison of the average SERS spectra measured for AbStx1a (black line) at a concentration of 10 µg/mL and AbStx1a/Stx1a (blue line). **(C)** Comparison of the average spectra measured for AbStx2a (black line) at a concentration of 10 µg/mL in PBS, AbStx2a/Stx2a (red line) and AbStx2a/Stx2a-cl (green line) at 154 nM in PBS. Modified from [170].

To allow discrimination of the subtle differences of SERS signals, PCA was applied as described above. Figure 16 shows the resulting clusters in the 2D space referring to PC1 and PC2 of the SERS measurements for AbStx1a/Stx1a (blue), AbStx2a/Stx2a (red), and AbStx2a/Stx2a-cl (green), forming three distinct groups consistent with their chemical differences. The sum of the variance values for PC1 (48 %) and PC2 (34 %) exceed 80% also under this experimental condition, providing effective differentiation. ANOVA confirmed significant discrimination among the three toxins for both components ($p < 2\times10^{-16}$). While clear separation of the clusters was expected for Stx1a versus the two Stx2a variants due to the different and specific antibodies used in the assay, distinguishing Stx2a from Stx2a-cl was less obvious as the same antibody was used. These results demonstrate that PCA complements spectral analysis, enabling discrimination even between subspecies of toxins which are very similar.

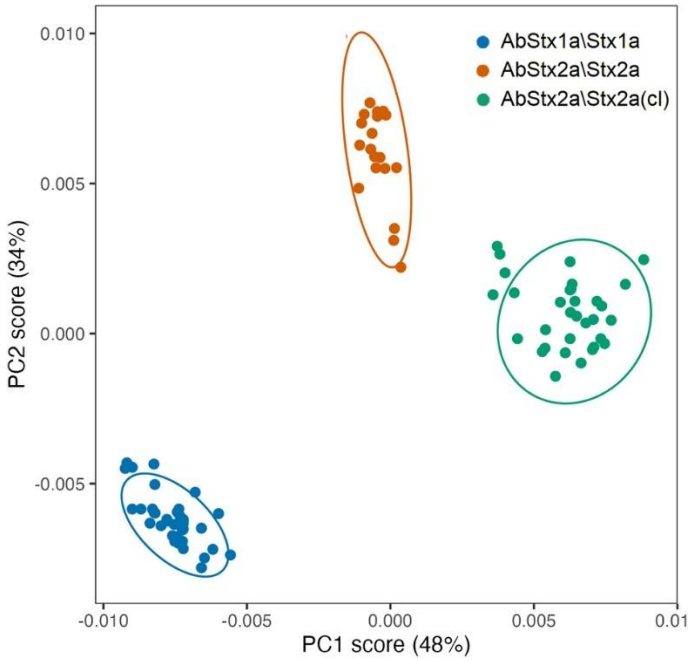

Figure 16.

PCA of SERS spectra for AbStx1a/Stx1a (blue points), AbStx2a/Stx2a (red points), and AbStx2a/Stx2a-cl (green points).

The sensor detection potential was further evaluated by determining the limit of detection (LoD) for Stx1a and Stx2a. SERS spectra were collected in PBS at sub-nanomolar concentrations using two plasmonic metasurfaces functionalized with 10 µg/mL of the corresponding antibodies. The sensor achieved LoDs of 6.8 pM (0.46 ng/mL) for Stx1a and 2 pM (0.14 ng/mL) for Stx2a, demonstrating sensitivity comparable to or exceeding that of other plasmonic and traditional detection methods (Figure 17; Table 3) [170].

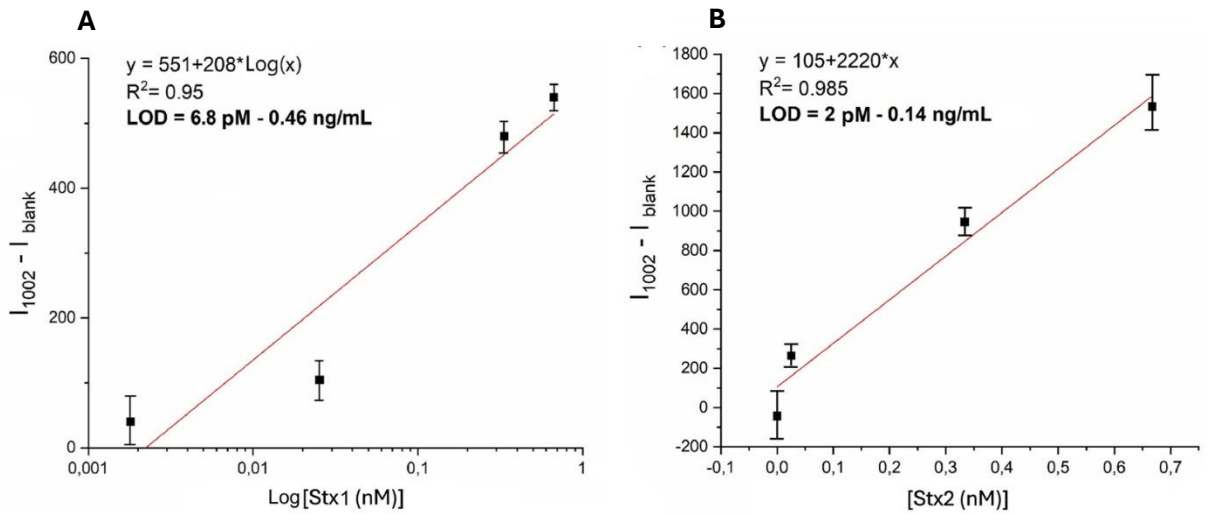

Figure 17.

(A-B) Determination of LoD of functionalized SERS metasurfaces. **(A)** LoD assessment for Stx1 detection. Experimental points derived from the 1,002 cm^{-1} peak intensity, corresponding linear fit (red line). **(B)** LoD assessment for Stx2 detection. Experimental points derived from the 1,002 cm^{-1} peak intensity, corresponding linear fit (red line). Modified from [170].

Technique	Feature	Analyte	LOD
LSPR platform	Synthetic glycosyl ceramides attached to gold nanoparticles	Stx	10 ng/mL
LSPR platform	Gold nanoparticles bound to antibodies	Stx2	10 ng/mL
SPC-ECL	Nanospheres of Au NPs encapsulated into a solid silica core with graphite phase carbon nitride quantum dots embedded	Stx	9 fM
SPRi	Biochip with 50-nm gold film	Stx1, Stx2	50 ng/mL
SERS substrate	Recycled silicon chips	Stx2	0.3158 µM
SERS device	Noble metal nanoparticles and Raman reporter loaded metal–organic framework	Stx2	0.82 ng/mL
LC-MS	Nanospray liquid chromatography-mass spectrometry and Vero cell bioassay	Stx	Stx2c (5.7 ng/mL)
Reverse latex agglutination	VTEC-Screen Seiken	Stx1, Stx2	25 ng/ml
Nanoparticle platform	Gold nanoparticles conjugated with Gb3 and silver enhancement	Stx1	1 µg/ml
Nanoparticle platform	Magnetic nanoparticles conjugated with Gb3 and MALDI-TOF	Stx1	330 pg/ml
(mPCR) assay	Vero cells in a three-dimensional (3D) platform	Stx1, Stx2	32 ng/ml
Lateral flow immunoassay	Based on AuNP and CdTe QD	Stx2	25 ng/ml
SERS device	2D hybrid metallic polymeric nanostructure based on the octupolar framework	Stx2	1.4 nM
AlphaLISA	Bead-based immunoassay	Stx	0.5 ng/mL

Table 3.

Overview of plasmonic approaches and traditional techniques used for Stx identification. Modified from [170].

Impact of NAB815 on the treatment of CD-1 mice exposed to free Stx2a or human blood-derived Stx2a-containing EV

NAB815, a derivative of the antibiotic polymyxin B, was found to inhibit the binding of Stx2 to TLR4 expressed by circulating cells hence impairing the release of pathogenic EV containing Stx2a. After the characterization *in vitro*, we are aiming to demonstrate the efficacy of the compound in cellular and animal models.

NAB815 reduces toxicity induced by Stx2a-containing EV to Vero cells

To assess whether NAB815 could mitigate the effects of EV-associated Stx2a, Vero cells were challenged with different amounts (0.1, 0.3, 1, and 3 µL) of EV from a representative donor. EV were obtained by incubating blood with PBS (control EV), 2 nM Stx2a (Stx2a EV), and Stx2a together with NAB815 0.01 µg/mL (Stx2a + NAB815 EV). Following 72-hour incubation, Vero cell viability was quantified. Control EV produced no measurable cytotoxicity across all tested volumes (Figure 18A, black line). Stx2a EV induced concentration-dependent cell death, reaching approximately 50% at the maximum tested volume (3 µL; Figure 18A, red line). Importantly, EV generated during co-treatment of blood with Stx2a and NAB815 exhibited reduced cytotoxic effects (Figure 18A, blue line). To validate these observations across biological replicates, fixed volumes (3 µL) of different EV preparations obtained from four independent donors were evaluated. The protective effect induced by NAB815 was significant ($p < 0.001$, Figure 18B), as the ~50% lethality induced by Stx2a-triggered EV turned out to be ~15% in the presence of the drug.

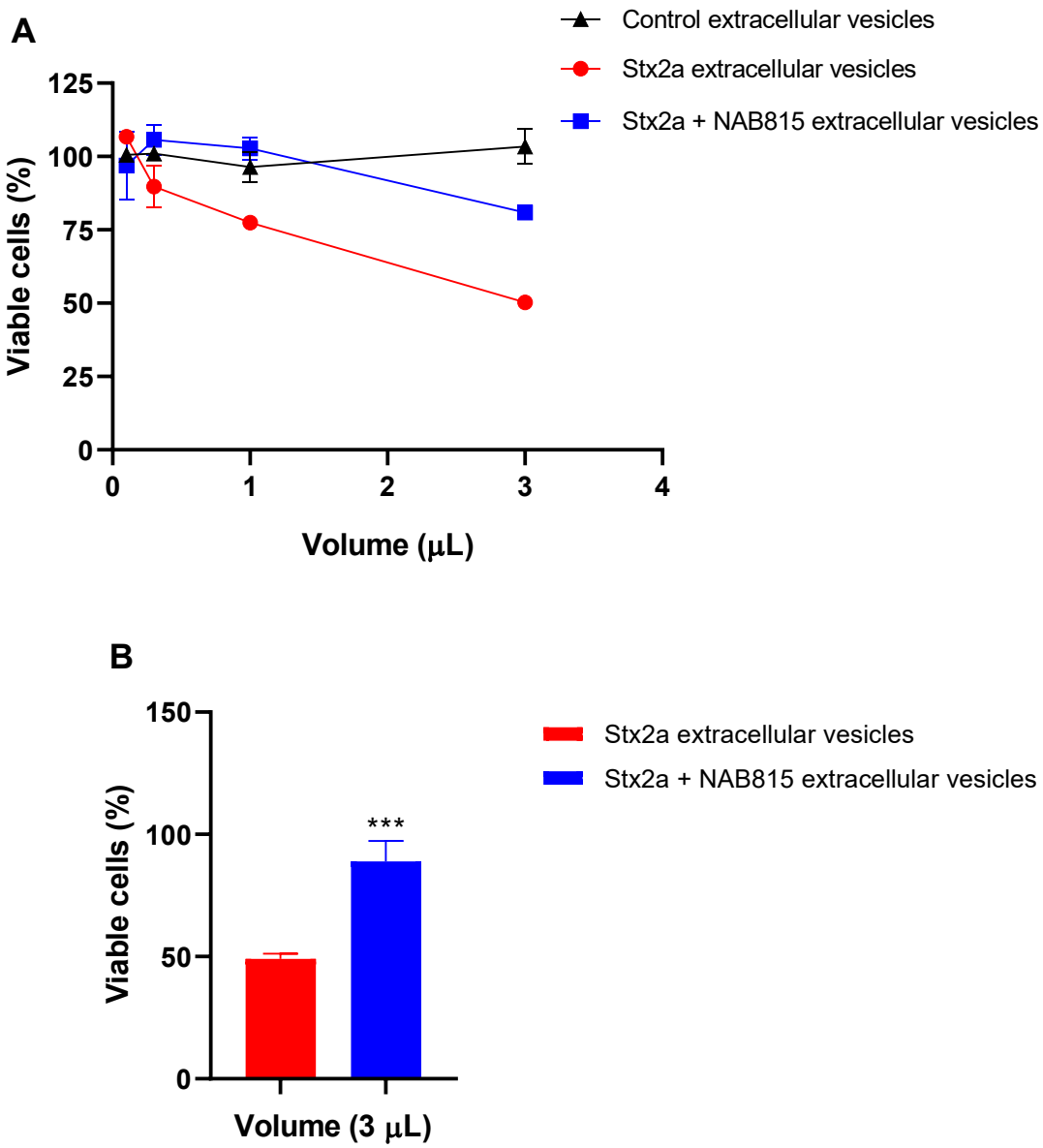

Figure 18.

(A-B) Cytotoxicity of human blood-derived EV in Vero cells. EV were purified from human blood treated with vehicle, 2 nM Stx2a, or 2 nM Stx2a + 0.01 µg/mL NAB815. Serial dilutions were applied to Vero cells, and cytotoxic effects were quantified using viability assays. **(A)** Cell viability expressed as mean percentage ± SD normalized to vehicle controls (n = 2 donors). **(B)** Pooled analysis of cell viability presented as mean ± SD relative to vehicle controls (n = 4 donors).

***$p < 0.001$ (two-tailed unpaired t-test).

NAB815 protects CD-1 mice from free Stx2a

The therapeutic potential of NAB815 was evaluated *in vivo* using female CD-1 mice administered intravenously with Stx2a at 10 or 15 pg/g body weight. In this experimental model endogenous murine EV release following Stx exposure was previously demonstrated [139]. Animals were monitored for 10 days, with blood sampling at 72 hours for renal function assessment. Serum urea analysis revealed significant renal protection at the higher toxin dose (Figure 19A). Creatinine measurements showed a similar protective trend, although statistical significance was not reached (Figure 19B). A significant drop in body weight was observed on day 3 (before the lethal effects) in animals treated with the higher dose of Stx2a, while in the presence of NAB815 no significant changes were observed (Figure 19C). Survival analysis demonstrated reduced lethality in drug-treated groups without reaching statistical significance (Figure 19D). At 10 pg/g, Stx2a induced mortality in approximately 30% of animals. Co-administration with NAB815 at this dose resulted in the death of a single animal exhibiting intestinal congestion. This presentation is atypical since Gb3Cer intestinal expression or Stx-induced intestinal damage was not previously observed in mice [85, 99, 212]. At 15 pg/g (LD_{50}), NAB815 provided clear protection since animals treated with toxin showed significantly elevated mortality versus controls, while lethality of co-treated animals was not significantly different (Figure 19D). At day 10, histopathological examination confirmed tubular damages consistent with previous studies on Stx-intoxicated CD-1 mice [99]. At 10 pg/g, lesions included epithelial hydropic degeneration (Figure 19E), tubular cell detachment (Figure 19F), tubular dilation and epithelial atrophy and necrosis. PAS staining of kidneys from 15 pg/g-treated animals allowed the differentiation of proximal and distal tubules based on brush border architecture. Distal tubules exhibited hydropic degeneration (Figure 19G), while coagulative necrosis was present mainly in proximal tubules (Figure 19H) in which basal membranes or cellular details are not always visible, and many nuclei are pycnotic or dissolved (karyolysis). Blinded semi-quantitative histopathologic scoring revealed significantly reduced kidney damage in NAB815-co-treated animals relative to animals treated with Stx2a ($p < 0.05$, Figure 19I).

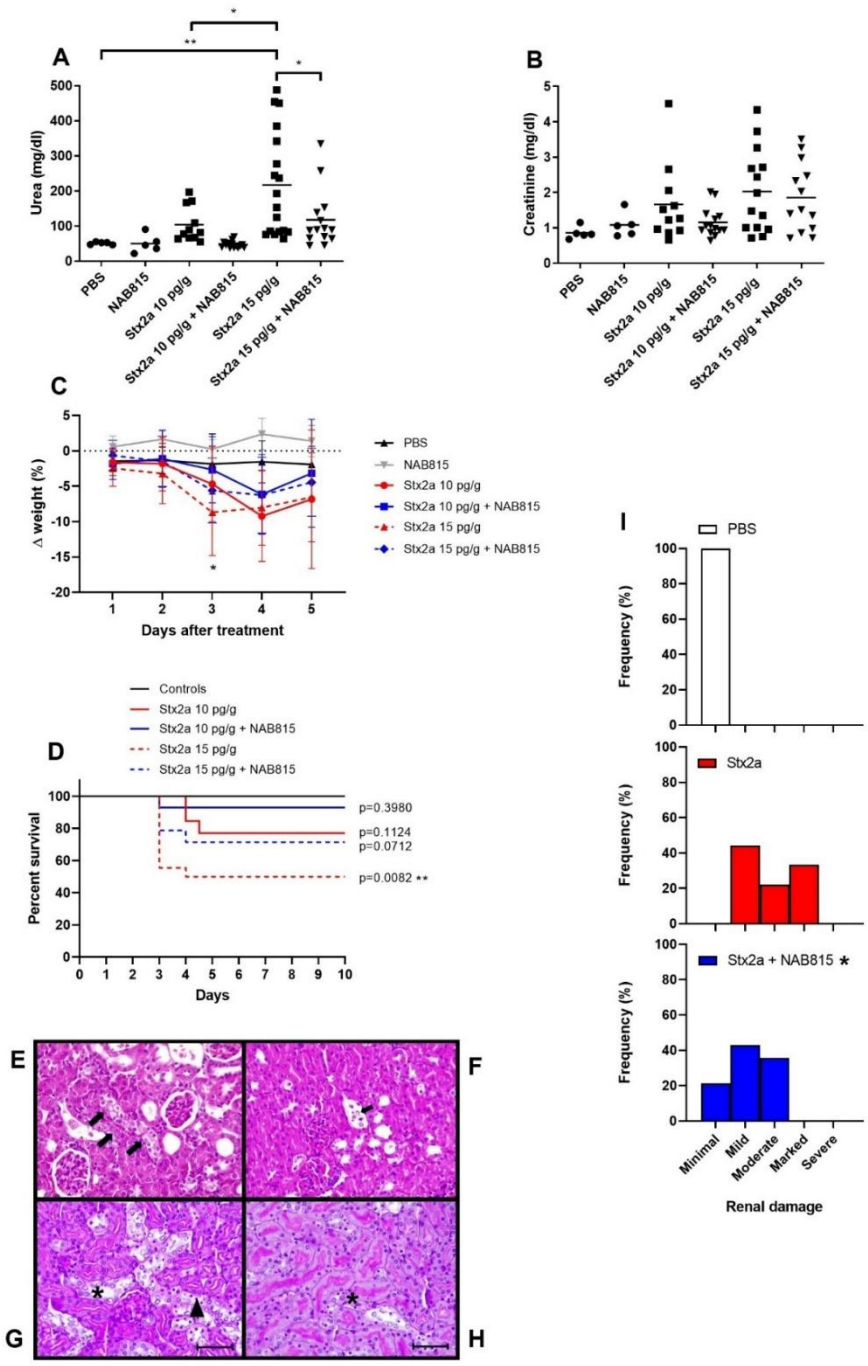

Figure 19.

(A-I) NAB815 protection against free Stx2a in CD-1 mice. CD-1 mice received intravenous injections of free Stx2a at 10 or 15 pg/g either alone (n = 13 and n = 18, respectively) or combined with 0.01 µg/mL NAB815 (n = 14 and n = 14, respectively). Vehicle controls (n = 5) and NAB815-only controls (n = 5) were included for comparison. **(A, B)** Serum urea and creatinine levels, respectively. Data are mean values; *$p < 0.05$, **$p < 0.001$ (one-way ANOVA with Tukey's multiple comparison test). **(C)** Body weight changes. Data are presented as mean ± SD; the 15 pg/g Stx2a group differed significantly from vehicle controls (*$p < 0.05$, one-way ANOVA with Dunnett's

multiple comparison test). **(D)** Survival analysis assessed via log-rank (Mantel-Cox) test; p-values calculated relative to pooled controls (PBS- and NAB815-treated groups, n = 10). **(E-F)** Representative kidney histology, 10 pg/g Stx2a treatment. **(E)** Arrows indicate tubular epithelial cells exhibiting increased volume and cytoplasmic clearing (hydropic degeneration); **(F)** arrow shows sloughed epithelial cells within tubular lumen. Hematoxylin-eosin, 40× magnification. **(G-H)** Representative kidney histopathology analysis, 15 pg/g Stx2a injection. **(G)** Distal tubules display hydropic degeneration (asterisk), pyknotic nuclei (arrowhead); **(H)** pyknotic nuclei (asterisk). PAS stain, scale bar = 50 μm. **(I)** Semi-quantitative renal injury scoring in PBS-treated controls (n = 5) and mice receiving 15 pg/g Stx2a without (n = 18) or with (n = 14) NAB815. ATI severity assessed on PAS-stained sections using the following scale: minimal, <10% parenchymal involvement; mild, 11–25%; moderate, 26–50%; marked, 51–75%; severe, >75%. *$p < 0.05$, Stx2a versus Stx2a + NAB815 (two-tailed Mann-Whitney test).

NAB815 reduces the renal damage induced by human Stx2a - EV in mice

Since in circulating cells the expression pattern of Gb3Cer and TLR4 receptors differs considerably in mice and humans and considering the lack of the Stx2a-modulating factor HuSAP in mice, a humanized model was developed using intravenous administration of human blood cell-derived EV (10,400–20,800 × g). CD-1 mice received 5 ID_{50}/g (Vero viability assay) of pooled EV isolated from Stx2a-treated blood from eight donors. Equivalent volumes of control EV, NAB815-alone EV, or Stx2a + NAB815 EV were administered for comparison. No mortality occurred across experimental groups, and body weights remained comparable throughout the 10-day observation period (Figure 20C). Mice receiving control or NAB815-derived EV showed normal serum urea and creatinine (Figures 20A, 20B). Urea levels were significantly higher in animals treated with Stx2a - EV compared to both the Stx2a + NAB-treated group and the negative control group (Figures 20A). Additionally, the same trend was observed with serum creatinine values, although differences were not significant (Figure 20B).

Histopathology analysis (day 10) revealed tubular lesions in Stx2a - EV-treated mice similar to those induced by free toxin (Figures 20E, 20F). Semi-quantitative histological scoring indicated a protective effect in NAB815-co-treated animals without achieving statistical significance (Figure 20G). Quantification of acute tubular injuries demonstrated an increasing number of injured cells in Stx2a - EV treated mice compared with control EV, an effect absent in all other treatment groups (Figure 20D), confirming the protective effect afforded by NAB815 at non-bactericidal concentrations. In conclusion, both mouse models

clearly demonstrated that a drug capable of perturbing the Stx2a/TLR4 interaction is effective in preventing renal damage despite the lack of effects on Stx2/Gb3Cer interaction.

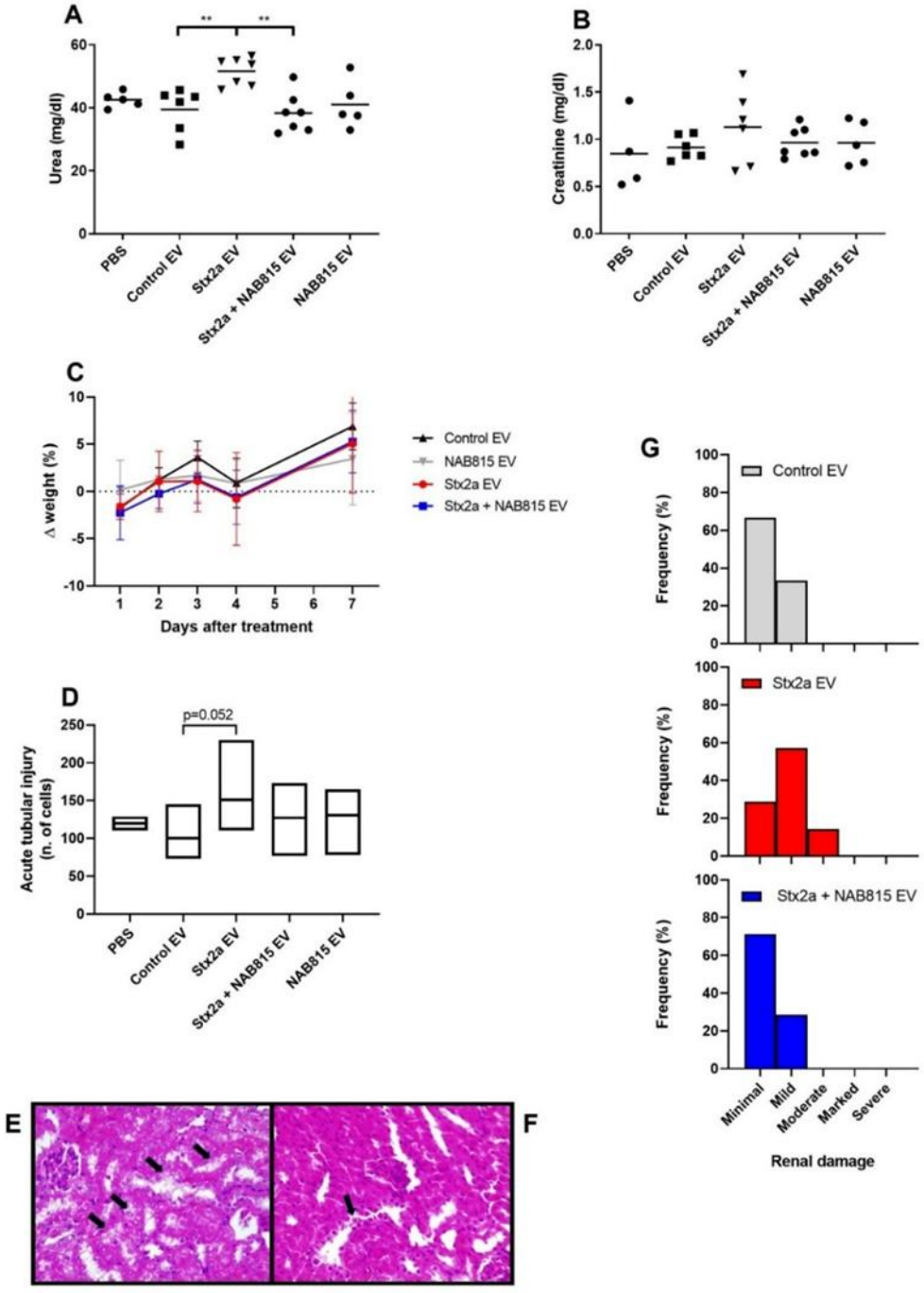

Figure 20.

(A–G) NAB815 protection against renal toxicity induced by Stx2a-containing human EV in CD-1 mice. CD-1 mice received intravenous injections of PBS vehicle (n = 5), control EV from untreated blood (n = 6), EV from 2 nM Stx2a-treated blood (n = 7), or EV from blood co-treated with 2 nM Stx2a plus 0.01 μg/mL NAB815 (n = 7). **(A, B)** Serum urea and creatinine levels, respectively. Data

are mean values; *$p < 0.05$, **$p < 0.01$ (one-way ANOVA with Tukey's multiple comparison test). **(C)** Body-weight alterations. Data are presented as mean ± SD. The Stx2a EV group differed significantly from controls (*$p < 0.05$, one-way ANOVA with Dunnett's multiple comparison test). **(D)** ATI quantification, determined as described in Methods; *$p < 0.05$ for Stx2a EV versus control EV (one-way ANOVA with Dunnett's multiple comparison test). **(E–F)** Representative renal histopathology (day 10). **(E)** Arrows indicate tubules with epithelial cells exhibiting increased volume and cytoplasmic clearing (hydropic degeneration); **(F)** arrow marks sloughed epithelial cells within the tubular lumen. Hematoxylin-eosin stain, 40× magnification. **(G)** Semi-quantitative renal injury scoring in mice treated with control EV (n = 6), Stx2a EV (n = 7), or Stx2a + NAB815 EV (n = 7). ATI severity graded on PAS-stained sections according to parenchymal involvement: minimal (<10%); mild (11–25%); moderate (26–50%); marked (51–75%); severe (>75%). Stx2a EV versus Stx2a + NAB815 EV (two-tailed Mann-Whitney test).

Assessment of SOS response activation and Shiga toxins production by the antibiotic derivative NAB815 in *E. coli* strains

NAB815 was found to be effective at very low concentrations (0.01 µg/mL) in protecting mice from Stx2a-induced renal damage. Since antibiotics are not recommended for the treatment of STEC-infected patients due to the well-known effect on bacterial SOS response and subsequent enhanced Stx release [10, 72, 74, 75], we sought to evaluate if NAB815 at this non-bactericidal dosage is safe.

Kinetic evaluation of the effects of NAB815 at sub-bactericidal concentrations on SOS response and Stx release using reporter *E. coli* strains

The potential of sub-inhibitory concentrations of NAB815 to induce bacterial SOS response, phage activation, and Stx production was first assessed using fluorescence-based reporter assays in genetically engineered *E. coli* strains. Specifically, SOS activity (*recAP::cfp*), toxin expression (*stx1::yfp* or *stx2::yfp*), and bacterial growth (OD_{595}) were monitored in real time in *STEC* O157:H7 EDL933 Δ*stx2 stx1::yfp* pMBM25 [72] and *STEC* O104:H4 *stx2::yfp* pKB1 *recAP::cfp*.

NAB815 was tested at 0.01 µg/mL, corresponding to the antibiotic concentration that was effective in protecting mice; additional concentrations (0.1 µg/mL and 1 µg/mL) were also evaluated. Similar concentrations of polymyxin B, the parental drug, were included as reference whereas PBS and ciprofloxacin (0.05 µg/mL 0.1 µg/mL) served as negative and positive controls, respectively.

In the O157:H7 reporter strain, NAB815 and polymyxin B at the highest tested concentration did not affect bacterial growth. OD_{595} values and RecAP-CFP fluorescence remained comparable to the PBS control (Figure 21C-D, black dots and red diamonds). In contrast, exposure to 0.1 µg/mL ciprofloxacin produced a marked SOS response, characterized by a RecAP-CFP fluorescence peak at approximately 120 minutes followed by a decrease in OD_{595} after 180 minutes (Figure 21B, black dots and red diamonds). A weaker response was detected at 0.05 µg/mL ciprofloxacin (Figure 22). For this reason, this concentration was therefore not used for subsequent analyses. Across the different antibiotic treatments, only ciprofloxacin at both tested doses resulted in a significant activation of the SOS response compared to PBS control, as shown in Figure 22 ($p < 0.0001$). Finally, the obtained time-resolved data corroborate with previous studies which involved the same *STEC* O157:H7 EDL933 Δ*stx2 stx1::yfp* pMBM25 engineered strain treated with

ciprofloxacin [72]. Despite strong SOS activation in the ciprofloxacin-positive control, *stx1a* gene expression was not detected during the experimental timeframe, suggesting a transient uncoupling between SOS activation and Stx1a synthesis or impairment in Stx1a phage induction (Figure 21B, blue diamonds). Similarly, the highest concentration of the other antibiotics did not result in *stx1* gene expression in the expected timeframe following SOS response activation (Figure 21, blue diamonds).

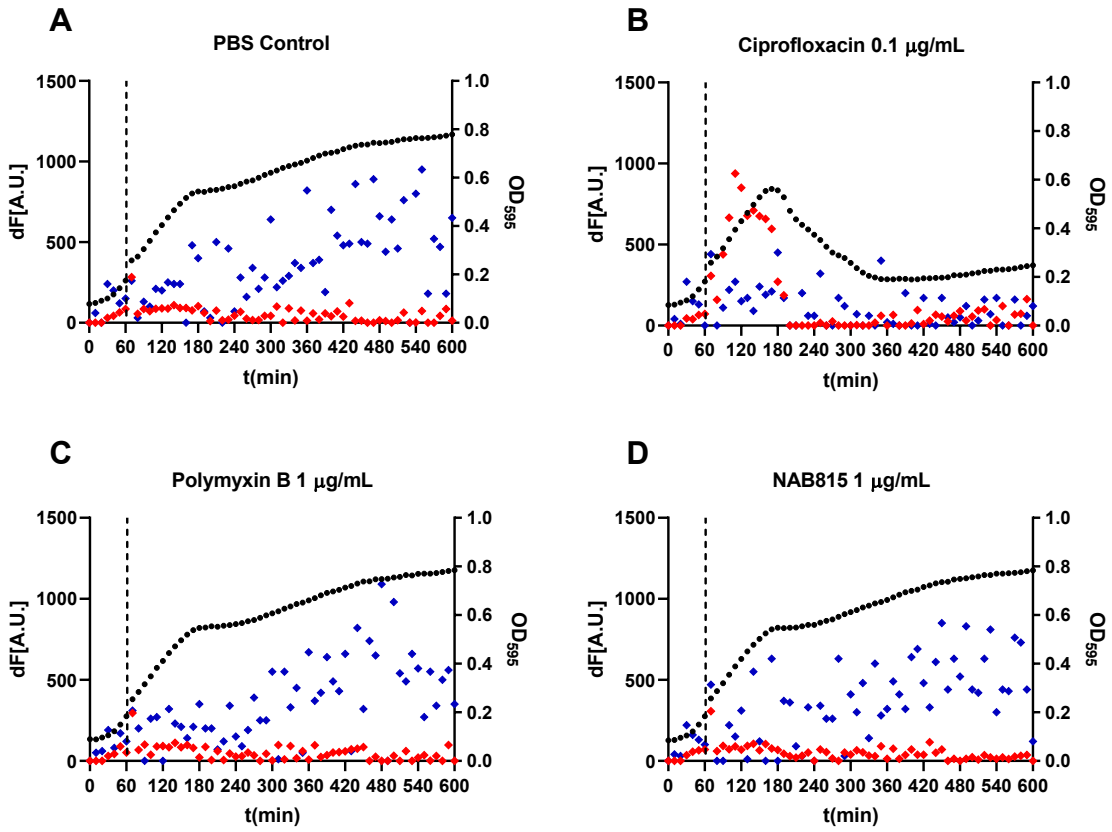

Figure 21.

(A-D) Kinetics of SOS response and Stx1 expression in *STEC* O157:H7 EDL933 Δ*stx2 stx1::yfp* pMBM25 exposed to sub-bactericidal concentrations of polymyxin B and NAB815. Shown are growth curves (black dots; OD_{595}), SOS response (*recAP::cfp*, red diamonds), and *stx1a* gene expression (*stx1::yfp*, blue diamonds) represented as increases in fluorescence over time (ΔF [A.U.]). Samples were monitored for 1,200 min (20 hours). After 60 minutes (indicated by the dashed line), cultures were treated with the corresponding antibiotic, according to the Materials and methods section. A single representative experiment is shown out of three technical replicates derived from three independent biological experiments..

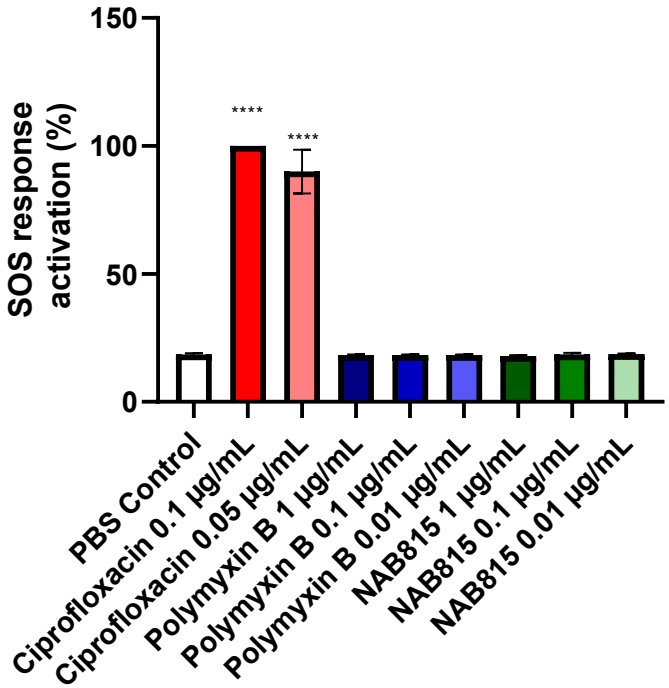

Figure 22.

Assessment of SOS response activation in *STEC* O157:H7 EDL933 Δ*stx2 stx1::yfp* pMBM25 following exposure to sub-bactericidal concentrations of polymyxin B and NAB815 (blue and green bars, respectively). Fluorescence data were normalized to the ciprofloxacin-treated positive control (highest antibiotic concentration, red bar). PBS (white bar) served as the negative control for statistical comparisons. Shown is the SOS response (total CFP) of the indicated treatments between 60- and 200-min. Bars represent mean values from three technical replicates derived from three independent biological experiments ± SD. **** $p < 0.0001$ (one-way ANOVA followed by Holm's multiple comparison test).

Experiments performed with the Stx2a-producing *STEC* O104:H4 *stx2::yfp* pKB1 *recAP::cfp* reporter strain confirmed and extended the findings described above. Due to the higher ciprofloxacin tolerance of this strain, different doses of this antibiotic were tested (0.5, 0.25, 0.125, 0.0625 µg/mL). All NAB815 and polymyxin B treatments had no detectable effect on bacterial growth or fluorescence (Figures 23-25), indicating the absence of SOS or *stx2a* activation. In contrast, ciprofloxacin triggered a pronounced SOS response, peaking at 190 minutes, followed by *stx2a* gene expression between 230 and 370 minutes (Figure 23B, red and blue diamonds). This response was accompanied by a decline in OD_{595} after 280 minutes (Figure 23B, black dots). Notably, statistically significant activation of both the SOS response and *stx2a* gene expression was observed only in O104:H4 samples

treated with ciprofloxacin at 0.25 or 0.125 µg/mL, whereas all other antibiotic treatments showed no combined significant effect compared with the PBS control (Figure 24A-B, $p < 0.0001$).

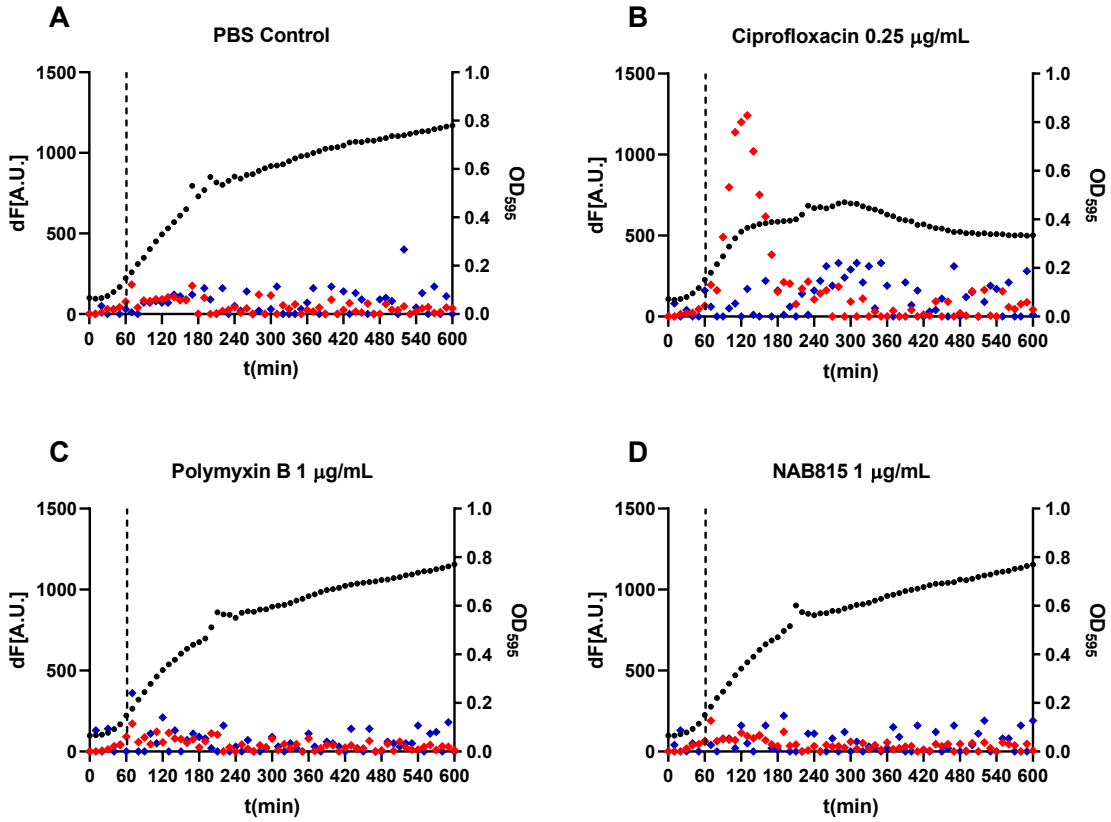

Figure 23.

(A-D) Kinetics of SOS response and *stx2a* gene expression in *STEC* O104:H4 *stx2::yfp* pKB1 *recAP::cfp* exposed to sub-bactericidal concentrations of polymyxin B and NAB815. Shown are growth curves (black dots; OD), SOS response (*recAP::cfp*, red diamonds), and *stx2* expression (*stx2::yfp*, blue diamonds) represented as increases in fluorescence over time (ΔF [A.U.]). Samples were monitored for 1200 min (20 hours). After 60 minutes (indicated by the dashed line), cultures were treated with the corresponding antibiotic, according to the Methods section. A single representative experiment is shown out of three technical replicates derived from three independent biological experiments.

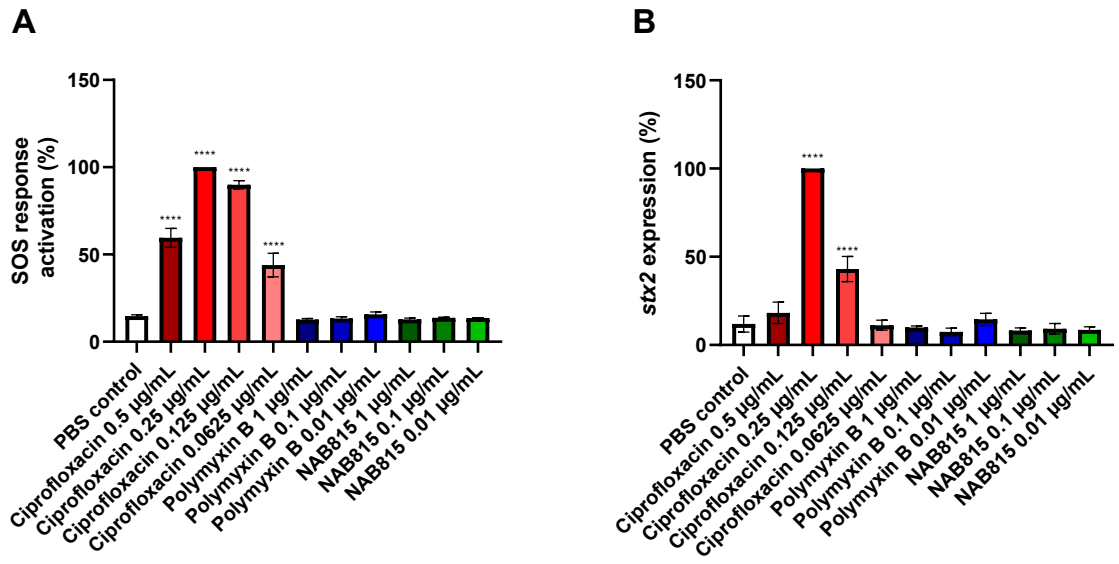

Figure 24.

Evaluation of **(A)** SOS response activation and **(B)** *stx2a* expression in *E. coli* O104:H4 *stx2::yfp* pKB1 *recAP::cfp* following exposure to sub-bactericidal concentrations of polymyxin B and NAB815 (blue and green bars, respectively). PBS (white bar) and ciprofloxacin (red bar) were used as negative and positive controls, respectively. Shown are the SOS responses (total CFP) of the indicated treatments between 60 and 200 min, and *stx2a* gene expression between 220 and 370 minutes. Bars represent mean values from three technical replicates derived from three independent biological experiments ± SD. **** $p < 0.0001$ (one-way ANOVA followed by Holm's multiple comparison test).

To assess potential morphological changes induced by antibiotic treatments, 5 µL from each well was examined under a 40× fluorescence microscope at the end of the 20-hour experiment, as reported in Figure 25. Among all treatments, only ciprofloxacin caused morphological alterations, leading to elongated cell shapes. Consistently, only ciprofloxacin treated cells exhibited CFP^+/YFP^+ fluorescence (Figure 25). Overall, these results using reporter STEC strains indicate that, unlike ciprofloxacin, sub-bactericidal concentrations of polymyxin B and its derivative NAB815 do not trigger the bacterial SOS response in STEC strains carrying *stx1* and/or *stx2* genes.

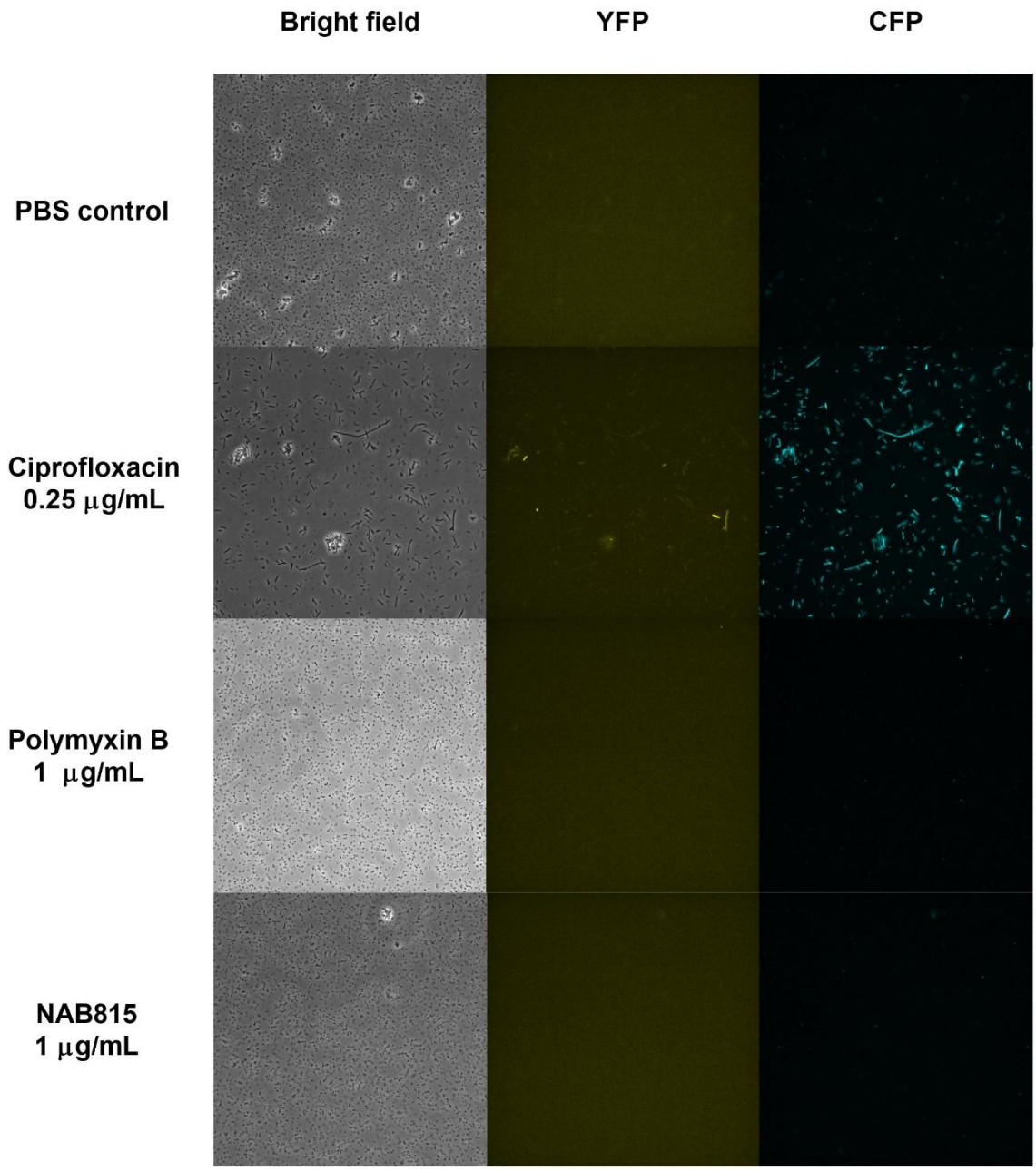

Figure 25.

Fluorescence microscopy of the *STEC* O104:H4 *stx2::yfp* pKB1 *recAP::cfp* strain after antibiotic treatment. Following 20 hours of incubation, 5 µL from each culture was analyzed for morphological changes and YFP/CFP fluorescence, corresponding to *stx2* and *recAP* (SOS response) expression, respectively. The highest polymyxin B and NAB815 concentrations are reported in the table. Only the 0.25 µg/mL ciprofloxacin treatment is shown, as it produced the strongest SOS response and *stx2a* gene induction. Only ciprofloxacin treatment induced morphological changes and YFP/CFP fluorescence, indicating activation of the SOS response and *stx2a* gene expression. Magnification: 40×.

Evaluation of Stx production after NAB815 and polymyxin B sub-bactericidal treatments of Stx1a- and Stx2a-producing clinical isolates

The effects of NAB815 and polymyxin B on Stx production were further evaluated in clinical STEC isolates producing either Stx1a or Stx2a. Cultures were treated for 20 hours with 0.01 and 0.1 µg/mL of each antibiotic as well as with PBS and with 0.1 µg/mL ciprofloxacin as negative and positive controls, respectively. Aliquots (12 µL) of the 20× concentrated supernatants were analyzed by Western blot. In the Stx1a-producing strain, only ciprofloxacin induced a statistically significant increase in toxin levels compared with PBS (Figure 26A; $p = 0.0002$). NAB815 and polymyxin B produced minor, non-significant changes at both tested concentrations. Similarly, in the Stx2-producing strain, significant toxin induction was observed only with ciprofloxacin (Figure 26B; $p < 0.0001$), while NAB815 and polymyxin B had no detectable effect. Compared with the Stx1a strain, the semi-quantitative Western blot analysis of the Stx2a-producing strain treated with ciprofloxacin revealed lower induction of toxin expression (see the different y-axis scale in Figure 26A, B).

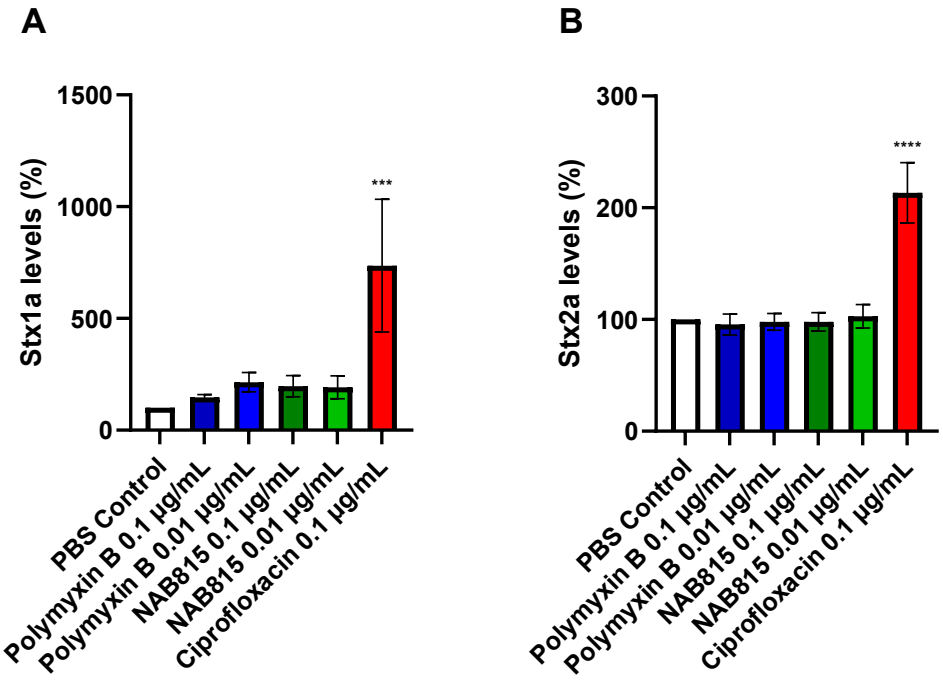

Figure 26.

(A-B) Effects of sub-bactericidal doses of NAB815 and polymyxin B on Stx production in clinical STEC isolates assessed by Western blot. (**A**) Stx1a- and **(B)** Stx2a-producing strains were treated with 0.01 or 0.1 µg/mL of each compound, while PBS and 0.1 µg/mL ciprofloxacin served as controls.

With respect to PBS negative control, only ciprofloxacin significantly increased Stx production (Stx1a, $p = 0.0002$; Stx2a, $p < 0.0001$). Mean values are based on three technical replicates of each independent biological triplicates and are expressed as mean ± SD. Statistical significance was determined using one-way ANOVA followed by Holm's multiple comparison test (**$p = 0.0002$; ****$p < 0.0001$).

Finally, the 20× concentrated supernatants from clinical Stx1a- and Stx2a-producing isolates, treated with the different antibiotics, were applied to Vero cells at final dilutions of 1:1000 (0.02×) and 1:100 (0.2×), respectively. The well-known different sensitivity of Vero cells to Stx1a and Stx2a, with Stx1a being approximately 10 times more cytotoxic [158], explains the use of different concentrations in the experimental settings. After 72 hours, cytotoxicity was measured using a crystal violet cell viability assay (absorbance at 570 nm). Only supernatants from ciprofloxacin-treated bacteria producing Stx1a induced a significant increase in cytotoxicity compared with PBS control (Figure 27A; $p = 0.0037$), consistent with the enhanced Stx1a levels observed by Western blot analysis. Supernatants from NAB815- or polymyxin B-treated cultures showed no significant differences relative to control. Similarly, ciprofloxacin-treated supernatants from bacteria producing Stx2 caused a significant albeit modest, increase in cytotoxicity (Figure 27B; $p = 0.0119$), whereas NAB815- or polymyxin B-treated showed no significant cytotoxic effects relative to PBS control. Consistent with the Western blot results, Stx2a-containing supernatants resulted in a lower cytotoxic response compared with those from Stx1a-producing cultures [99].

In conclusion, these findings confirm that sub-bactericidal doses of the antibiotic derivative NAB815 do not induce the bacterial SOS response and, consequently, do not increase Stx release by STEC bacteria. Although current guidelines discourage the use of antibiotics in STEC infections due to the risk of exacerbating the disease, the concept of using very low doses of an antibiotic derivative for its ability to inhibit the formation of Stx-containing EV through impairment of Stx2a/TLR4 interactions and not for its antimicrobial activity seems promising for the management of STEC patients.

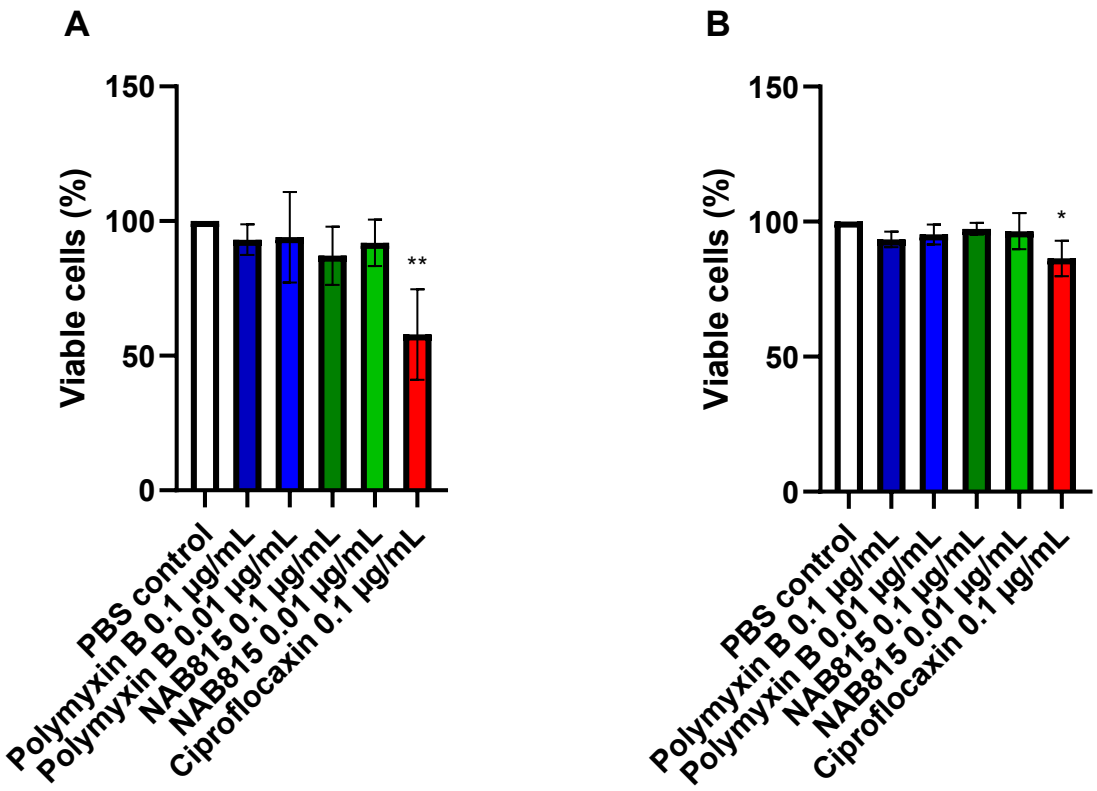

Figure 27.

(A-B) Effects of sub-bactericidal doses of NAB815 and polymyxin B on functional Stx production in clinical STEC isolates, assessed via crystal violet cell viability assay on Vero cells. Clinical STEC strains producing Stx1a or Stx2a were first treated with sub-bactericidal concentrations of PBS, polymyxin B, NAB815, and ciprofloxacin. The resulting bacterial supernatants were collected, concentrated, and applied to Vero cells at 0.02× final concentration for Stx1a and 0.2× for Stx2a. Compared to PBS control only supernatants from ciprofloxacin-treated cultures induced a significant increase in cytotoxicity for both Stx1a **(A)** and Stx2a **(B)**. Data represent the mean ± SD of three technical replicates from three independent biological replicates. Statistical analysis was performed using one-way ANOVA followed by Holm's multiple comparison test (**p = 0.0037; *p = 0.0119).

Discussion

Differential contribution of Stx1 and Stx2 to EV-mediated HUS pathogenesis

During STEC infections, the probability of developing HUS is strongly influenced by the type of Stx produced by the microorganism, being highest when Stx2a is expressed alone, near zero when strains produce only Stx1a, and intermediate when both toxins are present [24]. This pattern has led to extensive comparisons of Stx1a and Stx2a toxicity in cell and animal models.

Although Stx1a is ~10 folds more potent than Stx2a in Gb3-Cer expressing Stx sensitive Vero cells, probably due to its stronger binding to the Gb3Cer receptor that promotes cell entry, the A1 fragment of Stx2a shows greater affinity for ribosomes, leading to stronger inhibition of protein synthesis in human cells [77, 158]. The differences observed between Stx1a and Stx2a in cellular models therefore cannot fully account for the clinical evidence.

In line with human epidemiological data, animal studies confirmed that Stx2a is more ominous than Stx1a. In mice, Stx2a is markedly more toxic than Stx1a, with an LD_{50} approximately 100-fold lower when parenterally administered [159]. After oral administration the LD_{50} of Stx2a was found to be 2.8 µg/mouse, by contrast, Stx1a showed no toxicity even at 157 µg/mouse [159]. Despite Stx1a and Stx2a exhibited similar systemic and kidney targeting, co-administration of Stx1a with Stx2a resulted in reduced toxicity in the same animal model. This protective effect was further confirmed using a Stx1a toxoid with a defective A chain, suggesting that Stx1a competes with Stx2a for Gb3Cer binding sites on renal endothelial cells, thereby lowering overall toxicity [159]. During the three-year PhD project, we aimed to elucidate the mechanisms underlying the protective effects induced by Stx1 during STEC infections by strains co-producing Stx1a and Stx2a through *in vitro* modeling of toxin-blood cell interactions. Characterization of Stx-containing EV revealed that Stx1a attenuates the effects of the HUS-triggering Stx2a. Combined exposure of blood cells to both toxins resulted in reduced EV quantity, dimensions, and lower Stx2a content compared to exposure with Stx2a alone. The combined treatment led to the reduction of large Stx-containing EV, the most pathogenic form associated with progression from bloody diarrhea to overt HUS, resulting in complete disappearance of EV larger than 300 nm [131].

These findings support the hypothesis that in infections involving STEC strains capable of producing both toxins, Stx1a may exert a protective effect through competitive receptor binding, occupying sites that would otherwise be available to Stx2a. This competitive mechanism could operate at two critical stages: during direct intoxication of target cells via the Gb3Cer receptor, and during early toxemia, when Stx bind circulating cells through Gb3Cer (monocytes and platelets) or TLR4 (neutrophils, monocytes, and platelets), thereby impairing the formation and release of Stx2a-containing EV. The higher binding affinity of Stx1a for Gb3Cer provides a molecular basis for this protective mechanism, potentially explaining the milder clinical outcomes observed in infections involving strains that produce both toxins.

Implications for rapid Shiga toxin diagnostics

Current diagnostic methods for the detection of STEC infections are time-consuming and rely on specialized facilities and trained personnel [160]. Since early and accurate diagnosis is critical for preventing the onset of HUS and its associated life-threatening complications, the development of new rapid and accessible diagnostic alternatives is essential. To overcome these limitations, the three-year PhD project included a collaboration with the Consiglio Nazionale delle Ricerche (CNR, Pozzuoli, Naples), which led to the establishment of a biosensor for simple and rapid detection of Stx [170].

The obtained results demonstrate the analytical capabilities of an engineered plasmonic metasurface for detecting and discriminating different Stx through SERS spectroscopy combined with PCA analysis. The hexagonal arrangement of asymmetric nanocavities, fabricated via electron beam lithography, provided strong near-field enhancement and hot-spot distribution, making it particularly suitable for biosensing applications. Two complementary approaches were evaluated: label-free detection using unfunctionalized substrates and antibody-mediated recognition with functionalized platforms. The unfunctionalized approach successfully distinguished between Stx1a, Stx2a, and cleaved Stx2a based on their spectral fingerprints. Notably, the SERS analysis revealed distinct structural features, particularly for the cleaved form, which exhibited unique peaks, confirming significant structural changes following proteolytic processing. PCA analysis transformed subtle spectral variations into reliable and reproducible differences among the three toxins.

The functionalized approach demonstrated remarkable sensitivity, achieving detection limits of 6.8 pM for Stx1a and 2 pM for Stx2a, these concentrations are below those typically found in patients' sera (~30-90 nM, corresponding to 2–6 ng/mL by ELISA) before HUS development [131]. Importantly, the system successfully differentiated between native and cleaved Stx2a despite using the same antibody, highlighting how SERS-PCA analysis captures fine structural distinctions that may correlate with different pathogenic roles.

These findings establish the proposed platform as a promising tool for point-of-care diagnostics of STEC infections. By enabling rapid identification of toxin subtypes and distinguishing between low-risk (Stx1-producing) and high-risk (Stx2-producing) strains, the system could guide a personalized therapeutic approach, promptly initiating supportive therapy upon STEC infection diagnosis or, in the case of HUS, targeted drug treatment. Furthermore, discriminating between native and cleaved Stx2a variants opens new perspectives for investigating their differential contributions to HUS pathogenesis. Our method represents a valid alternative to conventional Stx detection systems and can be integrated with other on-chip biological devices to realize portable point-of-care diagnostics. Future work will focus on validating the system in complex biological matrices, such as human sera, and on developing a prototype for rapid Stx detection, with potential commercialization of Portable Plasmonic Platforms in high-growth photonics applications. The creation of a spin-off could further advance these concepts to technology readiness levels suitable for commercial product development.

Targeting EV formation with NAB815

Nowadays, no specific therapeutic interventions exist to prevent HUS development in STEC-infected patients nor to treat patients after diagnosis of the syndrome, leaving clinical management dependent on supportive care. Recent research has identified NAB815, a non-toxic polymyxin B derivative, as a promising therapeutic candidate [177, 203]. At the 0.01 μg/mL dose, a concentration approximately 200-fold lower than its MIC, NAB815 showed to successfully inhibit the binding between Stx2a and TLR4, resulting in the reduction of both leukocyte-platelet aggregate formation and large Stx2a-containing EV release [177]. Specifically, EV isolated from human blood treated with Stx2a in the presence of NAB815 (0.01 μg/mL) showed reduced number and size, and a lower toxic cargo compared to Stx2a-stimulated EV, as documented by measuring Stx2a content within the

vesicles. These changes resulted into functional protection, as demonstrated by the significantly reduced toxicity of EV obtained by challenging human blood with Stx2a and NAB815 when tested on Vero cells [177].

To determine whether these laboratory findings translated into meaningful protection against systemic toxemia*, in vivo* studies were conducted to evaluate the safety and efficacy of NAB815. Several animal models are available for studying the onset of HUS triad and, in particular, renal damage. Some models involve STEC infection of animals (mice, calves, chicks), while others rely on intravenous or intraperitoneal administration of Stx2 (mouse, rat, baboon, dog, rabbit) [213]. In this project female CD-1 mice were challenged according to two different experimental protocols, one including treatment of animals with free-soluble Stx2a ± NAB815, the second based on intoxication of mice with human blood-derived EV isolated in the presence of Stx2a ± NAB815.

In the first experimental approach, an already established setting [99, 212, 214, 215], CD-1 mice received intravenous injections of free Stx2a at doses of 10 or 15 pg/g, which approximately corresponded to LD_{30} and LD_{50}, respectively. Co-treatment with 0.01 μg/mL NAB815 protected mice from acute renal failure induced by Stx2a treatment, with drug significantly reducing pathologic serum urea levels, particularly at the higher toxin dose. Animals treated with Stx2a alone exhibited marked weight loss by day 3, whereas those receiving the combined treatment showed body weight comparable to controls, suggesting that NAB815 effectively mitigated the systemic effects of intoxication. Survival analysis revealed a reduced mortality trend in NAB815-treated groups, with histopathological examination confirming significant attenuation of tubular damage compared to mice receiving Stx2a alone.

The second experimental model was designed to closely reproduce the pathogenic mechanism observed in patients with STEC infection. In this context, EV-associated Stx2a is released as a consequence of interactions between the toxin and circulating blood cells, resulting in particulate Stx2a that, through blood circulation, can reach and target the kidneys. Therefore, to mimic this condition, animals were exposed to human blood-derived Stx2a-containing EV. The analysis of serum urea and creatinine levels revealed a protective effect exerted by the drug. Notably, Stx2a + NAB815-EV-treated animals exhibited renal parameters normalized to control levels, demonstrating that the drug effectively prevented the formation of pathogenic vesicles during the blood treatment phase. However, the injection of Stx2a-carrying EV resulted in reduced toxic effects than expected on the basis of the measured Stx2a content. This reduction may be explained by the −80 °C long term

storage of EV, prepared weeks before the mice challenge, a condition known capable of affecting their integrity [216]. Interestingly, urea levels proved to be a better predictor of acute kidney failure than creatinine values, a trend consistently observed in both experimental designs. While creatinine changes mainly indicate kidney impairment in animals with comparable diet and physical activity, urea elevations reflect combined glomerular and tubulointerstitial pathology. Species-specific receptor distribution patterns help explain these findings. Murine kidneys express the Gb3Cer receptor exclusively on tubular cells, while human renal tissue displays this receptor across multiple cells including glomerular endothelium, tubular cells, podocytes, and mesangial cells [85]. Histological examination, according to the different Gb3Cer expression distribution pattern, revealed tubular damage in toxin exposed animals.

Although the CD-1 mouse model allowed the evaluation of both free and vesicle-associated Stx2a pathways, it does not fully recapitulate the related human HUS. A mouse model of oral infection by STEC strains upon antibiotic administration would allow the natural release of the toxin in the gut, therefore more closely reproducing the events in the course of human infections. However, intrinsic limitations exist in all mice models including (i) different Stx targets in the kidney, (ii) different patterns of circulating cell-receptors, and (iii) different Stx-interacting molecules in blood. Indeed, as previously stated, Stx2 interacts with target organs via Gb3Cer, while the binding to circulating human cells occurs through both Gb3Cer and TLR4, and, finally, in human blood HuSAP interacts with Stx2. These species-specific features are critical for modeling human HUS pathogenesis.

Moreover, direct injection of Stx2a revealed an unexpected finding. Although NAB815 inhibits the interaction between Stx2a and TLR4 without interfering with the primary Gb3Cer receptor on target cells, it still provided protection in mice treated with Stx2a. It should be noted that TLR4 is considered a co-receptor, which facilitates the intoxication of target Gb3Cer-expressing cells by Stx. Indeed, human umbilical endothelial cells or cancer cells showed reduced Stx binding upon small interfering RNA-mediated TLR4 depletion [124]. The observed protection may result from NAB815 interference with Stx2a binding to TLR4 expressed on mice renal tubular epithelium, where both receptors are expressed [217]. However, NAB815 was not present when isolated EV were injected into mice, since the washing steps during vesicle preparation removed the drug. Additionally, when mice received a 100 μL injection of free Stx2a mixed with NAB815 at 0.01 μg/mL, the drug quickly diluted throughout the mouse bloodstream (~1.3 mL total volume in a 20-

gram mouse [189]), dropping the concentration approximately 10-fold. At these reduced levels, it is unlikely that the drug effectively blocks TLR4 from acting as a co-receptor.

These observations suggest that vesicle-associated toxin represents the primary pathogenic toxin form even in rodents. This observation is particularly interesting given that mice lack natural serum inhibitors like HuSAP found in humans, revealing a critical mechanistic difference: in mice, free Stx2a can damage kidneys through two separate pathways, either by triggering vesicle release from circulating blood cells or by binding directly to kidney cell receptors. Although NAB815 only prevents the vesicular pathway, it still provides substantial protection in intoxicated animals, indicating that vesicle-mediated delivery represents the primary threat even when direct access remains possible. Differently, in humans HuSAP naturally blocks free toxin activity, effectively eliminating the direct pathway and forcing the toxin to circulate predominantly in vesicle-associated form via vesicle binding. Since NAB815 specifically hinders the vesicular pathway, the only route of toxin delivery in humans, in patients the proposed therapeutic intervention could be even more effective. Additionally, NAB815 might block Stx2a binding to TLR4 acting as a co-receptor on kidney cells when administered at therapeutic dosing schedules (three times daily) designed to maintain plasma concentrations at the active level (0.01 μg/mL).

Further validation of these findings could come from studies using animal models closer to humans, such as baboons, which uniquely reproduce both the expression pattern of receptors on target organs and circulating cells, as well as HuSAP-mediated inhibition of free toxin. In addition, clinical trials could evaluate the ability of NAB815 to prevent HUS development in STEC-infected patients.

NAB815 does not induce SOS response or Shiga toxins production in antibiotic-treated *E. coli* strains

The administration of antibiotics in STEC infected patients remains controversial due to concerns about inducing the bacterial SOS response, which by activating integrated prophages enhances Stx expression and release, thus increasing the risk of developing HUS [13, 74, 75, 160]. As previously mentioned, sub-bactericidal doses of NAB815 protected Vero cells and CD-1 mice from Stx2a-related toxicity [177]. A critical aspect in proposing the treatment of STEC-infected patients with NAB815, given its antibiotic origin, is to exclude off-target effects leading to SOS-mediated stress responses and enhanced Stx production. Antibiotics active against *E. coli* and belonging to different chemical classes

typically exhibit distinct MICs and SOS-inducing concentrations (SICs), with the MIC/SIC ratio reflecting their potential to trigger bacterial stress responses. Accordingly, gentamicin and mitomycin C exhibit weak and strong SOS-inducing activity, respectively, while ciprofloxacin is a model SOS-inducing antibiotic. The MIC/SIC ratios are 1.8, 1.4, and 8 for gentamicin, mitomycin C, and ciprofloxacin, reflecting their relative potential to trigger bacterial stress responses [218-220]. Polymyxin B acting on *E. coli* clinical isolates shows MIC values of 1 μg/mL, with stress responses typically occurring only above this concentration [205, 221]. Similar concentration-dependent patterns appear in Shigella, where toxin release occurs exclusively above MIC levels [222]. Therefore, at 0.01 μg/mL, which is around 100 times lower than the polymyxin B MIC and 200 times below the NAB815 MIC, the tested antibiotics seem unlikely to trigger stress response pathways. However, before testing the compound in clinical settings, it is crucial to verify that the tested sub-inhibitory dose does not enhance Stx release. To specifically address this point, I spent one trimester as a visiting PhD student at the University Hospital of Münster (Germany) where it was investigated whether NAB815 could trigger bacterial SOS response, prophage activation, or increased toxin production using engineered reporter strains and clinical STEC isolates.

Real-time fluorescence monitoring of *STEC* O157:H7 EDL933 Δ*stx2 stx1::yfp* pMBM25 and *O104:H4 stx2::yfp* pKB1 *recAP::cfp* reporter strains demonstrated that NAB815, at concentrations of 0.01, 0.1, and 1 μg/mL, did not affect bacterial growth or induce activation of the SOS response. Similarly, the parent compound polymyxin B produced no detectable effects at the same concentrations. In contrast, 0.1 μg/mL ciprofloxacin inhibited bacterial growth and triggered SOS induction. Time-resolved fluorescence analysis revealed patterns consistent with those reported by other authors using different antibiotics on the same strains [72]. Although the *STEC* O157:H7 EDL933 Δ*stx2 stx1::yfp* pMBM25 strain was identical to that used in a previous study, no increase in CFP signal was detected during time-resolved analysis of *stx1* activation at any concentration of the tested compounds. Fluorescence microscopy further confirmed that NAB815 and polymyxin B, at all tested concentrations, did not alter cell morphology reflecting their mechanism of action. Indeed, polymyxin B and NAB815 are membrane-targeting antibiotics, not DNA-damaging agents, and therefore do not trigger *recAP* activation, which responds specifically to the accumulation of single-stranded DNA [223]. In contrast, ciprofloxacin-treated bacteria displayed a characteristic elongated morphology and were CFP-positive, consistent with SOS response activation. Accordingly, the use of antibiotics

in STEC infections is not universally detrimental, as some can modulate the SOS response and Stx production induced by ciprofloxacin. For example, the transcriptional inhibitor rifaximin and the translational inhibitors azithromycin, tetracycline, and gentamicin suppress SOS induction and Stx1 expression in a concentration-dependent manner, whether added before or after ciprofloxacin, demonstrating their capacity to mitigate the toxin-inducing effects of DNA-damaging agents [72]. Western blot and Vero cell cytotoxicity assays confirm that NAB815 and polymyxin B do not induce Stx production in clinical STEC isolates, consistent with the lack of SOS activation observed in reporter strains. The strong induction of Stx1 observed in the Western blot analysis with the Stx1-producing strain upon ciprofloxacin treatment was accompanied by a corresponding increase in cytotoxicity in Vero cell viability assays. In contrast, although ciprofloxacin treatment led to a statistically significant increase in Stx2 production, the effect on Vero cells was milder compared to Stx1 levels, reflecting differences in the level of toxin expression between the respective strains, and the approximately tenfold higher sensitivity of Vero cells to Stx1a compared to Stx2a [77].

In conclusion, NAB815, used at sub-inhibitory concentrations far below its MIC does not induce SOS responses, prophage activation, or Stx production, preserving bacterial growth and morphology, and thus offers protection against Stx2a-mediated cytotoxicity without triggering toxin release by STEC. These studies support the safety profile of NAB815 observed in mice experiments, highlighting its potential as a therapeutic agent to prevent HUS, and justify testing the drug in animal models closer to humans or in clinical trials.

Conclusions

This thesis investigated the complex interplay between Stx and HUS, as well as potential diagnostic and therapeutic strategies, addressing three interconnected levels: pathophysiology, diagnosis, and treatment. At the pathophysiological level, the research activity contributed to clarify the distinct and combined roles of Stx1a and Stx2a in HUS development.

At the diagnostic level, a novel SERS/PCA based-biosensor was developed and validated. The device achieved high sensitivity and specificity, allowing precise discrimination of Stx1a, Stx2a, and cleaved Stx2a through their molecular fingerprints. This represents a significant advancement toward rapid, sensitive, and label-free detection of circulating Stx, with potential for early clinical diagnosis.

At the therapeutic level**,** the study demonstrated the efficacy of NAB815 in inhibiting Stx2a binding to immune cells and reducing the release of Stx-containing EV. Its negligible impact on bacterial growth and toxin production supports its potential as a safe, therapeutic candidate.

Overall, the three-year PhD project successfully achieved its objectives: (1) elucidating the contributions of Stx1a and Stx2a to HUS pathogenesis; (2) developing a sensitive SERS-based diagnostic tool for Stx detection; and (3) validating NAB815 as a promising therapeutic tool. Together, these findings expand current understanding of STEC infection and offer a foundation for future translational research.

Bibliography

1. Tarr, G.A.M., et al., *Case definitions of hemolytic uremic syndrome following Escherichia coli O157:H7 infection vary in validity.* Int J Med Microbiol, 2018. **308**(8): p. 1121-1127.
2. Karpman, D., et al., *Haemolytic uraemic syndrome.* Journal of Internal Medicine, 2017. **281**(2): p. 123-148.
3. Joseph, A., et al., *Shiga Toxin-Associated Hemolytic Uremic Syndrome: A Narrative Review.* Toxins (Basel), 2020. **12**(2).
4. Williams, D.M., et al., *Acute Kidney Failure: A Pediatric Experience Over 20 Years.* Archives of Pediatrics & Adolescent Medicine, 2002. **156**(9): p. 893-900.
5. Bhandari, J., P. Rout, and Y.R. Sedhai, *Hemolytic Uremic Syndrome*, in *StatPearls*. 2025, StatPearls Publishing
   Copyright © 2025, StatPearls Publishing LLC.: Treasure Island (FL).
6. Gasser, C., et al., *[Hemolytic-uremic syndrome: bilateral necrosis of the renal cortex in acute acquired hemolytic anemia].* Schweiz Med Wochenschr, 1955. **85**(38-39): p. 905-9.
7. Karmali, M.A., et al., *Sporadic cases of haemolytic-uraemic syndrome associated with faecal cytotoxin and cytotoxin-producing Escherichia coli in stools.* Lancet, 1983. **1**(8325): p. 619-20.
8. Riley, L.W., et al., *Hemorrhagic colitis associated with a rare Escherichia coli serotype.* N Engl J Med, 1983. **308**(12): p. 681-5.
9. M., B., *Shiga Toxins: The Ribosome-inactivating Proteins from Pathogenic Bacteria*, in *Ribosome-inactivating Proteins: Ricin and Related Proteins*, L.D. Stirpe F., Editor. 2014, Wiley & Sons.
10. Freedman, S.B., N. van de Kar, and P.I. Tarr, *Shiga Toxin-Producing Escherichia coli and the Hemolytic-Uremic Syndrome.* N Engl J Med, 2023. **389**(15): p. 1402-1414.
11. Paton, J.C. and A.W. Paton, *Pathogenesis and diagnosis of Shiga toxin-producing Escherichia coli infections.* Clin Microbiol Rev, 1998. **11**(3): p. 450-79.
12. Zoja, C., S. Buelli, and M. Morigi, *Shiga toxin-associated hemolytic uremic syndrome: pathophysiology of endothelial dysfunction.* Pediatr Nephrol, 2010. **25**(11): p. 2231-40.
13. Tarr, P.I., C.A. Gordon, and W.L. Chandler, *Shiga-toxin-producing Escherichia coli and haemolytic uraemic syndrome.* Lancet, 2005. **365**(9464): p. 1073-86.
14. Müthing, J., et al., *Shiga toxins, glycosphingolipid diversity, and endothelial cell injury.* Thromb Haemost, 2009. **101**(2): p. 252-64.
15. Richardson, S.E., et al., *The histopathology of the hemolytic uremic syndrome associated with verocytotoxin-producing Escherichia coli infections.* Hum Pathol, 1988. **19**(9): p. 1102-8.
16. Bielaszewska, M. and H. Karch, *Consequences of enterohaemorrhagic Escherichia coli infection for the vascular endothelium.* Thromb Haemost, 2005. **94**(2): p. 312-8.
17. Inward, C.D., et al., *Renal histopathology in fatal cases of diarrhoea-associated haemolytic uraemic syndrome. British Association for Paediatric Nephrology.* Pediatr Nephrol, 1997. **11**(5): p. 556-9.
18. Ray, P.E. and X.H. Liu, *Pathogenesis of Shiga toxin-induced hemolytic uremic syndrome.* Pediatr Nephrol, 2001. **16**(10): p. 823-39.
19. Nataro, J.P. and J.B. Kaper, *Diarrheagenic Escherichia coli.* Clin Microbiol Rev, 1998. **11**(1): p. 142-201.
20. Konowalchuk, J., J.I. Speirs, and S. Stavric, *Vero response to a cytotoxin of Escherichia coli.* Infection and Immunity, 1977. **18**(3): p. 775-779.

21. Ardissino, G., et al., *Bloody Diarrhea and Shiga Toxin-Producing Escherichia coli Hemolytic Uremic Syndrome in Children: Data from the ItalKid-HUS Network*. J Pediatr, 2021. **237**: p. 34-40.e1.
22. Vishram, B., et al., *The emerging importance of Shiga toxin-producing Escherichia coli other than serogroup O157 in England*. J Med Microbiol, 2021. **70**(7).
23. Khalid, M. and S. Andreoli, *Extrarenal manifestations of the hemolytic uremic syndrome associated with Shiga toxin-producing Escherichia coli (STEC HUS)*. Pediatr Nephrol, 2019. **34**(12): p. 2495-2507.
24. Ardissino, G., et al., *Is Shigatoxin 1 protective for the development of Shigatoxin 2-related hemolytic uremic syndrome in children? Data from the ItalKid-HUS Network*. Pediatr Nephrol, 2020. **35**(10): p. 1997-2001.
25. Ostroff, S.M., et al., *Toxin Genotypes and Plasmid Profiles as Determinants of Systemic Sequelae in Escherichia coli O157:H7 Infections*. The Journal of Infectious Diseases, 1989. **160**(6): p. 994-998.
26. Travert, B., et al., *Shiga Toxin-Associated Hemolytic Uremic Syndrome in Adults, France, 2009-2017*. Emerg Infect Dis, 2021. **27**(7): p. 1876-1885.
27. Majowicz, S.E., et al., *Global incidence of human Shiga toxin-producing Escherichia coli infections and deaths: a systematic review and knowledge synthesis*. Foodborne Pathog Dis, 2014. **11**(6): p. 447-55.
28. Alhadlaq, M.A., et al., *Overview of pathogenic Escherichia coli, with a focus on Shiga toxin-producing serotypes, global outbreaks (1982–2024) and food safety criteria*. Gut Pathogens, 2024. **16**(1): p. 57.
29. Pollock, K.G., et al., *Sorbitol-fermenting Escherichia coli O157, Scotland*. Emerg Infect Dis, 2010. **16**(5): p. 881-2.
30. Tilden, J., Jr., et al., *A new route of transmission for Escherichia coli: infection from dry fermented salami*. Am J Public Health, 1996. **86**(8): p. 1142-5.
31. Persad, A.K. and J.T. LeJeune, *Animal Reservoirs of Shiga Toxin-Producing Escherichia coli*. Microbiol Spectr, 2014. **2**(4): p. Ehec-0027-2014.
32. Pruimboom-Brees, I.M., et al., *Cattle lack vascular receptors for Escherichia coli O157:H7 Shiga toxins*. Proc Natl Acad Sci U S A, 2000. **97**(19): p. 10325-9.
33. Hoey, D.E., et al., *Verotoxin 1 binding to intestinal crypt epithelial cells results in localization to lysosomes and abrogation of toxicity*. Cell Microbiol, 2003. **5**(2): p. 85-97.
34. Kintz, E., et al., *Transmission pathways for sporadic Shiga-toxin producing E. coli infections: A systematic review and meta-analysis*. Int J Hyg Environ Health, 2017. **220**(1): p. 57-67.
35. Allerberger, F., et al., *Escherichia coli O157 infections and unpasteurised milk*. Euro Surveill, 2001. **6**(10): p. 147-51.
36. Solomon, E.B., S. Yaron, and K.R. Matthews, *Transmission of Escherichia coli O157:H7 from contaminated manure and irrigation water to lettuce plant tissue and its subsequent internalization*. Appl Environ Microbiol, 2002. **68**(1): p. 397-400.
37. *Importance of culture confirmation of shiga toxin-producing Escherichia coli infection as illustrated by outbreaks of gastroenteritis--New York and North Carolina, 2005*. MMWR Morb Mortal Wkly Rep, 2006. **55**(38): p. 1042-5.
38. Hildebrand, J.M., et al., *An outbreak of Escherichia coli O157 infection linked to paddling pools*. Commun Dis Rep CDR Rev, 1996. **6**(2): p. R33-6.
39. Salvadori, M.I., et al., *Factors that led to the Walkerton tragedy*. Kidney Int Suppl, 2009(112): p. S33-4.
40. Henderson, H., *Direct and indirect zoonotic transmission of Shiga toxin-producing Escherichia coli*. J Am Vet Med Assoc, 2008. **232**(6): p. 848-59.

41. Bosilevac, J.M. and M. Koohmaraie, *Prevalence and characterization of non-O157 shiga toxin-producing Escherichia coli isolates from commercial ground beef in the United States*. Appl Environ Microbiol, 2011. **77**(6): p. 2103-12.
42. Tokuda, K., Y. Yahata, and T. Sunagawa, *Prevention of secondary household transmission during Shiga toxin-producing Escherichia coli outbreaks*. Epidemiol Infect, 2016. **144**(14): p. 2931-2939.
43. *Infections Associated With Group Childcare*. Principles and Practice of Pediatric Infectious Diseases, 2017: p. 25-32.e3.
44. Dabke, G., et al., *Duration of shedding of Verocytotoxin-producing Escherichia coli in children and risk of transmission in childcare facilities in England*. Epidemiol Infect, 2014. **142**(2): p. 327-34.
45. Michino, H., et al., *Massive outbreak of Escherichia coli O157:H7 infection in schoolchildren in Sakai City, Japan, associated with consumption of white radish sprouts*. Am J Epidemiol, 1999. **150**(8): p. 787-96.
46. Buchholz, U., et al., *German outbreak of Escherichia coli O104:H4 associated with sprouts*. N Engl J Med, 2011. **365**(19): p. 1763-70.
47. Rasko, D.A., et al., *Origins of the E. coli strain causing an outbreak of hemolytic-uremic syndrome in Germany*. N Engl J Med, 2011. **365**(8): p. 709-17.
48. Frank, C., et al., *Epidemic profile of Shiga-toxin-producing Escherichia coli O104:H4 outbreak in Germany*. N Engl J Med, 2011. **365**(19): p. 1771-80.
49. Bielaszewska, M., et al., *Characterisation of the Escherichia coli strain associated with an outbreak of haemolytic uraemic syndrome in Germany, 2011: a microbiological study*. Lancet Infect Dis, 2011. **11**(9): p. 671-6.
50. Torres, A.G., et al., *Recent Advances in Shiga Toxin-Producing Escherichia coli Research in Latin America*. Microorganisms, 2018. **6**(4).
51. Rivas, M., et al., *Characterization and epidemiologic subtyping of Shiga toxin-producing Escherichia coli strains isolated from hemolytic uremic syndrome and diarrhea cases in Argentina*. Foodborne Pathog Dis, 2006. **3**(1): p. 88-96.
52. Noris, M. and G. Remuzzi, *Atypical hemolytic-uremic syndrome*. N Engl J Med, 2009. **361**(17): p. 1676-87.
53. Vaziri-Sani, F., et al., *Phenotypic expression of factor H mutations in patients with atypical hemolytic uremic syndrome*. Kidney Int, 2006. **69**(6): p. 981-8.
54. Kavanagh, D., T.H. Goodship, and A. Richards, *Atypical hemolytic uremic syndrome*. Semin Nephrol, 2013. **33**(6): p. 508-30.
55. Raina, R., et al., *Atypical Hemolytic-Uremic Syndrome: An Update on Pathophysiology, Diagnosis, and Treatment*. Ther Apher Dial, 2019. **23**(1): p. 4-21.
56. Shiga, K., *Über den Dysenteriebacillus (Bacillus dysenteriae)*. Zentralbl Bakteriol Orig, 1898. **24**: p. 913-918.
57. Konowalchuk, J., J.I. Speirs, and S. Stavric, *Vero response to a cytotoxin of Escherichia coli*. Infect Immun, 1977. **18**(3): p. 775-9.
58. Strockbine, N.A., et al., *Cloning and sequencing of the genes for Shiga toxin from Shigella dysenteriae type 1*. J Bacteriol, 1988. **170**(3): p. 1116-22.
59. Melton-Celsa, A.R., *Shiga Toxin (Stx) Classification, Structure, and Function*. Microbiol Spectr, 2014. **2**(4): p. Ehec-0024-2013.
60. Gill, A., et al., *Characterization of Atypical Shiga Toxin Gene Sequences and Description of Stx2j, a New Subtype*. J Clin Microbiol, 2022. **60**(3): p. e0222921.
61. Scheutz, F., et al., *Multicenter evaluation of a sequence-based protocol for subtyping Shiga toxins and standardizing Stx nomenclature*. J Clin Microbiol, 2012. **50**(9): p. 2951-63.
62. Brett, K.N., et al., *stx1c Is the most common Shiga toxin 1 subtype among Shiga toxin-producing Escherichia coli isolates from sheep but not among isolates from cattle*. J Clin Microbiol, 2003. **41**(3): p. 926-36.

63. Bürk, C., et al., *Identification and characterization of a new variant of Shiga toxin 1 in Escherichia coli ONT:H19 of bovine origin*. J Clin Microbiol, 2003. **41**(5): p. 2106-12.
64. Wang, X., et al., *A Comprehensive Review on Shiga Toxin Subtypes and Their Niche-Related Distribution Characteristics in Shiga-Toxin-Producing E. coli and Other Bacterial Hosts*. Microorganisms, 2024. **12**(4): p. 687.
65. Kokai-Kun, J.F., A.R. Melton-Celsa, and A.D. O'Brien, *Elastase in intestinal mucus enhances the cytotoxicity of Shiga toxin type 2d*. J Biol Chem, 2000. **275**(5): p. 3713-21.
66. Bielaszewska, M., et al., *Shiga toxin activatable by intestinal mucus in Escherichia coli isolated from humans: predictor for a severe clinical outcome*. Clin Infect Dis, 2006. **43**(9): p. 1160-7.
67. Bunger, J.C., et al., *Reduced Toxicity of Shiga Toxin (Stx) Type 2c in Mice Compared to Stx2d Is Associated with Instability of Stx2c Holotoxin*. Toxins, 2015. **7**(6): p. 2306-2320.
68. Marques, L.R.M., et al., *Escherichia coli strains isolated from pigs with edema disease produce a variant of Shiga-like toxin II*. FEMS Microbiology Letters, 1987. **44**(1): p. 33-38.
69. Rodríguez-Rubio, L., et al., *Bacteriophages of Shiga Toxin-Producing Escherichia coli and Their Contribution to Pathogenicity*. Pathogens, 2021. **10**(4).
70. Krüger, A. and P.M. Lucchesi, *Shiga toxins and stx phages: highly diverse entities*. Microbiology (Reading), 2015. **161**(Pt 3): p. 451-62.
71. Johansen, B.K., et al., *Mosaic structure of Shiga-toxin-2-encoding phages isolated from Escherichia coli O157:H7 indicates frequent gene exchange between lambdoid phage genomes*. Microbiology (Reading), 2001. **147**(Pt 7): p. 1929-1936.
72. Berger, M., et al., *Transcriptional and Translational Inhibitors Block SOS Response and Shiga Toxin Expression in Enterohemorrhagic Escherichia coli*. Scientific Reports, 2019. **9**(1): p. 18777.
73. Wagner, P.L., et al., *Bacteriophage control of Shiga toxin 1 production and release by Escherichia coli*. Mol Microbiol, 2002. **44**(4): p. 957-70.
74. Tarr, P.I. and S.B. Freedman, *Why antibiotics should not be used to treat Shiga toxin-producing Escherichia coli infections*. Current Opinion in Gastroenterology, 2022. **38**(1): p. 30-38.
75. Waldor, M.K. and D.I. Friedman, *Phage regulatory circuits and virulence gene expression*. Curr Opin Microbiol, 2005. **8**(4): p. 459-65.
76. Chan, Y.S. and T.B. Ng, *Shiga toxins: from structure and mechanism to applications*. Appl Microbiol Biotechnol, 2016. **100**(4): p. 1597-1610.
77. Menge, C., *Molecular Biology of Escherichia Coli Shiga Toxins' Effects on Mammalian Cells*. Toxins (Basel), 2020. **12**(5).
78. Ling, H., et al., *Structure of the shiga-like toxin I B-pentamer complexed with an analogue of its receptor Gb3*. Biochemistry, 1998. **37**(7): p. 1777-88.
79. Bast, D.J., et al., *The identification of three biologically relevant globotriaosyl ceramide receptor binding sites on the Verotoxin 1 B subunit*. Molecular Microbiology, 1999. **32**(5): p. 953-960.
80. Garred, O., et al., *Role of processing and intracellular transport for optimal toxicity of Shiga toxin and toxin mutants*. Exp Cell Res, 1995. **218**(1): p. 39-49.
81. Kulczyk, A.W., et al., *Cryo-EM structure of Shiga toxin 2 in complex with the native ribosomal P-stalk reveals residues involved in the binding interaction*. J Biol Chem, 2023. **299**(1): p. 102795.
82. Basu, D., et al., *The A1 Subunit of Shiga Toxin 2 Has Higher Affinity for Ribosomes and Higher Catalytic Activity than the A1 Subunit of Shiga Toxin 1*. Infect Immun, 2016. **84**(1): p. 149-61.
83. Fraser, M.E., et al., *Structure of shiga toxin type 2 (Stx2) from Escherichia coli O157:H7*. J Biol Chem, 2004. **279**(26): p. 27511-7.

84. Gallegos, K.M., et al., *Shiga toxin binding to glycolipids and glycans.* PLoS One, 2012. **7**(2): p. e30368.
85. Celi, A.B., et al., *Role of Globotriaosylceramide in Physiology and Pathology.* Front Mol Biosci, 2022. **9**: p. 813637.
86. Merrill, A.H., Jr., *Sphingolipid and glycosphingolipid metabolic pathways in the era of sphingolipidomics.* Chem Rev, 2011. **111**(10): p. 6387-422.
87. Obrig, T.G., et al., *Endothelial heterogeneity in Shiga toxin receptors and responses.* Journal of Biological Chemistry, 1993. **268**(21): p. 15484-15488.
88. Schüller, S., et al., *Shiga toxin binding in normal and inflamed human intestinal mucosa*. Microbes Infect, 2007. **9**(1): p. 35-9.
89. Detzner, J., G. Pohlentz, and J. Müthing, *Valid Presumption of Shiga Toxin-Mediated Damage of Developing Erythrocytes in EHEC-Associated Hemolytic Uremic Syndrome.* Toxins, 2020. **12**(6): p. 373.
90. Brigotti, M., *The Interactions of Human Neutrophils with Shiga Toxins and Related Plant Toxins: Danger or Safety?* Toxins, 2012. **4**(3): p. 157-190.
91. van Setten, P.A., et al., *Effects of verocytotoxin-1 on nonadherent human monocytes: binding characteristics, protein synthesis, and induction of cytokine release.* Blood, 1996. **88**(1): p. 174-83.
92. Karpman, D., et al., *Platelet activation by Shiga toxin and circulatory factors as a pathogenetic mechanism in the hemolytic uremic syndrome.* Blood, 2001. **97**(10): p. 3100-8.
93. Yan, N. and Z.J. Chen, *Intrinsic antiviral immunity.* Nat Immunol, 2012. **13**(3): p. 214-22.
94. George, T., et al., *MHC class II proteins contain a potential binding site for the verotoxin receptor glycolipid CD77.* Cell Mol Biol (Noisy-le-grand), 2001. **47**(7): p. 1179-85.
95. Morace, I., et al., *Renal globotriaosylceramide facilitates tubular albumin absorption and its inhibition protects against acute kidney injury.* Kidney Int, 2019. **96**(2): p. 327-341.
96. Okuda, T., et al., *Targeted Disruption of Gb3/CD77 Synthase Gene Resulted in the Complete Deletion of Globo-series Glycosphingolipids and Loss of Sensitivity to Verotoxins**. Journal of Biological Chemistry, 2006. **281**(15): p. 10230-10235.
97. Brigotti, M., et al., *The structure of the Shiga toxin 2a A-subunit dictates the interactions of the toxin with blood components.* Cell Microbiol, 2019. **21**(5): p. e13000.
98. Itoh, K., et al., *Different binding property of verotoxin-1 and verotoxin-2 against their glycolipid receptor, globotriaosylceramide.* Tohoku J Exp Med, 2001. **195**(4): p. 237-43.
99. Tesh, V.L., et al., *Comparison of the relative toxicities of Shiga-like toxins type I and type II for mice.* Infect Immun, 1993. **61**(8): p. 3392-402.
100. Siegler, R.L., et al., *Response to Shiga Toxin-1, with and without Lipopolysaccharide, in a Primate Model of Hemolytic Uremic Syndrome.* American Journal of Nephrology, 2001. **21**(5): p. 420-425.
101. Ergonul, Z., et al., *Shigatoxin-1 binding and receptor expression in human kidneys do not change with age.* Pediatr Nephrol, 2003. **18**(3): p. 246-53.
102. Varrone, E., et al., *Detection of Cleaved Stx2a in the Blood of STEC-Infected Patients.* Toxins, 2023. **15**(12): p. 690.
103. Jackson, M.P., *Structure-function analyses of Shiga toxin and the Shiga-like toxins.* Microb Pathog, 1990. **8**(4): p. 235-42.
104. Sandvig, K., et al., *Endocytosis and retrograde transport of Shiga toxin*. Toxicon, 2010. **56**(7): p. 1181-5.
105. Torgersen, M.L., S.U. Lauvrak, and K. Sandvig, *The A-subunit of surface-bound Shiga toxin stimulates clathrin-dependent uptake of the toxin.* Febs j, 2005. **272**(16): p. 4103-13.
106. Garred, O., B. van Deurs, and K. Sandvig, *Furin-induced cleavage and activation of Shiga toxin.* J Biol Chem, 1995. **270**(18): p. 10817-21.

107. Melton-Celsa, A.R., S.C. Darnell, and A.D. O'Brien, *Activation of Shiga-like toxins by mouse and human intestinal mucus correlates with virulence of enterohemorrhagic Escherichia coli O91:H21 isolates in orally infected, streptomycin-treated mice.* Infection and Immunity, 1996. **64**(5): p. 1569-1576.
108. Melton-Celsa, A.R., S.C. Darnell, and A.D. O'Brien, *Activation of Shiga-like toxins by mouse and human intestinal mucus correlates with virulence of enterohemorrhagic Escherichia coli O91:H21 isolates in orally infected, streptomycin-treated mice.* Infect Immun, 1996. **64**(5): p. 1569-76.
109. Endo, Y., et al., *Site of action of a Vero toxin (VT2) from Escherichia coli O157:H7 and of Shiga toxin on eukaryotic ribosomes. RNA N-glycosidase activity of the toxins.* Eur J Biochem, 1988. **171**(1-2): p. 45-50.
110. Matussek, A., et al., *Molecular and functional analysis of Shiga toxin–induced response patterns in human vascular endothelial cells.* Blood, 2003. **102**(4): p. 1323-1332.
111. Tesh, V.L., *Activation of cell stress response pathways by Shiga toxins.* Cell Microbiol, 2012. **14**(1): p. 1-9.
112. Jandhyala, D.M., C.M. Thorpe, and B. Magun, *Ricin and Shiga toxins: effects on host cell signal transduction.* Curr Top Microbiol Immunol, 2012. **357**: p. 41-65.
113. Brigotti, M., et al., *Damage to nuclear DNA induced by Shiga toxin 1 and ricin in human endothelial cells.* Faseb j, 2002. **16**(3): p. 365-72.
114. Brigotti, M., et al., *Shiga toxin 1: damage to DNA in vitro.* Toxicon, 2001. **39**(2-3): p. 341-8.
115. Fujii, J., et al., *Shiga Toxin 2 Causes Apoptosis in Human Brain Microvascular Endothelial Cells via C/EBP Homologous Protein.* Infection and Immunity, 2008. **76**(8): p. 3679-3689.
116. Arfilli, V., et al., *Shiga toxin 1 and ricin A chain bind to human polymorphonuclear leucocytes through a common receptor.* Biochem J, 2010. **432**(1): p. 173-80.
117. Macher, B.A. and J.C. Klock, *Isolation and chemical characterization of neutral glycosphingolipids of human neutrophils.* J Biol Chem, 1980. **255**(5): p. 2092-6.
118. Fernandez, G.C., et al., *The functional state of neutrophils correlates with the severity of renal dysfunction in children with hemolytic uremic syndrome.* Pediatr Res, 2007. **61**(1): p. 123-8.
119. te Loo, D.M., et al., *Binding and transfer of verocytotoxin by polymorphonuclear leukocytes in hemolytic uremic syndrome.* Blood, 2000. **95**(11): p. 3396-402.
120. Brigotti, M., et al., *Identification of TLR4 as the receptor that recognizes Shiga toxins in human neutrophils.* J Immunol, 2013. **191**(9): p. 4748-58.
121. Kawai, T., et al., *Decoding Toll-like receptors: Recent insights and perspectives in innate immunity.* Immunity, 2024. **57**(4): p. 649-673.
122. Brigotti, M., et al., *Soluble Toll-Like Receptor 4 Impairs the Interaction of Shiga Toxin 2a with Human Serum Amyloid P Component.* Toxins (Basel), 2018. **10**(9).
123. Zunt, S.L., et al., *Soluble forms of Toll-like receptor 4 are present in human saliva and modulate tumour necrosis factor-α secretion by macrophage-like cells.* Clinical and Experimental Immunology, 2009. **156**(2): p. 285-293.
124. Torgersen, M.L., et al., *Toll-like receptor 4 facilitates binding of Shiga toxin to colon carcinoma and primary umbilical vein endothelial cells.* FEMS Immunol Med Microbiol, 2011. **61**(1): p. 63-75.
125. Kimura, T., et al., *Serum Amyloid P Component Is the Shiga Toxin 2-neutralizing Factor in Human Blood* *. Journal of Biological Chemistry, 2001. **276**(45): p. 41576-41579.
126. Marcato, P., et al., *Serum Amyloid P Component Binding to Shiga Toxin 2 Requires Both A Subunit and B Pentamer.* Infection and Immunity, 2003. **71**(10): p. 6075-6078.
127. Griener, T.P., et al., *Differential binding of Shiga toxin 2 to human and murine neutrophils.* Journal of Medical Microbiology, 2007. **56**(11): p. 1423-1430.

128. Armstrong, G.D., et al., *Human serum amyloid P component protects against Escherichia coli O157:H7 Shiga toxin 2 in vivo: therapeutic implications for hemolytic-uremic syndrome.* J Infect Dis, 2006. **193**(8): p. 1120-4.
129. Brigotti, M., et al., *Clinical relevance of shiga toxin concentrations in the blood of patients with hemolytic uremic syndrome.* Pediatr Infect Dis J, 2011. **30**(6): p. 486-90.
130. He, X., et al., *Serum Shiga toxin 2 values in patients during acute phase of diarrhoea-associated haemolytic uraemic syndrome.* Acta Paediatrica, 2015. **104**(12): p. e564-e568.
131. Brigotti, M., et al., *Particulate Shiga Toxin 2 in Blood is Associated to the Development of Hemolytic Uremic Syndrome in Children*. Thromb Haemost, 2020. **120**(1): p. 107-120.
132. Varrone, E., D. Carnicelli, and M. Brigotti, *Extracellular Vesicles and Renal Endothelial Cells: A Fatal Attraction in Hemolytic Uremic Syndrome.* The American Journal of Pathology, 2021. **191**(5): p. 795-804.
133. Ståhl, A.L., et al., *Shiga toxin and lipopolysaccharide induce platelet-leukocyte aggregates and tissue factor release, a thrombotic mechanism in hemolytic uremic syndrome.* PLoS One, 2009. **4**(9): p. e6990.
134. McEver, R., *Chapter 12. P-Selectin/PSGL-1 and other interactions between platelets, leukocytes, and endothelium*. 2007. p. 231-249.
135. Grange, C. and B. Bussolati, *Extracellular vesicles in kidney disease.* Nat Rev Nephrol, 2022. **18**(8): p. 499-513.
136. Raposo, G. and W. Stoorvogel, *Extracellular vesicles: exosomes, microvesicles, and friends.* J Cell Biol, 2013. **200**(4): p. 373-83.
137. Karpman, D., A.L. Ståhl, and I. Arvidsson, *Extracellular vesicles in renal disease.* Nat Rev Nephrol, 2017. **13**(9): p. 545-562.
138. Welsh, J.A., et al., *Minimal information for studies of extracellular vesicles (MISEV2023): From basic to advanced approaches.* J Extracell Vesicles, 2024. **13**(2): p. e12404.
139. Ståhl, A.L., et al., *A novel mechanism of bacterial toxin transfer within host blood cell-derived microvesicles.* PLoS Pathog, 2015. **11**(2): p. e1004619.
140. Louise, C.B. and T.G. Obrig, *Shiga toxin-associated hemolytic-uremic syndrome: combined cytotoxic effects of Shiga toxin, interleukin-1 beta, and tumor necrosis factor alpha on human vascular endothelial cells in vitro.* Infect Immun, 1991. **59**(11): p. 4173-9.
141. Eisenhauer, P.B., et al., *Tumor necrosis factor alpha increases human cerebral endothelial cell Gb3 and sensitivity to Shiga toxin.* Infect Immun, 2001. **69**(3): p. 1889-94.
142. van de Kar, N.C., et al., *Tumor necrosis factor and interleukin-1 induce expression of the verocytotoxin receptor globotriaosylceramide on human endothelial cells: implications for the pathogenesis of the hemolytic uremic syndrome.* Blood, 1992. **80**(11): p. 2755-64.
143. Behrens, F., et al., *Extracellular vesicles as regulators of kidney function and disease.* Intensive Care Med Exp, 2020. **8**(Suppl 1): p. 22.
144. López, E.L., et al., *An epidemiologic surveillance of Shiga-like toxin-producing Escherichia coli infection in Argentinean children: risk factors and serum Shiga-like toxin 2 values.* Pediatr Infect Dis J, 2012. **31**(1): p. 20-4.
145. Murata, K., et al., *Verotoxin-1 stimulation of macrophage-like THP-1 cells up-regulates tissue factor expression through activation of c-Yes tyrosine kinase: Possible signal transduction in tissue factor up-regulation*. Biochim Biophys Acta, 2006. **1762**(9): p. 835-43.
146. Butenas, S., T. Orfeo, and K.G. Mann, *Tissue Factor in Coagulation*. Arteriosclerosis, Thrombosis, and Vascular Biology, 2009. **29**(12): p. 1989-1996.

147. Monnens, L., et al., *The complement system in hemolytic-uremic syndrome in childhood*. Clin Nephrol, 1980. **13**(4): p. 168-71.
148. Kim, Y., K. Miller, and A.F. Michael, *Breakdown products of C3 and factor B in hemolytic-uremic syndrome.* J Lab Clin Med, 1977. **89**(4): p. 845-50.
149. Robson, W.L., et al., *Hypocomplementemia and leukocytosis in diarrhea-associated hemolytic uremic syndrome.* Nephron, 1992. **62**(3): p. 296-9.
150. Jalal, D., et al., *Endothelial Microparticles and Systemic Complement Activation in Patients With Chronic Kidney Disease.* J Am Heart Assoc, 2018. **7**(14).
151. Walsh, P.R. and S. Johnson, *Eculizumab in the treatment of Shiga toxin haemolytic uraemic syndrome.* Pediatr Nephrol, 2019. **34**(9): p. 1485-1492.
152. Ståhl, A.L., L. Sartz, and D. Karpman, *Complement activation on platelet-leukocyte complexes and microparticles in enterohemorrhagic Escherichia coli-induced hemolytic uremic syndrome.* Blood, 2011. **117**(20): p. 5503-13.
153. Orth, D., et al., *Shiga toxin activates complement and binds factor H: evidence for an active role of complement in hemolytic uremic syndrome.* J Immunol, 2009. **182**(10): p. 6394-400.
154. Morigi, M., et al., *Alternative pathway activation of complement by Shiga toxin promotes exuberant C3a formation that triggers microvascular thrombosis.* J Immunol, 2011. **187**(1): p. 172-80.
155. Ehrlenbach, S., et al., *Shiga toxin 2 reduces complement inhibitor CD59 expression on human renal tubular epithelial and glomerular endothelial cells.* Infect Immun, 2013. **81**(8): p. 2678-85.
156. Friedrich, A.W., et al., *Escherichia coli harboring Shiga toxin 2 gene variants: frequency and association with clinical symptoms.* J Infect Dis, 2002. **185**(1): p. 74-84.
157. Verstraete, K., et al., *Genetic characteristics of Shiga toxin-producing E. coli O157, O26, O103, O111 and O145 isolates from humans, food, and cattle in Belgium.* Epidemiol Infect, 2013. **141**(12): p. 2503-15.
158. Petro, C.D., et al., *Shiga Toxin Type 1a (Stx1a) Reduces the Toxicity of the More Potent Stx2a In Vivo and In Vitro.* Infect Immun, 2019. **87**(4).
159. Russo, L.M., A.R. Melton-Celsa, and A.D. O'Brien, *Shiga Toxin (Stx) Type 1a Reduces the Oral Toxicity of Stx Type 2a*. J Infect Dis, 2016. **213**(8): p. 1271-9.
160. Liu, Y., et al., *Diagnosis and Treatment for Shiga Toxin-Producing Escherichia coli Associated Hemolytic Uremic Syndrome.* Toxins (Basel), 2022. **15**(1).
161. Qin, X., et al., *Real-Time PCR Assay for Detection and Differentiation of Shiga Toxin-Producing Escherichia coli from Clinical Samples.* J Clin Microbiol, 2015. **53**(7): p. 2148-53.
162. Shane, A.L., et al., *2017 Infectious Diseases Society of America Clinical Practice Guidelines for the Diagnosis and Management of Infectious Diarrhea*. Clin Infect Dis, 2017. **65**(12): p. e45-e80.
163. McKee, R.S., et al., *Predicting Hemolytic Uremic Syndrome and Renal Replacement Therapy in Shiga Toxin-producing Escherichia coli-infected Children*. Clin Infect Dis, 2020. **70**(8): p. 1643-1651.
164. Cornick, N.A., et al., *Escherichia coli O157:H7 infections: discordance between filterable fecal shiga toxin and disease outcome.* J Infect Dis, 2002. **186**(1): p. 57-63.
165. Gould, L.H., et al., *Recommendations for diagnosis of shiga toxin--producing Escherichia coli infections by clinical laboratories.* MMWR Recomm Rep, 2009. **58**(Rr-12): p. 1-14.
166. Gould, L.H., et al., *Increased recognition of non-O157 Shiga toxin-producing Escherichia coli infections in the United States during 2000-2010: epidemiologic features and comparison with E. coli O157 infections.* Foodborne Pathog Dis, 2013. **10**(5): p. 453-60.

167. Wijnsma, K.L., et al., *Glyco-iELISA: a highly sensitive and unambiguous serological method to diagnose STEC-HUS caused by serotype O157*. Pediatr Nephrol, 2019. **34**(4): p. 631-639.
168. McLean, K., et al., *Rapid and robust analytical protocol for E. coli STEC bacteria subspecies differentiation using whole cell MALDI mass spectrometry*. Talanta, 2018. **182**: p. 164-170.
169. He, X., et al., *Sensitive detection of Shiga Toxin 2 and some of its variants in environmental samples by a novel immuno-PCR assay*. Appl Environ Microbiol, 2011. **77**(11): p. 3558-64.
170. Rippa, M., et al., *Diagnostic oriented discrimination of different Shiga toxins via PCA-assisted SERS-based plasmonic metasurface*. Nanophotonics, 2025.
171. Hamza, M.E., M.A. Othman, and M.A. Swillam, *Plasmonic Biosensors: Review*. Biology, 2022. **11**(5): p. 621.
172. Katrin, K., et al., *Surface-enhanced Raman scattering and biophysics*. Journal of Physics: Condensed Matter, 2002. **14**(18): p. R597.
173. Fergusson, J., et al., *Plasmonic and Photothermal Properties of Silica-Capped Gold Nanoparticle Aggregates*. The Journal of Physical Chemistry C, 2023. **127**(50): p. 24475-24486.
174. Kambhampati, P., et al., *On the chemical mechanism of surface enhanced Raman scattering: Experiment and theory*. Journal of Chemical Physics, 1998. **108**(12): p. 5013-5026.
175. Kneipp, K., *Surface-Enhanced Raman Scattering*. Physics Today, 2007. **60**: p. 40.
176. Rippa, M., et al., *Plasmonic Metasurfaces for Specific SERS Detection of Shiga Toxins*. ACS Applied Materials & Interfaces, 2022. **14**(4): p. 4969-4979.
177. Varrone, E., et al., *An antibiotic derivative as a new potential tool in the prevention of hemolytic uremic syndrome*. iScience, 2025. **28**(8): p. 113076.
178. Hickey, C.A., et al., *Early volume expansion during diarrhea and relative nephroprotection during subsequent hemolytic uremic syndrome*. Arch Pediatr Adolesc Med, 2011. **165**(10): p. 884-9.
179. Sutherland, S.M., et al., *Fluid overload and mortality in children receiving continuous renal replacement therapy: the prospective pediatric continuous renal replacement therapy registry*. Am J Kidney Dis, 2010. **55**(2): p. 316-25.
180. Karpman, D., *Management of Shiga toxin-associated Escherichia coli-induced haemolytic uraemic syndrome: randomized clinical trials are needed*. Nephrol Dial Transplant, 2012. **27**(10): p. 3669-74.
181. Coccia, P.A., et al., *Acute peritoneal dialysis, complications and outcomes in 389 children with STEC-HUS: a multicenter experience*. Pediatr Nephrol, 2021. **36**(6): p. 1597-1606.
182. Loos, S., et al., *An outbreak of Shiga toxin-producing Escherichia coli O104:H4 hemolytic uremic syndrome in Germany: presentation and short-term outcome in children*. Clin Infect Dis, 2012. **55**(6): p. 753-9.
183. de Galasso, L., S. Picca, and I. Guzzo, *Dialysis modalities for the management of pediatric acute kidney injury*. Pediatr Nephrol, 2020. **35**(5): p. 753-765.
184. Mahat, U., R.B. Matar, and S.J. Rotz, *Use of complement monoclonal antibody eculizumab in Shiga toxin producing Escherichia coli associated hemolytic uremic syndrome: A review of current evidence*. Pediatr Blood Cancer, 2019. **66**(11): p. e27913.
185. Keenswijk, W., et al., *Is Plasma Exchange Efficacious in Shiga Toxin-Associated Hemolytic Uremic Syndrome? A Narrative Review of Current Evidence*. Ther Apher Dial, 2019. **23**(2): p. 118-125.
186. Kielstein, J.T., et al., *Best supportive care and therapeutic plasma exchange with or without eculizumab in Shiga-toxin-producing E. coli O104:H4 induced haemolytic-*

uraemic syndrome: an analysis of the German STEC-HUS registry. Nephrol Dial Transplant, 2012. **27**(10): p. 3807-15.
187. Dowling, T.C., et al., *Phase 1 safety and pharmacokinetic study of chimeric murine-human monoclonal antibody c alpha Stx2 administered intravenously to healthy adult volunteers.* Antimicrob Agents Chemother, 2005. **49**(5): p. 1808-12.
188. Moxley, R.A., et al., *Efficacy of Urtoxazumab (TMA-15 Humanized Monoclonal Antibody Specific for Shiga Toxin 2) Against Post-Diarrheal Neurological Sequelae Caused by Escherichia coli O157:H7 Infection in the Neonatal Gnotobiotic Piglet Model.* Toxins (Basel), 2017. **9**(2).
189. Lee, L., A. Abe, and J.A. Shayman, *Improved inhibitors of glucosylceramide synthase.* J Biol Chem, 1999. **274**(21): p. 14662-9.
190. Sánchez, D.S., et al., *Eliglustat prevents Shiga toxin 2 cytotoxic effects in human renal tubular epithelial cells.* Pediatric Research, 2022. **91**(5): p. 1121-1129.
191. Amaral, M.M., et al., *Action of shiga toxin type-2 and subtilase cytotoxin on human microvascular endothelial cells.* PLoS One, 2013. **8**(7): p. e70431.
192. Secher, T., et al., *Retrograde Trafficking Inhibitor of Shiga Toxins Reduces Morbidity and Mortality of Mice Infected with Enterohemorrhagic Escherichia coli.* Antimicrob Agents Chemother, 2015. **59**(8): p. 5010-3.
193. Gandhi, T., et al., *Development of an Arginine Anchored Nanoglobule with Retrograde Trafficking Inhibitor (Retro-2) for the Treatment of an Enterohemorrhagic Escherichia coli Outbreak.* Mol Pharm, 2019. **16**(10): p. 4405-4415.
194. Geerdes-Fenge, H.F., et al., *Ciprofloxacin reduces the risk of hemolytic uremic syndrome in patients with Escherichia coli O104:H4-associated diarrhea.* Infection, 2013. **41**(3): p. 669-73.
195. Tajiri, H., et al., *A role for fosfomycin treatment in children for prevention of haemolytic–uraemic syndrome accompanying Shiga toxin-producing Escherichia coli infection.* International Journal of Antimicrobial Agents, 2015. **46**(5): p. 586-589.
196. Vaara, M., *Polymyxins and their novel derivatives.* Curr Opin Microbiol, 2010. **13**(5): p. 574-81.
197. Guo, Y.B., et al., *Polymyxin B antagonizing biological activity of lipopolysaccharide.* Chin J Traumatol, 2007. **10**(3): p. 180-3.
198. Carnicelli, D., et al., *The Antibiotic Polymyxin B Impairs the Interactions between Shiga Toxins and Human Neutrophils.* J Immunol, 2016. **196**(3): p. 1177-85.
199. Vaara, M., *Novel derivatives of polymyxins.* Journal of Antimicrobial Chemotherapy, 2013. **68**(6): p. 1213-1219.
200. Vaara, M., *New polymyxin derivatives that display improved efficacy in animal infection models as compared to polymyxin B and colistin.* Med Res Rev, 2018. **38**(5): p. 1661-1673.
201. Vaara, M., T. Vaara, and J.M. Tyrrell, *Structure-activity studies on polymyxin derivatives carrying three positive charges only reveal a new class of compounds with strong antibacterial activity.* Peptides, 2017. **91**: p. 8-12.
202. Vaara M, V., T., *Polymyxin derivative and uses thereof.* . 2016: USA.
203. Vaara, M., T. Vaara, and C. Vingsbo Lundberg, *Polymyxin derivatives NAB739 and NAB815 are more effective than polymyxin B in murine Escherichia coli pyelonephritis.* J Antimicrob Chemother, 2018. **73**(2): p. 452-455.
204. Vaara, M., et al., *Excretion of the Polymyxin Derivative NAB739 in Murine Urine.* Antibiotics (Basel), 2020. **9**(4).
205. Chen, S., et al., *Polymyxin B and fusidic acid, a novel potent synergistic combination against Klebsiella pneumoniae and Escherichia coli isolates with polymyxin B resistance.* Frontiers in Microbiology, 2023. **Volume 14 - 2023**.
206. Slingerland, C.J. and N.I. Martin, *Recent Advances in the Development of Polymyxin Antibiotics: 2010–2023.* ACS Infectious Diseases, 2024. **10**(4): p. 1056-1079.

207. Vaara, M., T. Vaara, and J.M. Tyrrell, *Structure–activity studies on polymyxin derivatives carrying three positive charges only reveal a new class of compounds with strong antibacterial activity.* Peptides, 2017. **91**: p. 8-12.
208. Ryd, M., et al., *Purification of Shiga toxin by alpha-D-galactose-(1----4)-beta-D-galactose-(1----4)-beta-D-glucose-(1- ---) receptor ligand-based chromatography.* FEBS Lett, 1989. **258**(2): p. 320-2.
209. Matussek, A., et al., *Molecular and functional analysis of Shiga toxin-induced response patterns in human vascular endothelial cells.* Blood, 2003. **102**(4): p. 1323-32.
210. Chaiwut, R. and W. Kasinrerk, *Very low concentration of lipopolysaccharide can induce the production of various cytokines and chemokines in human primary monocytes.* BMC Res Notes, 2022. **15**(1): p. 42.
211. Salomon, A., et al., *Size and Shape Resonances in Second Harmonic Generation from Silver Nanocavities*. The Journal of Physical Chemistry C, 2013. **117**(43): p. 22377-22382.
212. Rutjes, N.W.P., et al., *Differential tissue targeting and pathogenesis of verotoxins 1 and 2 in the mouse animal model.* Kidney International, 2002. **62**(3): p. 832-845.
213. Jeong, Y.J., et al., *Experimental In Vivo Models of Bacterial Shiga Toxin-Associated Hemolytic Uremic Syndrome.* J Microbiol Biotechnol, 2018. **28**(9): p. 1413-1425.
214. Watanabe-Takahashi, M., et al., *Exosome-associated Shiga toxin 2 is released from cells and causes severe toxicity in mice.* Scientific Reports, 2018. **8**(1): p. 10776.
215. Palermo, M., et al., *Pretreatment of mice with lipopolysaccharide (LPS) or IL-1β exerts dose-dependent opposite effects on Shiga toxin-2 lethality.* Clinical and Experimental Immunology, 2002. **119**(1): p. 77-83.
216. Kawai-Harada, Y., et al., *Evaluation of EV Storage Buffer for Efficient Preservation of Engineered Extracellular Vesicles.* International Journal of Molecular Sciences, 2023. **24**(16): p. 12841.
217. Wolfs, T.G., et al., *In vivo expression of Toll-like receptor 2 and 4 by renal epithelial cells: IFN-gamma and TNF-alpha mediated up-regulation during inflammation.* J Immunol, 2002. **168**(3): p. 1286-93.
218. Chittò, M., et al., *Sub-Inhibitory concentrations of SOS-Response inducing antibiotics stimulate integrase expression and excision of pathogenicity islands in uropathogenic Escherichia coli strain 536.* International Journal of Medical Microbiology, 2020. **310**(1): p. 151361.
219. Crane, J.K., C.L. Alvarado, and M.D. Sutton, *Role of the SOS Response in the Generation of Antibiotic Resistance In Vivo.* Antimicrobial Agents and Chemotherapy, 2021. **65**(7): p. 10.1128/aac.00013-21.
220. Piddock, L.J., R.N. Walters, and J.M. Diver, *Correlation of quinolone MIC and inhibition of DNA, RNA, and protein synthesis and induction of the SOS response in Escherichia coli.* Antimicrobial Agents and Chemotherapy, 1990. **34**(12): p. 2331-2336.
221. Demjanenko, P., S. Zheng, and J.K. Crane, *SOS-Inducing Drugs Trigger Nucleic Acid Release and Biofilm Formation in Gram-Negative Bacteria*. Biomolecules, 2024. **14**(3): p. 321.
222. Griffin, D.E. and P. Gemski, *Release of Shiga Toxin from Shigella dysenteriae 1 by Polymyxin B.* Infection and Immunity, 1983. **40**(1): p. 425-428.
223. Padhy, I., S.K. Dwibedy, and S.S. Mohapatra, *A molecular overview of the polymyxin-LPS interaction in the context of its mode of action and resistance development.* Microbiological Research, 2024. **283**: p. 127679.

Abbreviations

Ab – Antibodies

aHUS – Atypical hemolytic uremic syndrome

ANOVA – Analysis of variance

ATI – Acute tubular injury

BSA – Bovine serum albumin

CFB – Complement factor B

CFH – Complement factor H

CFI – Complement factor I

cfp – Cyan fluorescent protein

CNR– Consiglio Nazionale delle Ricerche

CPD solution – Citrate-phosphate-dextrose

DMEM – Dulbecco's Modified Eagle Medium

E. coli – *Escherichia coli*

EBL – Electron beam lithography

EHEC – Enterohemorrhagic *E. coli*

ELISA – Enzyme-linked immunosorbent assays

EMEM – Eagle's Minimum Essential Medium

EV – Extracellular vesicles

Gb3Cer – Globotriaosylceramide

GPRP – Gly-Pro-Arg-Pro

HuSAP – Human serum amyloid P component

LoD – Limit of detection

LPS – Lipopolysaccharide

LSPR – Localized Surface Plasmon Resonance

MAC – Membrane attack complex

MCP/CD46 – Membrane cofactor protein

mAb – Monoclonal antibodies

MIC – Minimum inhibitory concentration

NTA – Nanoparticle tracking analysis

OD – Optical density

PAMPs – Pathogen-associated molecular patterns

PAS – Periodic acid–Schiff

PCA – Principal component analysis

pAb – Polyclonal antibodies

PBS – Phosphate buffered saline

PRRs – Pattern recognition receptors

PVDF – Polyvinylidene fluoride

RIPs – Ribosome-Inactivating Proteins

S. dysenteriae – *Shigella dysenteriae*

SERS – Surface-Enhanced Raman Spectroscopy

SEM – Scanning electron microscopy

SIC – SOS response-inducing concentration

sTLR – Soluble Toll-like receptor

Stx – Shiga toxins

Stx1 – Shiga toxin 1

Stx2 – Shiga toxin 2

TBS-T – Tris-buffered saline-Tween-20

TF – Tissue factor

TLR – Toll-like receptor

WES – Quantitative capillary Western blot

yfp – Yellow fluorescent protein